

Spring 4-16-2017

FABRICATION AND STUDY OF THE STRUCTURE AND MAGNETISM OF RARE- EARTH FREE NANOCCLUSERS

Bhaskar Das

University of Nebraska-Lincoln, bhaskar.das@huskers.unl.edu

Follow this and additional works at: <http://digitalcommons.unl.edu/physicsdiss>

 Part of the [Condensed Matter Physics Commons](#), [Energy Systems Commons](#), [Metallurgy Commons](#), [Nanoscience and Nanotechnology Commons](#), [Semiconductor and Optical Materials Commons](#), and the [Structural Materials Commons](#)

Das, Bhaskar, "FABRICATION AND STUDY OF THE STRUCTURE AND MAGNETISM OF RARE-EARTH FREE NANOCCLUSERS" (2017). *Theses, Dissertations, and Student Research: Department of Physics and Astronomy*. 35.
<http://digitalcommons.unl.edu/physicsdiss/35>

This Article is brought to you for free and open access by the Physics and Astronomy, Department of at DigitalCommons@University of Nebraska - Lincoln. It has been accepted for inclusion in Theses, Dissertations, and Student Research: Department of Physics and Astronomy by an authorized administrator of DigitalCommons@University of Nebraska - Lincoln.

FABRICATION AND STUDY OF THE STRUCTURE AND MAGNETISM OF
RARE-EARTH FREE NANOCCLUSERS

by

Bhaskar Das

A DISSERTATION

Presented to the Faculty of
The Graduate College at the University of Nebraska
In Partial Fulfillment of Requirements
For the Degree of Doctor of Philosophy

Major: Physics and Astronomy

Under the Supervision of Professor David J. Sellmyer

Lincoln, Nebraska

April, 2017

FABRICATION AND STUDY OF THE STRUCTURE AND MAGNETISM OF
RARE-EARTH FREE NANOCLUSTERS

Bhaskar Das, Ph.D.

University of Nebraska, 2017

Advisor: David J. Sellmyer

Extensive search for new magnetic materials free of critical rare-earth elements or expensive platinum suitable for technology or energy-applications is one of the main factors driving today's research in magnetism. Development of these new materials is often hindered by conventional bulk-synthesis techniques which result in phase mixtures or poor magnetic properties. This dissertation focusses on this problem by investigating an alternate approach to fabricate nanoclusters of magnetic materials using an inert-gas-condensation cluster-deposition method, and analyzing their potential for magnetic applications. Nanoclusters of hard-magnetic Zr_2Co_{11} were studied which have relatively high magnetocrystalline anisotropy as required for permanent-magnet applications. The Zr_2Co_{11} nanoclusters exhibit high coercivity at room temperature, high magnetization and a high-energy product of 16.6 MGOe. When combined with a soft Fe-Co phase, the energy product rises to 19.5 MGOe. *In-situ* magnetic alignment of these nanoclusters is also demonstrated, which enhances the remanent magnetization and energy product. Mn_5Si_3 and Fe_5Si_3 nanoclusters also were studied and high surface spin polarization was demonstrated for these materials resulting in novel magnetism such as, high magnetization and Curie temperature at the nanoscale compared to bulk. These materials show lattice-matching with semiconductors and high spin-polarization, which suggest further studies of these nanoclusters in the context of spintronics as potential spin-injectors.

DEDICATION

To my parents Alope Das and Anasuya Das, whose hard work has enabled me to become what I am. They always inspire me to go forward in life in any circumstances and never lost hope in me.

To my wife, Moumita, who encourages me to fulfil my dreams by sacrificing a lot of her own. I am very thankful to her to remain patient and drive me to think positively through difficult times.

ACKNOWLEDGEMENTS

The role and contribution of my advisor Prof. David J. Sellmyer in my research and my life cannot be explained by simple thanks. He is the reason for what I am today as a person. Besides his scientific expertise, his professional characteristics taught me values of life which I will treasure forever. His guidance and tutelage made me think about research in a way I never thought possible, and that is what made me the scientist I am today. The freedom I got in his research group was the key to rediscover myself through continuous self-analysis and discussing my ideas with him. I sincerely thank him for being my research father and never losing faith in me.

I am grateful to my committee members Prof. Ralph Skomski, Prof. Sy-Hwang Liou and Prof. Jeffrey E. Shield for their valuable advice during my research and their thoughtful criticism of my work without which I could not have come this far. Criticism I obtained from Prof. Skomski helped me to refine my thinking process of looking at solution to the problems I faced during my research. I also thank Prof. Shield for letting me use his lab facilities of bulk-sample preparation during the beginning of my research career.

It would be an understatement to thank Dr. Balamurugan Balasubramanian only for helping me throughout my research career as a Ph. D. student. I learned to walk on the path of experimental research holding his hands. From teaching the operation of tools, to understanding and explaining the scientific results, he is the person who guided me in the correct path to succeed in my goals. Hours of working together, even late at nights during difficult periods of my research make me indebted to him forever.

During my research in Prof. Sellmyer's group, I worked with undergraduate student Eric Krage whom I mentored in two summers and those are the two most fun-filled summers I can remember. Thank you, Eric, for working with me more as a friend than a student.

I am indebted to NCMN specialists Dr. Steve Michalski, and Dr. Shah Valloppilly for guiding me with valuable ideas and training me on several lab tools, and Dr. Xinzhong Li for helping me with microscopy measurements. They made me feel as a part of the NCMN team. I also learned a lot about graduate school from Steve, whom I thank for being such a good friend. I am thankful to Zach Sun for helping me with the cluster machine whenever there was a problem. I also want to thank supportive staff members of NCMN, Shelli Krupicka, Terese Janovic and all staffs at the Department of Physics.

I am thankful to present and past group members Dr. Wenyong Zhang, Dr. Tom George, Dr. Rui Zhang and Yunlong Jin for thoughtful discussions about physics and research. I thank Dr. Pinaki Mukherjee and Dr. Priyanka Manchanda for not only helping me in research as colleagues but also being good friends who always gave motivation and positive thoughts.

US-DOE and NSF are appreciated for funding the research through grants.

I am grateful to all my friends in Lincoln, Kaushik and Priyanka, Santanu, Anil, Debalin, Sutanu and Sandrayee who were always with me at times of fun as well as those of stress and doubt.

Last but not least, I want to thank my wife Moumita, my parents, and all other family members and friends who are always with me with their unconditional support.

Table of Contents

| | |
|---|-----------|
| CHAPTER 1. INTRODUCTION | 1 |
| 1.1 Introduction to New Magnetic Materials and Nanoscale Magnetism..... | 1 |
| 1.1.1 Objective: New Magnetic Materials | 1 |
| 1.1.2 Advantages of Nanoclusters over Bulk..... | 2 |
| 1.1.3 Prospects for Nanoscale Magnetism..... | 3 |
| 1.2 Theoretical Background of Magnetic Properties | 4 |
| 1.2.1 Atomic Origin of Magnetism..... | 4 |
| 1.2.2 Ferromagnetism and Hysteresis | 6 |
| 1.2.3 Magnetocrystalline Anisotropy..... | 8 |
| 1.2.4 Stoner-Wohlfarth Model..... | 9 |
| 1.2.5 Exchange Interaction and Curie Temperature | 11 |
| 1.2.6 Energy Product..... | 13 |
| 1.3 Magnetic Nanocomposites | 14 |
| 1.3.1 Hard and Soft Ferromagnets | 14 |
| 1.3.2 Hard-Soft Nanocomposite | 15 |
| 1.4 Summary | 18 |
| | |
| CHAPTER 2. EXPERIMENTAL PROCEDURES | 23 |
| 2.1 Cluster-Deposition Method | 23 |
| 2.1.1 Inert-Gas Condensation | 23 |
| 2.1.2 Deposition of the Nanoclusters and Capping..... | 27 |
| 2.2 Synthesis of Bulk Magnetic Materials | 28 |
| 2.3 X-Ray Diffraction Method | 29 |
| 2.4 Electron Microscopy | 31 |
| 2.5 Magnetic Characterization | 33 |
| 2.5.1 Physical Property Measurement System (PPMS)..... | 33 |
| 2.5.2 Superconducting Quantum Interference Device (SQUID)..... | 35 |

| | |
|---|-----------|
| CHAPTER 3. MAGNETIC ANISOTROPY OF DILUTE Co(Zr) NANOCCLUSERS..... | 40 |
| 3.1 Introduction | 41 |
| 3.2 Synthesis and Alignment of the Nanoclusters..... | 42 |
| 3.3 Results and Discussion..... | 43 |
| 3.4 Conclusions | 48 |
| | |
| CHAPTER 4. Zr₂Co₁₁ -BASED RARE-EARTH-FREE NANOCCLUSERS WITH HIGH ENERGY PRODUCTS | 52 |
| 4.1 Introduction | 53 |
| 4.2 Synthesis of Zr ₂ Co ₁₁ Nanoclusters..... | 54 |
| 4.3 Results | 55 |
| 4.3.1 Structural Properties..... | 55 |
| 4.3.2 Magnetic Properties | 59 |
| 4.3.3 Degree of Magnetic Alignment | 62 |
| 4.4 Discussion | 63 |
| | |
| CHAPTER 5. MAGNETIC PROPERTIES OF Zr₂Co₁₁:Fe-Co NANOCOMPOSITES FABRICATED BY NANOCCLUSER-DEPOSITION..... | 68 |
| 5.1 Introduction | 69 |
| 5.2 Synthesis of the Nanocomposite Cluster Films..... | 71 |
| 5.3 Results and Discussion..... | 73 |
| 5.3.1 Nanostructures of Zr ₂ Co ₁₁ :Fe-Co composite films..... | 73 |
| 5.3.2 Magnetic Properties | 75 |
| 5.3.3 Nanocomposite Model Structure | 76 |
| 5.3.4 Energy Products | 79 |
| 5.4 Conclusions | 81 |
| | |
| CHAPTER 6. SIZE-ENHANCED MAGNETIC PROPERTIES OF Mn AND Fe - BASED SILICIDE NANOCCLUSERS | 84 |
| 6.1 Introduction | 85 |
| 6.2 Structure of Mn ₅ Si ₃ and Fe ₅ Si ₃ Nanoclusters..... | 87 |

| | | |
|--------------------------|---|------------|
| 6.3 | Magnetic Properties: Mn_5Si_3 Nanoclusters | 91 |
| 6.4 | DFT Results for Mn_5Si_3 nanoclusters | 94 |
| 6.5 | Magnetic Properties: Fe_5Si_3 Bulk and Nanoclusters | 96 |
| 6.6 | DFT Study of Fe_5Si_3 nanoclusters..... | 98 |
| 6.7 | Conclusions | 99 |
| CONCLUSIONS | | 103 |
| APPENDIX A | | 105 |
| APPENDIX B | | 107 |
| APPENDIX C | | 109 |

List of Figures and Tables

Chapter 1

| | |
|---|----|
| Figure 1.2.1. Angular (L) and Spin (S) moment with the respective magnetic moments .. | 4 |
| Figure 1.2.2. An example of ferromagnetic hysteresis loops | 7 |
| Figure 1.2.3. Hysteresis loops for a system of Stoner-Wohlfarth grains..... | 10 |
| Figure 1.2.4. Typical variation of magnetization with temperature | 12 |
| Figure 1.2.5. B vs H hysteresis loop for a ferromagnet | 13 |
| Figure 1.3.1. Schematic of exchange-spring magnet..... | 15 |
| Figure 1.3.2. Hysteresis of (a) perfectly exchange coupled and (b) not-coupled magnet | 16 |

Chapter 2

| | |
|--|----|
| Figure 2.1.1. Schematic of a composite target showing the target material | 24 |
| Figure 2.1.2. Cluster deposition system showing three distinct stages..... | 25 |
| Figure 2.2.1. Melt-spinning method to synthesize bulk ribbons of alloys..... | 29 |
| Figure 2.3.1. Bragg's law of diffraction. | 30 |
| Figure 2.5.1. Schematic of a VSM..... | 34 |
| Figure 2.5.2. Diamagnetic m vs H graph of Silicon substrate showing negative slope.... | 38 |

Chapter 3

| | |
|---|----|
| Figure 3.2.1. Magnetic alignment of nanoclusters using two permanent magnets..... | 42 |
| Figure 3.3.1. Structure of Co(Zr) nanoclusters | 44 |
| Figure 3.3.2. LRTEM image of Co(Zr) nanoclusters | 45 |

| | |
|--|----|
| Figure 3.3.3. The expanded room-temperature M-H curves of the aligned nanoclusters | 46 |
| Figure 3.3.4. Variation of (a) H_c and, (b) remanence ratio (M_r/M_s) | 47 |
| Table 3.1. K_u and saturation magnetic polarization J_s of Co(Zr)..... | 48 |

Chapter 4

| | |
|---|----|
| Figure 4.3.1. XRD patterns of Zr_2Co_{11} nanoclusters (red) and bulk (blue) | 55 |
| Figure 4.3.2. Equilibrium phase diagram of Co-Zr. | 56 |
| Figure 4.3.3. LRTEM image of Zr_2Co_{11} nanoclusters | 57 |
| Figure 4.3.4. FESEM images of Zr_2Co_{11} nanocluster films deposited on Si (001) | 58 |
| Figure 4.3.5. Hysteresis loops for Zr_2Co_{11} nanoclusters..... | 60 |
| Figure 4.3.6. Coercivity H_c (red curve) and saturation polarization J_s (green curve)..... | 61 |
| Figure 4.3.7. Degree of magnetic alignment..... | 62 |
| Figure 4.4.1. Energy products..... | 64 |

Chapter 5

| | |
|---|----|
| Figure 5.1.1. Coercivity [H_c ; red curve] and energy product [$(BH_i)_{max}$; blue curve] | 70 |
| Figure 5.2.1. Schematic of the nanocomposite fabrication process..... | 71 |
| Figure 5.3.1. HRTEM image of Zr_2Co_{11} : Fe-Co nanocomposite film..... | 73 |
| Figure 5.3.2. STEM and EDX of Zr_2Co_{11} : Fe-Co nanocomposite film..... | 74 |
| Figure 5.3.3. Magnetic hysteresis loops at room temperature | 75 |
| Figure 5.3.4. Trend of H_c (red curve) and J_s (blue curve) of the Zr_2Co_{11} : Fe-Co..... | 76 |
| Figure 5.3.5. Model nanocomposite structure. | 77 |
| Figure 5.3.6. Energy product at Room Temperature. | 80 |

Chapter 6

| | |
|--|----|
| Figure 6.1.1. D8 ₈ -type hexagonal crystal structure of Mn ₅ Si ₃ | 86 |
| Figure 6.2.1. LRTEM image of (a) Mn ₅ Si ₃ and, (b) Fe ₅ Si ₃ nanoclusters | 87 |
| Figure 6.2.2. HRTEM images of a single nanocluster..... | 88 |
| Figure 6.2.3. XRD of the nanoclusters | 89 |
| Figure 6.2.4. Scanning Transmission Electron Microscopy | 90 |
| Figure 6.3.1. Magnetization (M) measured as a function of temperature (T) | 91 |
| Figure 6.3.2. The magnetic hysteresis loops of the isotropic (unaligned) nanoclusters ... | 92 |
| Figure 6.3.3. Easy-axis aligned Mn ₅ Si ₃ nanoclusters showing in-plane hysteresis loops | 93 |
| Figure 6.4.1. DFT results of Mn ₅ Si ₃ nanoclusters..... | 95 |
| Figure 6.5.1. Magnetic hysteresis of Fe ₅ Si ₃ nanoclusters..... | 96 |
| Figure 6.5.2. Dependence of magnetization on change in temperature..... | 97 |
| Figure 6.6.1. DOS for the Fe atoms | 98 |

CHAPTER 1. INTRODUCTION

1.1 Introduction to New Magnetic Materials and Nanoscale Magnetism

1.1.1 Objective: New Magnetic Materials

Magnetic materials play key roles in next-generation technologies including advanced electronic devices and mechanical applications such as motors and wind turbines.

However, due to ever-increasing demand of magnets and limited resource of critical rare-earth elements it is necessary to design new magnetic materials free of rare-earth and/or expensive elements (e.g. Pt, Pd, etc.).[1,2] This rapidly growing demand for permanent magnets has led to renewed interest in alternative Co- or Fe-rich transition-metal alloys without rare-earth elements, but the synthesis and applications of compounds in this category remains a challenge due to their metastable nature as shown by bulk phase diagrams.[3-7] Alloys of transition metals are potential candidate for magnetic materials with superior magnetic properties due to their electronic structure.[8,9] Few of these alloys possess non-cubic crystal structure essential for high magnetocrystalline anisotropy, a key requirement for permanent magnetism as will be discussed later. In this regard, the Co-rich intermetallic Zr_2Co_{11} compound crystalizing in rhombohedral or orthorhombic structure exhibits high magnetocrystalline anisotropy ($K_1 \approx 20$ Mergs/cm³) and Curie temperature ($T_c \approx 650$ K) suitable for permanent magnets.[3,10,11] For spintronics applications, Si-based magnetic alloys have gained attention in recent years due to their potential applications in semiconductor nano-electronics.[12-14] Mn_5Si_3 and Fe_5Si_3 are two of such alloys which exhibit a hexagonal structure and hence high

anisotropy is possible which helps to obtain thermal stability for potential device applications.[15,16]

The alloys discussed above are predicted and/or partially shown to exhibit promising magnetic properties suitable for high temperature magnetic and spintronics applications and hence are interesting to be studied in detail to understand the spin-physics.[17,18]

1.1.2 Advantages of Nanoclusters over Bulk

New magnetic materials often are in binary-alloy phases which are metastable, i.e. exist in a narrow composition range, and/or require very high temperatures (700 – 1200 °C) for fabrication and stabilization.[7,11,19] For this reason, conventional equilibrium synthesis methods usually lead to impurity phases or an entirely different phase from the one with a desired crystal structure. Non-equilibrium bulk synthesis such as rapid quenching, or chemical synthesis methods might be useful in this process but they may also require very high temperatures or involve multiple steps to prepare the magnetic alloys with high purity.

Fabrication of nanoclusters, which is described in detail in the next chapter, involves a single-step deposition process without use of high temperature melting and gives unique control over phase purity and crystalline ordering. This is a non-equilibrium process which also provides an opportunity to align uniaxial nanoclusters along their easy-axis prior to deposition by applying an external magnetic field (details will be discussed in a later section) which is difficult or not possible for bulk synthesis. Hence, non-equilibrium nanocluster synthesis has emerged as a superior and effective alternative

for fabrication of new and/or metastable magnetic materials, and it also provides an intriguing opportunity to study the spin-physics and riveting properties of magnetism at the nanoscale.

1.1.3 Prospects for Nanoscale Magnetism

Recently, nanoclusters of sizes ≤ 10 nm have been highlighted for their outstanding magnetic properties making them suitable for modern applications.[20,21] These nanocluster building blocks are capable of exploiting the nanoscale effects such as quantum confinement effects on electron spins and surface effects and to improve the magnetic properties beyond their bulk limitations.[22-26] Due to increased surface-to-volume ratio of the nanoclusters compared to that of larger grains of bulk, spin-structures at the nanocluster surfaces are modified and often result in large spin-polarization at the surface due to the low co-ordination number. This leads to high average magnetization of the nanocluster which increases with a decrease of the nanocluster-size and also influences weak ferromagnets or antiferromagnets to exhibit a net magnetization.[27,28]

Nanoscale effects also drive the enhancement of permanent-magnet properties and magnetic anisotropy which can be manipulated by the domain size and magnetocrystalline easy-axis orientation. Usually, the small size of nanoclusters helps to accommodate only a single or small number of ferromagnetic domains which results in high coercivity. Magnetic alignment of the uniaxial easy-axis of nanoclusters along the applied field direction leads to high remanent magnetization and good permanent-magnet properties. Furthermore, nanocomposites of hard-soft magnetic materials are a new pathway for obtaining strong permanent magnets which can be tailored by high-

anisotropy nanoclusters using the magnetic alignment and tuned nanostructuring of the hard and soft magnetic materials.[29,30] This thesis discusses synthesis and analysis of such high-anisotropy magnetic nanoclusters and evaluates their unique spin-structures and magnetic properties for practical applications in modern technologies.

1.2 Theoretical Background of Magnetic Properties

1.2.1 Atomic Origin of Magnetism

Magnetism in solids results mainly from to the electronic orbital and spin motion in an atom.

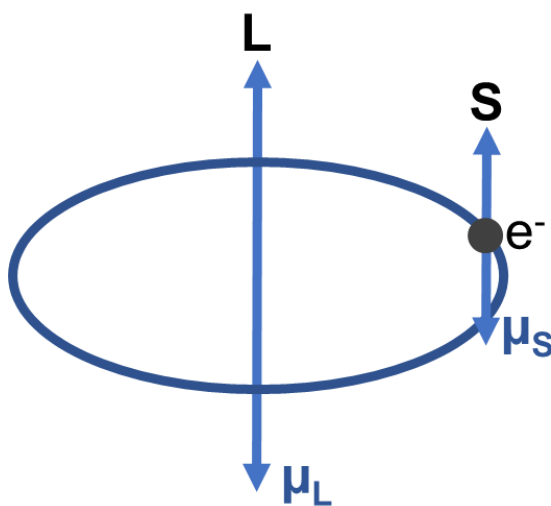


Figure 1.2.1. Angular (L) and Spin (S) moment with the respective magnetic moments (μ_L) and (μ_S) of an electron rotating around nucleus.

Figure 1.2.1 shows the electron motion around nucleus and the corresponding orbital and spin moments. Orbital and spin magnetic moments due to the electron motion is expressed through equations 1.1 and 1.2 respectively.[31]

$$\mu_L = -\frac{e}{2m_e}L = -\frac{e\hbar}{2m_e}\sqrt{l(l+1)} \quad 1.1$$

$$\mu_S = -\frac{e}{2m_e}S = -\frac{e\hbar}{2m_e}\sqrt{s(s+1)} \quad 1.2$$

Here, m_e is the electron mass, l and s are orbital and spin quantum number respectively, and \hbar is $h/2\pi$ where h is Planck's constant. Total angular momentum can be considered as the sum of orbital and spin moment which reduces to the equation 1.3 of effective magnetic moment μ_f .

$$\mu_f = g\frac{e\hbar}{2m_e}\sqrt{j(j+1)} \quad 1.3$$

Here, j is the total magnetic quantum number, and g is a constant known as Landé g factor.[31,32] Magnetic moment of a single electron (orbital or spin) is generally written as Bohr magnetron $\mu_B = \frac{e\hbar}{2m_e}$.

According to Pauli's exclusion principle, only a pair of up and down spins can occupy a single state and hence most of the filled orbital have zero contribution to the spin moment. Thus, only orbitals with partially filled spin states are important for magnetic moment or magnetization of an element. This is the reason for transition metals to contribute to magnetic moment because of the unfilled d – orbitals present in those elements which have unpaired spin states. For these elements, unpaired states of electron

can vary from 1 to 5 leading to as high as $5 \mu_B$ of magnetic moment per atom. But, for a crystallized alloy, atomic orbitals are shared between the consisting atoms which result in much lower values for the average magnetic moment.[8] For a single-crystal nanocluster, the spin-structure at the surface becomes more complicated compared to the bulk which leads to a different average value of the magnetic moment than the bulk crystal, which stimulates more research on nanoscale magnetism.[8,12] In this study, the magnetic moments (magnetization) of transition-metal-based magnetic alloys will be discussed with experimental results and theoretical calculations for nanoscale and bulk materials.

1.2.2 Ferromagnetism and Hysteresis

Ferromagnetism is the material property in which a spontaneous magnetization exists even in the absence of any applied magnetic field. Usually, regions inside such materials form domains in which all spins point along same direction. In case of single crystalline ferromagnetic nanoclusters, each cluster can be regarded as a single domain. For a ferromagnet in applied magnetic field B the Hamiltonian can be written as,

$$H = -\sum_{ij} J_{ij} S_i \cdot S_j + g \mu_B \sum_j S_j \cdot B \quad 1.4$$

Here, J_{ij} is called the exchange constant between the nearest neighbor atoms which is positive in the case of ferromagnets.[32] The first term on the right is the Heisenberg exchange energy and the second term on the right is the Zeeman energy.

Magnetization of a ferromagnet varies with applied magnetic field and undergoes nonlinear transitions and the associated curve is known as the hysteresis loop. Figure

1.2.2 shows a typical hysteresis loop observed in ferromagnets. Each segment of the curve is significant from the viewpoint of spin orientations of the magnetic domains.

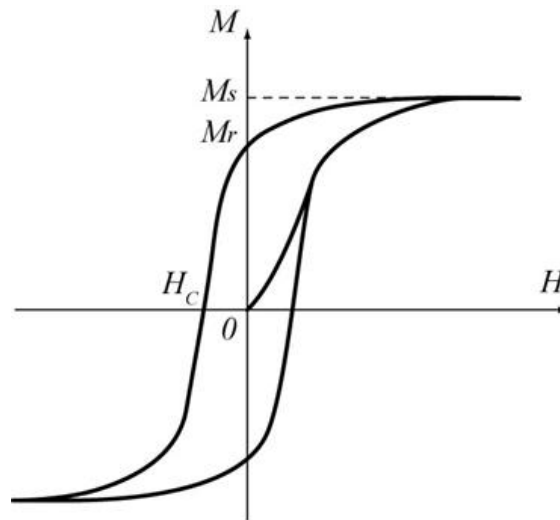


Figure 1.2.2. An example of ferromagnetic hysteresis loops showing different magnetic quantities relevant to a ferromagnet.[33]

At zero applied field, all moments are random and create a net magnetization zero which is at the origin of the curve and the magnet is in the virgin state. An increasing positive applied field begins to align the moments along that direction following the initial magnetization curve starting from the origin. The mechanism of magnetization affects the shape of this curve. Typically, a concave-up curvature indicates a pinning mechanism and concave-down indicates nucleation or rotation. Note that, pinning is defined as locking the motion of the rotation of the magnetic spins (domain-wall-motion) while nucleation relates to the easy-rotation of the spins.[8] At the saturation field, the magnet becomes saturated with the magnetization $M = M_s$ defined as saturation magnetization signifying that all moments are aligned with the applied field. While

reducing the magnetic field, the aligned spins rotate back and at a particular field called the nucleation field (H_N) the magnetization starts to decrease which denotes the knee region of the curve. At zero field the magnitude of magnetization retained is known as the remanent magnetization (M_r). The nonlinear behavior of the curve is defined by the slope $\chi = \frac{dM}{dH}$ and is termed the magnetic susceptibility. For the negative field the moments rotate into the reverse direction and at the coercive field H_c , the averaged moments result in zero magnetization. Further increasing the field along the negative direction gradually saturates the magnet in the fully reversed state. The whole process from negative field back to positive saturation reverses a symmetrical curve as shown in the Fig. 1.2.2. This full cycle of the hysteresis spends energy equal to the area under the curve and usually is dissipated as thermal energy.

1.2.3 Magnetocrystalline Anisotropy

The crystallographic *easy* axis is defined by the preferable direction with respect to the lattice plane directions along which the magnetization tends to align. Crystals with a unique easy axis are called uniaxial crystals and the anisotropy is known as uniaxial anisotropy and is often seen in materials with non-cubic crystal structures such as, hexagonal or rhombohedral structure. The easy axis is generally along the c -axis of the unit cell and the magnetocrystalline anisotropy energy is expressed as,

$$E = K_0 + K_1 \sin^2 \theta + K_2 \sin^4 \theta + \dots \quad 1.5$$

Here, θ is the angle between the magnetization direction and c -axis and K_i ($i = 0, 1, 2, \dots$) are the anisotropy constants for different orders of the equation 1.5.[34] K_0 is neglected

since it is not dependent on angle and if the easy axis is along the c -axis of the crystal, then for small angles, higher order terms are also negligible. Hence, only K_1 is the important term for this kind of materials and known as the magnetocrystalline anisotropy constant which can be measured using various methods (discussed later). For $K_1 < 0$, the basal plane of the crystal plane acts as the *easy*-plane instead of a definite easy-axis and the anisotropy in such cases is known as *easy*-plane anisotropy which is also seen in some non-cubic crystal structure such as hexagonal lattices.[35] Magnetocrystalline anisotropy arises due to spin-orbit coupling which is weak compared to the coupling of orbital motion to the lattice. Hence, if the external field induces rotation to the electron spin, the orbital moment also tends to be rotated and the energy required to break this spin-orbit coupling is referred as anisotropy energy which is basically expressed in equation 1.5 from which it is seen that the energy is proportional to K_1 and hence a measure of this constant gives the strength of magnetocrystalline anisotropy present in the corresponding magnetic material.[34]

1.2.4 Stoner-Wohlfarth Model

A simple model to analyze the hysteresis of ferromagnetic materials with uniaxial anisotropy is to assume it as a system of non-interacting individual grains (or nanoclusters) and this is known as the Stoner-Wohlfarth model. For a single nanocluster, it can be regarded as a single-domain grain which has an easy axis at an angle θ with the applied field (H) direction. If ϕ is the angle between magnetization (M) and the applied field direction, then the average magnetic energy can be written as,[32]

$$E = K_1 \sin^2(\theta - \phi) - \mu_0 H M_s \cos \phi \quad 1.6$$

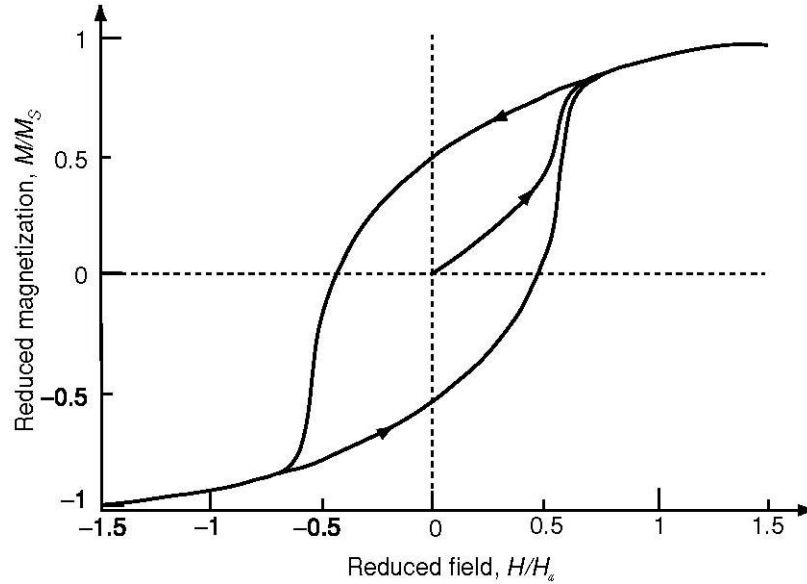


Figure 1.2.3. Hysteresis loops for a system of randomly oriented non-interacting Stoner-Wohlfarth grains.[8]

Figure 1.2.3 shows example of hysteresis for ideal Stoner-Wohlfarth type grains with randomly oriented easy axes which are isolated and non-interacting. It can be seen that, $M_r = M_s/2$ for this kind of granular or nanocluster systems. Here, H_a is the anisotropy field which is similar to H_c (or H_N) for aligned nanoclusters which exhibit a perfect square type hysteresis. Using stability analysis, the energy in Eqn. 1.6 can be reduced to a simple relationship between H_a and K_1 which is expressed as,

$$H_a = \frac{2K_1}{M_s} \quad 1.7$$

This model helps to describe the magnetism of uniaxial nanoclusters which can be magnetically aligned and an estimate of magnetocrystalline anisotropy can be obtained using Eqn. 1.7.[17,32]

1.2.5 Exchange Interaction and Curie Temperature

The exchange interaction is defined by the Coulomb repulsion of two neighboring electrons which, in case of ferromagnets, can happen intra-atomically and is stronger than inter-atomic interaction. According to Pauli's exclusion principle two electrons with same spin cannot be in the same state. There is an energy difference between the interaction of two spin-up states of two neighboring atoms and the interaction between one spin-up and one spin-down state. In general, the total interaction energy for a lattice is expressed by the Heisenberg Hamiltonian written as,[8]

$$H = -2 \sum_{i>j} J_{ij} S_i \cdot S_j \quad 1.8$$

Here, i and j define different lattice sites. In certain cases, the exchange term J_{ij} in Eqn. 1.8 can be simplified to a single term J representing nearest-neighbor interactions.

The exchange constant can be related to the Curie temperature of a ferromagnet in the context of Weiss law in molecular field theory. Curie temperature (T_c) of a ferromagnet is defined as the critical temperature above which the ferromagnet behaves as a paramagnet. The alignment of spins in a ferromagnet is broken at high temperatures where the thermal fluctuations in a lattice dominates over the exchange interaction between the spins. If the interaction between all the spins in a lattice is assumed to be a simple average interaction between only the nearest neighbor spins which can be regarded as an average molecular field, the model is called the mean-field approximation (MFA).[8]

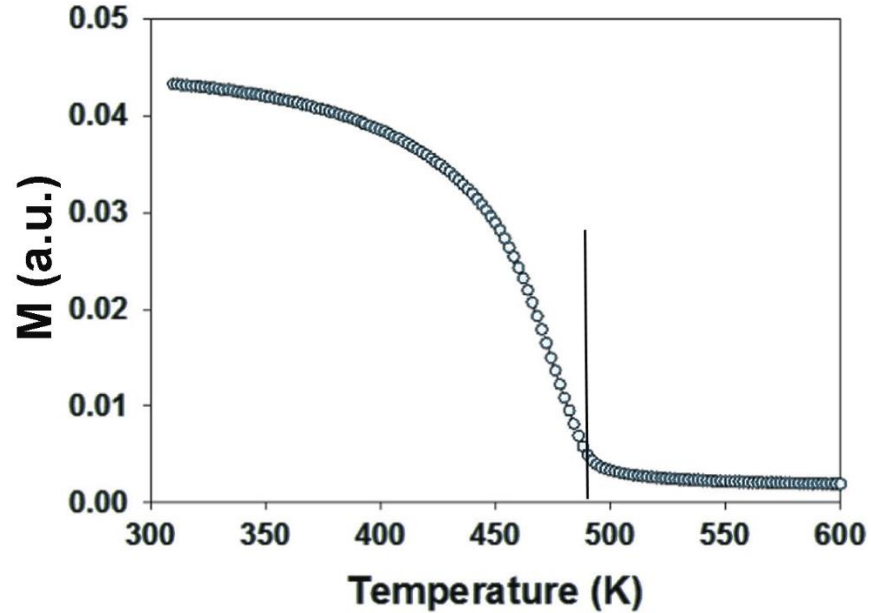


Figure 1.2.4. Typical variation of magnetization with temperature for a ferromagnet. The vertical straight line indicates the Curie temperature.[36]

T_c can be related to the exchange constant J through the MFA which is expressed in eqn. 1.9.[8,36]

$$T_c = \frac{z \times J}{k_B} \quad 1.9$$

Here, z is the number of the first neighbors and k_B is the Boltzmann constant.

Figure 1.2.4 shows the typical graph of variation of magnetization (normalized magnetization) with temperature for two systems with different exchange constants (J). For nanoclusters, often the spins at the surface of a cluster exhibit exchange interactions different from that observed in bulk crystal which gives rise to different value for J than the core or bulk as seen from the eqn. 1.8.[12] From theoretical simulations the value of J

can be obtained for ferromagnetic nanoclusters at the surface and the core which can be used in eqn. 1.9 to estimate the corresponding values for the Curie temperatures. This phenomenon can be used to understand nanoscale surface effects observed in many systems some of which are discussed in this dissertation.

1.2.6 Energy Product

Besides magnetic anisotropy and Curie temperature, the magnetic energy product is another magnetic quantity to determine the strength of a magnet and is the most important figure of merit to categorize permanent magnets. Maximum energy product is the total energy that can be stored in a magnet under a magnetic field and clearly it is related to the hysteresis of the ferromagnet as discussed in Section 1.2.2 only in this case it is important to deal with the magnetic flux density B which is the strength of the magnetization and is expressed as $B = \mu_0 (H+M)$ [$B = H+4\pi M$ in cgs units] where μ_0 is the magnetic permeability of free space.[8,9,32]

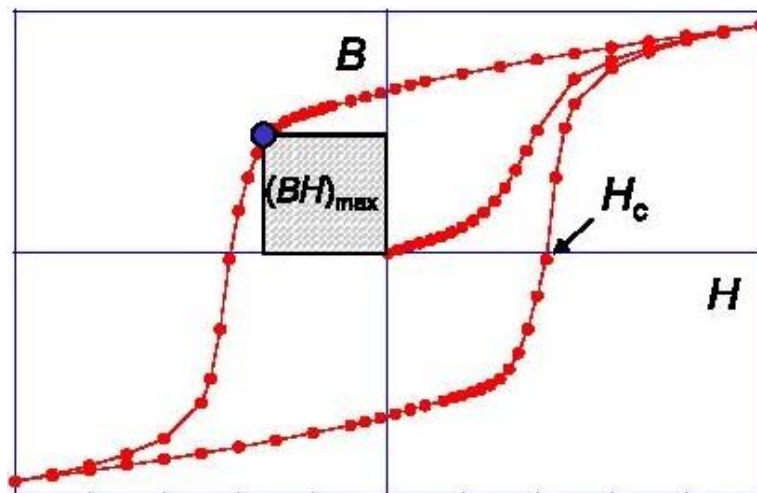


Figure 1.2.5. B vs H hysteresis loop for a ferromagnet showing the maximum energy product $(BH)_{\max}$. [37]

Figure 1.2.5 exhibits a hysteresis loop for B vs applied field H . [37] The energy product is calculated as the maximum of the product of B and H in the second quadrant of this loop as shown by the box. In cgs units, maximum of $BH = H^2 + 4\pi MH$ results in a theoretical value of energy product (when the loop is square and H_c is large) of,

$$(BH)_{\max}^{\text{theo}} = \frac{(4\pi M_s)^2}{4} = \frac{J_s^2}{4} \quad 1.10$$

Thus, the theoretical maximum energy product of a magnet cannot exceed the $\frac{1}{4}$ of square of its saturation magnetic polarization which indicates the necessity of large magnetization for high performance permanent magnets. [8]

1.3 Magnetic Nanocomposites

1.3.1 Hard and Soft Ferromagnets

Ferromagnets are often categorized into three types: hard, soft, and semihard magnets, based on their coercivities. Ferromagnetic materials showing H_c of several kOe usually are hard magnetic since it requires a large reverse applied field to drive the magnetization to zero. Typically, H_c near 3 – 5 kOe or greater is called hard magnetic material. These are often alloy ferromagnets some of which are discussed in this dissertation.

Soft ferromagnets usually have very low or almost zero H_c but often exhibit high magnetization. Ferromagnetic metals like Fe or Co are known soft magnets. Usually the ferromagnetic domains in soft magnets follow nucleation motion without any pinning

which causes the spins to be rotated easily with the applied magnetic field. $\text{Fe}_{65}\text{Co}_{35}$ is an alloy soft magnet which has the highest magnetization among all known materials with a J_S value of about 25 kG and often used as the soft phase in a composite magnet.[8]

1.3.2 Hard-Soft Nanocomposite

Due to comparatively low magnetization in the hard magnetic phase, the energy product of these magnetic materials often does not reach the values desired for high performance magnetic applications. One solution would be to combine the high H_c hard phase with high magnetization soft phase to obtain an optimum energy product. These kinds of composite magnets are known as exchange-spring magnets, a term coined by Kneller *et al.* in 1991.[38] In this paper, the idea was introduced and the mechanism involving the spin structure was explained.

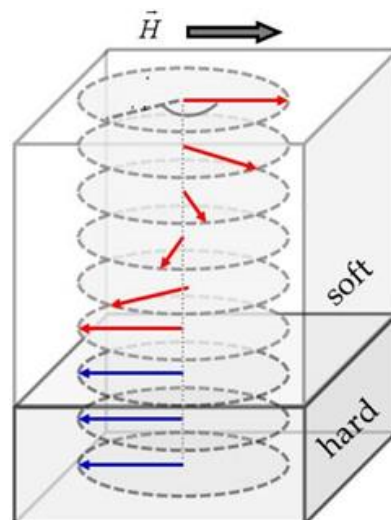


Figure 1.3.1. Schematic of exchange-spring magnet[39]

Figure 1.3.1 shows a schematic of exchange-spring magnet involving hard and soft magnetic phases. In such composites when a magnetic field is reversed from the saturation, the magnetization of the soft phase rotates with the field direction while the hard-phase magnetization remains in the initial saturation direction due to its high magnetocrystalline anisotropy. Hence, after removing the applied field, the soft phase magnetization rotates towards the direction of the magnetization of the hard phase which is basically due to the exchange interaction between the hard and soft phases and this is the reason for the name “exchange-spring” for this configuration.[8,38,39] If the magnetic field is reversed to a high value enough to rotate the hard phase, the total magnetization of the system is reversed.

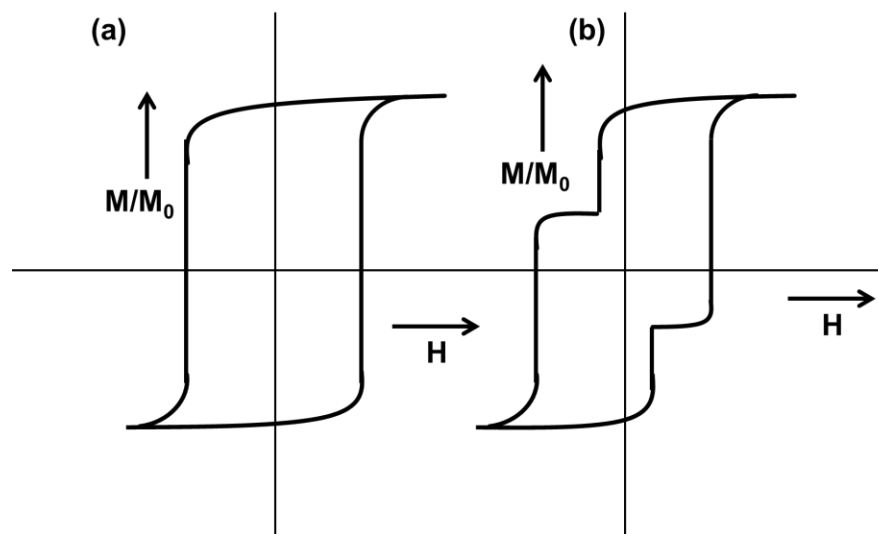


Figure 1.3.2. Hysteresis of (a) perfectly exchange coupled and (b) poorly-coupled hard-soft composites magnet

The hard and soft phases in a composite magnet should be perfectly exchange coupled for the coherent rotation of the magnetization. In the case of poor exchange-coupling or no coupling, the soft phase magnetization rotates with the magnetic field freely while the hard phase magnetization does not change till the applied field exceeds the H_c . This results in two phase behavior in the hysteresis loop with a step. Figure 1.3.2 (a) shows the hysteresis loop for a perfectly exchange coupled composite magnet which is similar to a single phase hard magnet. On the other hand, for poor exchange coupling showing steps in the hysteresis loop for the incoherent hard and soft phases is shown in Fig. 1.3.2 (b). The critical length of the soft phase required for perfect exchange coupling is less than about twice the length of Bloch wall width $\delta_h = \pi\sqrt{A/K_h}$. [38] A Bloch wall is defined as the region where the magnetization changes its value from one domain to the other and A and K_h are the exchange-stiffness constant and magnetic anisotropy constant of the hard phase respectively. [38,40,41]

Usually, the critical length discussed above is within the nanoscale region and producing perfectly exchange coupled magnets are not easy to prepare in bulk form. One solution could be embedding hard magnetic nanoclusters in a soft matrix or coat the hard clusters with the soft phase through controlled synthesis methods. Such, exchange-coupled nanocomposites have potential to obtain high energy product if the hard phase has large uniaxial anisotropy. In this dissertation, magnetism of such nanocomposites is demonstrated using hard Zr_2Co_{11} nanoclusters with $Fe_{65}Co_{35}$ soft magnetic phase.

1.4 Summary

Magnetic nanoclusters are intriguing in the context of studying the magnetic properties described in this chapter. Nanoscale permanent magnets such as $\text{Zr}_2\text{Co}_{11}$ and their nanocomposites as building blocks for magnets with high energy products are interesting to investigate experimentally from the view point of practical applications. Nanoscale effects on spin structure of magnetic materials like Mn_5Si_3 may help to provide a pathway for developing technologies pertinent to spintronics and other devices. This dissertation discusses such magnetic properties at the nanoscale with detailed experimental observations and characterizations and, with the help of DFT calculations, and explains the new findings in terms of the physics of magnetism.

References:

- [1] N. Jones, Materials science: The pull of stronger magnets, *Nature News* **472**, 22 (2011).
- [2] C. T. Yang, While Rare-Earth Trade Dispute With China Heats Up, Scientists Seek Alternatives, *National Geographic News* (2012).
- [3] B. G. Demczyk and S. F. Cheng, Structures of Zr_2Co_{11} and $HfCo_7$ Intermetallic Compounds, *Journal of Applied Crystallography* **24**, 1023 (1991).
- [4] K. Ishida and T. Nishizawa, The Co-Hf (Cobalt-Hafnium) system, *Journal of Phase Equilibria* **12**, 424 (1991).
- [5] M. J. Kramer, R. W. McCallum, I. A. Anderson, and S. Constantinides, Prospects for Non-Rare Earth Permanent Magnets for Traction Motors and Generators, *JOM* **64**, 752 (2012).
- [6] D. Kramer, Concern grows over China's dominance of rare-earth metals, *Physics Today* **63**, 22 (2010).
- [7] H. Okamoto, *Desk handbook: phase diagrams for binary alloys* (ASM International, Materials Park, OH, 2000), Phase diagrams for binary alloys, p. pp. 248, 263, 374, and 560.
- [8] J. M. D. Coey, *Magnetism and magnetic materials* (Cambridge University Press, Cambridge, 2009), 1st edn.
- [9] N. A. Spaldin, *Magnetic materials : fundamentals and applications* (Cambridge University Press, Cambridge, 2011), 2nd edn.
- [10] G. V. Ivanova, N. N. Shchegoleva, and A. M. Gabay, Crystal structure of Zr_2Co_{11} hard magnetic compound, *Journal of Alloys and Compounds* **432**, 135 (2007).
- [11] W. Zhang, S. R. Valloppilly, X. Li, R. Skomski, J. E. Shield, and D. J. Sellmyer, Coercivity Enhancement in Zr_2Co_{11} -Based Nanocrystalline Materials Due to Mo Addition, *IEEE Transactions on Magnetism* **48**, 3603 (2012).
- [12] B. Balasubramanian, P. Manchanda, R. Skomski, P. Mukherjee, B. Das, T. A. George, G. C. Hadjipanayis, and D. J. Sellmyer, Unusual spin correlations in a nanomagnet, *Applied Physics Letters* **106** (2015).
- [13] L. Liao, Y-C. Lin, M. Bao, R. Cheng, J. Bai, Y. Liu, Y. Qu, K. L. Wang, U. Huang, and X. Duan, High-speed graphene transistors with a self-aligned nanowire gate, *Nature* **467**, 305 (2010).

- [14] A. Fert, V. Cros, and J. Sampaio, Skyrmions on the track, *Nature Nanotechnology* **8**, 152 (2013).
- [15] C. Surgers, G. Fischer, P. Winkel, and H. V. Lohneysen, Large topological Hall effect in the non-collinear phase of an antiferromagnet, *Nature Communications* **5** (2014).
- [16] P. C. Srivastava and J. K. Tripathi, Giant magnetoresistance (GMR) in swift heavy ion irradiated Fe films on c-silicon (Fe/c-Si), *Journal of Physics D-Applied Physics* **39**, 1465 (2006).
- [17] J. M. D. Coey, Permanent magnets: Plugging the gap, *Scripta Materialia* **67**, 524 (2012).
- [18] M. A. McGuire, in *Vehicle Technologies Office: Annual Merit Review Presentations* (US Department of Energy, 2011).
- [19] K. H. J. Buschow, Differences in magnetic properties between amorphous and crystalline alloys, *Journal of Applied Physics* **53**, 7713 (1982).
- [20] B. Balamurugan, D. J. Sellmyer, G. C. Hadjipanayis, and R. Skomski, Prospects for nanoparticle-based permanent magnets, *Scripta Materialia* **67**, 542 (2012).
- [21] D. J. Sellmyer and R. Skomski, *Advanced magnetic nanostructures* (Springer, New York, 2006).
- [22] G. Reiss and A. Hutten, Magnetic nanoparticles: applications beyond data storage, *Nature Materials* **4**, 725 (2005).
- [23] D. J. Sellmyer, Applied physics: Strong magnets by self-assembly, *Nature* **420**, 374 (2002).
- [24] B. Balasubramanian, R. Skomski, X. Li, S. R. Valloppilly, J. E. Shield, G. C. Hadjipanayis, and D. J. Sellmyer, Cluster synthesis and direct ordering of rare-earth transition-metal nanomagnets, *Nano Letters* **11**, 1747 (2011).
- [25] S. Sun, C. B. Murray, D. Weller, L. Folks, and A. Moser, Monodisperse FePt nanoparticles and ferromagnetic FePt nanocrystal superlattices, *Science* **287**, 1989 (2000).
- [26] D. Alloyeau, C. Ricolleau, C. Mottet, T. Oikawa, C. Langlois, Y. Le Bouar, N. Braidy, and A. Loiseau, Size and shape effects on the order-disorder phase transition in CoPt nanoparticles, *Nature Materials* **8**, 940 (2009).

- [27] I. M. L. Billas, J. A. Becker, A. Châtelain, and W. A. de Heer, Magnetic moments of iron clusters with 25 to 700 atoms and their dependence on temperature, *Physical Review Letters* **71**, 4067 (1993).
- [28] P. D. Dimple, S. Garima, P. K. Manna, A. K. Tyagi, and S. M. Yusuf, Room temperature ferromagnetism in CoO nanoparticles obtained from sonochemically synthesized precursors, *Nanotechnology* **19**, 245609 (2008).
- [29] H. Zeng, J. Li, J. P. Liu, Z. L. Wang, and S. Sun, Exchange-coupled nanocomposite magnets by nanoparticle self-assembly, *Nature* **420**, 395 (2002).
- [30] X. Rui, J. E. Shield, Z. Sun, Y. Xu, and D. J. Sellmyer, In-cluster-structured exchange-coupled magnets with high energy densities, *Applied Physics Letters* **89**, 122509 (2006).
- [31] R. C. O'Handley, *Modern magnetic materials : principles and applications* (Wiley, New York, 2000).
- [32] S. Blundell, *Magnetism in condensed matter* (Oxford University Press, Oxford ; New York, 2001), Oxford master series in condensed matter physics.
- [33] D. R. Khokhlov and D. D. Zaitsev, Ferromagnets, <http://eng.thesaurus.rusnano.com/wiki/article1873>.
- [34] B. D. Cullity, *Introduction to magnetic materials* (Addison-Wesley Pub. Co., Reading, Mass., 1972), Addison-Wesley series in metallurgy and materials.
- [35] B. Balasubramanian, P. Manchanda, R. Skomski, P. Mukherjee, S. R. Valloppilly, B. Das, G. C. Hadjipanayis, and D. J. Sellmyer, High-coercivity magnetism in nanostructures with strong easy-plane anisotropy, *Applied Physics Letters* **108** (2016).
- [36] R. Y. Díaz, Modeling of macroscopic anisotropies, <http://www.fgarciasanchez.es/thesisrocio/node1.html>.
- [37] J. M. D. Coey, New permanent magnets; manganese compounds, *Journal of Physics: Condensed Matter* **26**, 064211 (2014).
- [38] E. F. Kneller and R. Hawig, The Exchange-Spring Magnet - a New Material Principle for Permanent-Magnets, *IEEE Transactions on Magnetics* **27**, 3588 (1991).
- [39] O. Yalçın, *Ferromagnetic Resonance 2013*, Ferromagnetic Resonance - Theory and Applications.
- [40] R. Skomski and J. M. D. Coey, Giant Energy Product in Nanostructured 2-Phase Magnets, *Physical Review B* **48**, 15812 (1993).

- [41] S. Nieber and H. Kronmüller, Nucleation Fields in Periodic Multilayers, *Physica Status Solidi B-Basic Research* **153**, 367 (1989).

CHAPTER 2. EXPERIMENTAL PROCEDURES

2.1 Cluster-Deposition Method

2.1.1 Inert-Gas Condensation

Inert-gas condensation method (IGC) is a bottom-up approach for nanocluster synthesis in which evaporated materials aggregate to form a cluster of atoms and each of these clusters is often regarded as a nanoparticle or a nanocluster. The gas-aggregation method, first developed by Haberland *et al.* is based on IGC and is widely used for gas-phase synthesis of nanoclusters. [1,2] It involves two important stages to synthesize nanoclusters which are, first, vaporizing the materials to form the gas phase and second, rapid condensation in a controlled manner to form nanoclusters of desired sizes. Using the gas-aggregation method, nanoclusters of different sizes can be fabricated ranging from few hundreds to several thousands of atoms per cluster. [1] The desired sizes can be obtained by optimizing several parameters and experimental conditions during the fabrication process.

Vaporization of the materials is usually performed by magnetron sputtering which involves bombarding the solid surface of the target with high-velocity ions of an inert gas to eject atoms from the surface. The target is made to the desired composition in two ways: (a) alloying stoichiometric elements, and (b) inserting pellets of a second element into a disk of another constituent element on the sputtering race-track as shown in Fig.

2.1.1. The race-track is a circular shell on the target with maximum probability of sputtering.

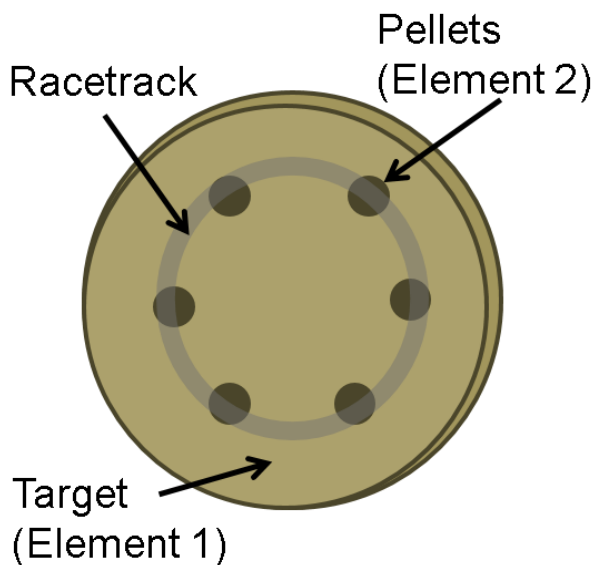


Figure 2.1.1. Schematic of a composite target showing the target material (element 1 such as Co, Fe or Si), pellets or plug inserts (element 2 such as Zr, Mn etc.) and the sputtering race-track.

The schematic of the cluster-deposition system is shown in Fig. 2.1.2 which has three major sections. First, a DC magnetron sputtering chamber capable of sputtering from a 3 -inch target. Second, a gas-aggregation chamber with a fluid jacket to cool and maintain the temperature of the walls and, third, a deposition chamber containing a substrate and a rotatable substrate holder. The effective volume of the aggregation chamber can be varied by moving the magnetron holder using a screw-rail linear actuator and can be used as a parameter for cluster deposition.

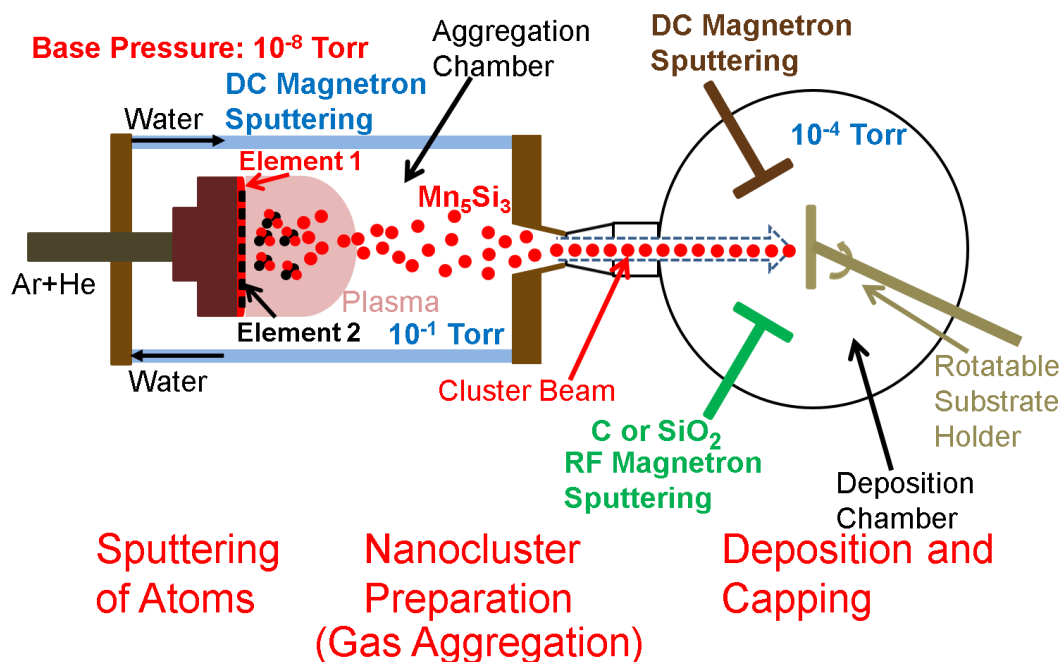


Figure 2.1.2 Cluster deposition system showing three distinct stages of the nanoclusters fabrication process.

The inert gas used in the sputtering process is a mixture of argon and helium, where Ar acts as the sputtering gas by producing high-energy ions and the He helps as a carrier fluid of the sputtered atoms to travel into the nucleation chamber and maintains a uniform temperature in the aggregation process and hence acts as one of the parameters to control the nanocluster size. The ionization gas near the magnetron is exposed to very high electric field by application of high-voltage (DC) from external power source. This helps to ionize the gas which, along with the sputtered material-atoms and electrons, form a plasma near the surface of the target which also acts as one of the electrode. The magnetic field of the magnetron, arising from a pair of strong circular-cylindrical magnets behind the target, helps to confine the plasma within a small region near the

race-track to ensure large number of collisions and ejection of more atoms. During the sputtering process the gas pressure in the chamber is typically $1 - 10^{-1}$ torr while the pressure in the deposition chamber lies in the range $10^{-3} - 10^{-4}$ torr. Due to differential gas pressure between the chambers, the ejected atoms travel into the cold aggregation chamber which is cooled either using liquid N_2 ($-130^\circ C$) or water depending on the experimental requirements. The neutral inert-gas atoms collide with the ejected-material atoms and absorb their energy; on the other hand, the inert-gas atoms lose energy by coming in contact with the cold aggregation chamber. This leads to formation of nucleation center by bonding between the material atoms which eventually grows to form a nanocluster. [3] Using very high sputtering-power (typically in the range between 150 – 250 Watts depending on the target material), the material atoms can be excited to very high energy which is absorbed in the gas-aggregation chamber during the above-mentioned collision process and this leads to rapid change in thermal energy during the formation of the nucleation center. This non-equilibrium process leads to direct crystallization similar to rapid thermal annealing and helps to obtain nanoclusters with a high degree of atomic ordering.[4] The amount of nanoclusters produced, their size and size distribution can be controlled by varying the different parameters such as flow rate of sputtering gas, volume of the gas-aggregation chamber, applied voltage or power in the magnetron and temperature of the aggregation chamber.

The flow rate of the sputtering gas (Ar) is usually measured in the units of SCCM (standard cubic centimeter per minute) and can be controlled using a gas flow controller. The higher flow rate of Ar ensures a high cooling rate which leads to formation of

nucleation sites in large numbers and hence more clusters with smaller sizes are obtained compared to smaller number of clusters having larger sizes formed due to lower flow rate of Ar. Also, the volume of the aggregation chamber plays key role in determination of the cluster-size by controlling the condensation environment. The size of the nanoclusters also decreases with reduction of the volume of the aggregation chamber due to a smaller number of collisions between the clusters and/or between the clusters and the atoms and *vice versa*. [5] The nanoclusters are drifted towards the deposition chamber by the differential gas pressure between the chambers through a small nozzle (diameter of about 1 mm) opening at the end of the gas-aggregation chamber. The opening can be reduced or increased externally by using a rotator and this helps to control the gas pressure inside the aggregation chamber, keeping the flow rate constant which acts as a parameter for the number of nanoclusters to form and exit the aggregation chamber.

2.1.2 Deposition of the Nanoclusters and Capping

The nanoclusters produced in the gas-aggregation chamber are extracted as a collimated beam towards the deposition chamber as shown in the Fig. 2.1.2 and deposited on the substrate. The substrate(s) on the substrate holder is preloaded in the load lock chamber so that the load lock chamber can be evacuated first after which the substrate is introduced in the deposition chamber without disturbing vacuum of the rest of the system. Usually a single crystalline silicon (Si) substrate with (001) orientation was used for the X-ray diffraction and magnetometry studies. For transmission-electron-microscopy studies thin carbon coated copper grid was used as a substrate on which a very thin layer of the nanoclusters was deposited. Since the nanoclusters are more sensitive to total

oxidation due to high surface area (or high surface-to-volume ratio), the clusters were protected from the atmosphere using a capping layer of either carbon (graphite) or SiO₂ with a layer-thickness of about 5 nm using a RF magnetron gun employed in the deposition chamber. The rotatable substrate holder helps in this step to expose the deposited nanoclusters towards the beam of capping material. The deposition chamber is also equipped with a DC sputtering gun capable of holding a 2 -inch target which can be used to deposit thin films of metallic materials for different purposes like creating metallic buffer layers or making nano-composites which will be discussed in later sections. The mass or the nominal thickness of the deposited nanocluster films on the substrates is measured using a quartz-crystal thickness monitor which can also be used to measure the nominal thickness of the cap layer or metal films (if necessary).

2.2 Synthesis of Bulk Magnetic Materials

Preparation of bulk magnetic alloys involves two major processes. At first, stoichiometrically weighed high-purity elements are melted in an argon atmosphere using arc-melting furnace. The melting is done repeatedly (about 4 times) to get homogeneously mixed ingots. The weight loss after melting is less than 0.5% in each composition of materials. In the second step, the arc-melted ingots are placed in a quartz crucible with an orifice of 0.5 – 0.75 mm and melted again using an induction furnace in argon atmosphere. The melt of the ingot is shot at high pressure through the orifice onto a water-cooled copper wheel rotating at a desired speed in the range of 22 - 57 m/s which

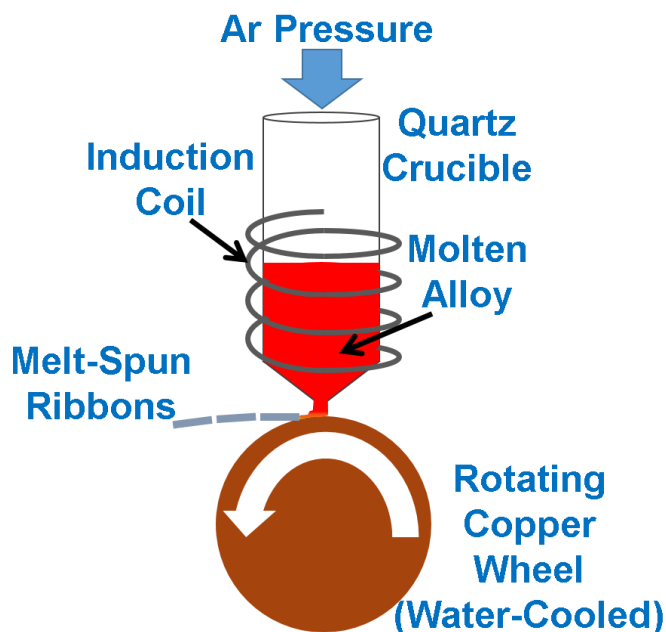


Figure 2.2.1. Melt-spinning method to synthesize bulk ribbons of alloys

forms ribbons of the materials as shown in Fig. 2.2.1, and the ribbons are collected in a chamber kept at room temperature. This method promotes rapid quenching which is a necessary step to form metastable phases using a non-equilibrium method. The phase, composition and magnetic properties of the ribbons or their mechanically milled powders are investigated using various analytical instruments mentioned in the following section.

2.3 X-Ray Diffraction Method

X-ray diffraction of nanocluster films and of the bulk samples were performed using Rigaku (D/MaxB) X-ray diffractometer in 2θ - θ mode with the Cu-K α and/or Co-K α radiation. X-rays are electromagnetic radiation with wavelength near 1.5 Å and generated

by impact of high energy electrons with a material target. The characteristic spectrum of x-ray ($K\alpha$ –lines), which is formed usually by filling up the electron-deficiency created in the impacted material by the previous electron bombardment, is most important for crystallographic studies using x-rays since they are monochromatic. The wavelength of the characteristic x-rays depends on the source, for example Cu- $K\alpha$ lines have a wavelength of 1.54 Å or Co- $K\alpha$ lines have a wavelength of 1.79 Å. The x-rays are diffracted from the lattice planes present in the crystalline materials and the diffraction follows Bragg's law:

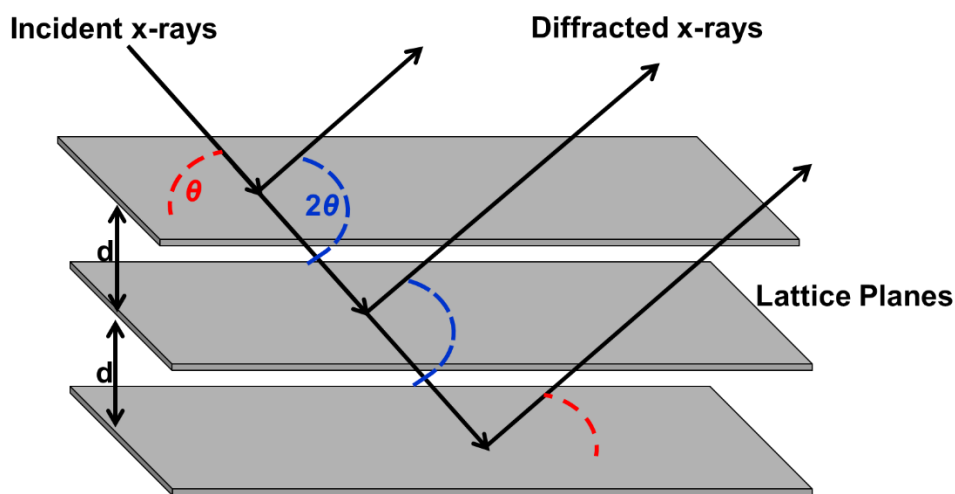


Figure 2.3.1. Bragg's law of diffraction. X-rays are incident at angle θ in the lattice plane and are diffracted at angle 2θ with respect to the incident direction

$$2d \sin\theta = n\lambda$$

2.1

Here, d is the spacing between the lattice planes as shown in Fig. 2.3.1, λ is the wavelength of the x-rays, θ is the incident angle of the x-rays and n is the order of diffraction which is typically taken as unity.[6] The diffraction peaks obtained from an x-

ray diffraction (XRD) pattern exhibit the corresponding lattice planes and the peak intensities depend on the structural symmetries with respect to the lattice sites. The atomic structure factor plays an important role in determining the intensity and the locations of the XRD peaks and often relies on the chemical sensitivity of x-rays. The width of the principal reflection peak is often used to determine the size of the crystallites (single-crystalline grain) present in a polycrystalline sample using Scherrer's equation:

$$\sigma = \frac{K\lambda}{B\cos\theta} \quad 2.2$$

where, K is a constant shape factor typically chosen as 0.9, B is the full width at half-maximum (FWHM) of the principal XRD peak and σ is the average size of the grain or crystallite.[6]

2.4 Electron Microscopy

Electron microscopy mainly consists of two types, one being scanning electron microscopy (SEM) and the other transmission-electron-microscopy (TEM). SEM is used to investigate surface properties, morphology or thickness (of films) of the samples whereas, TEM is often used to determine the crystal structure.

In the case of SEM, electrons originated from a cathode are accelerated through high energy in the range between 10 to 20 keV which come as a collimated beam to strike the surface of the sample. Because of the collision of this beam with the surface, secondary electrons are generated near the surface of the sample containing details of the

surface morphology. Detectors of the secondary electrons are then used to obtain this information and then convert them into images using a computer.[7] In this study, a FEI Nova NanoSEM450 is used which does not need any special sample-preparation procedure. The sample is usually mounted on the metal holders provided with the system which are transferred into the SEM chamber without breaking the vacuum, and installed on the stage for studying the properties of the sample surfaces.

TEM, on the other hand, uses higher energy in the range of 100 to 200 keV to accelerate the electrons emitted from field-emission gun. Electrons are transmitted through the thin samples (~10 nm) and carry structural information of the crystalline sample which are detected using various detectors. In high resolution TEM (HRTEM) diffraction of electrons from the lattice of crystalline samples produce patterns related to the crystal structure of the sample (size can be down to dimensions in the order of few Angstroms) which can be reproduced using fast Fourier transform (FFT) of the lattice image. High-angle-annular dark field (HAADF) studies also can be done using TEM where the electrons scattered from the lattice of the sample are detected at a high angle relative to the electron beam and due to their incoherent nature the detection is very sensitive to the atomic number (Z) of the sample.[8] Hence, HAADF images of the sample contain different contrast according to the Z of the elements present in the sample, where low contrast variation in the image indicates homogeneous elemental distribution over the sample dimension. High-energy electrons often excite ground state electrons residing in inner regions of the atoms of the sample so that they can be ejected from the shell. One electron from the outer shell can decay to fill the hole (electron

deficiency in the inner shell) and the energy released from this process as an x-ray excitation whose wavelength corresponds to the difference in the energy between the two shells. This x-ray is detected and energy dispersive x-ray (EDX) spectroscopy is used to analyze the EDX spectra to determine chemical composition of the sample. Often, EDX color maps are used to visualize the elemental distribution over the sample where different colors can be used to identify different elements present in the sample. An FEI Tecnai Osiris (Scanning) Transmission Electron Microscope was used for all the measurements on the nanoclusters deposited on the copper grid substrate. Low resolution TEM was used to obtain an overall image to calculate the size distribution of the nanoclusters, whereas HRTEM, HAADF and EDX spectroscopy were used for structural characterization and composition analysis.

2.5 Magnetic Characterization

2.5.1 Physical Property Measurement System (PPMS)

PPMS is used to measure magnetic properties using the Vibrating Sample Magnetometer (VSM) mode. In VSM, the sample is vibrated in a uniform magnetic field which changes the magnetic flux and the flux-change is detected by a set of pick up coils situated close to the sample.[9] A schematic of the VSM technique is shown in Fig. 2.5.1. The magnetic signal generated in this process is sensitive to the magnetization of the sample and the corresponding magnetic moment is measured as output.

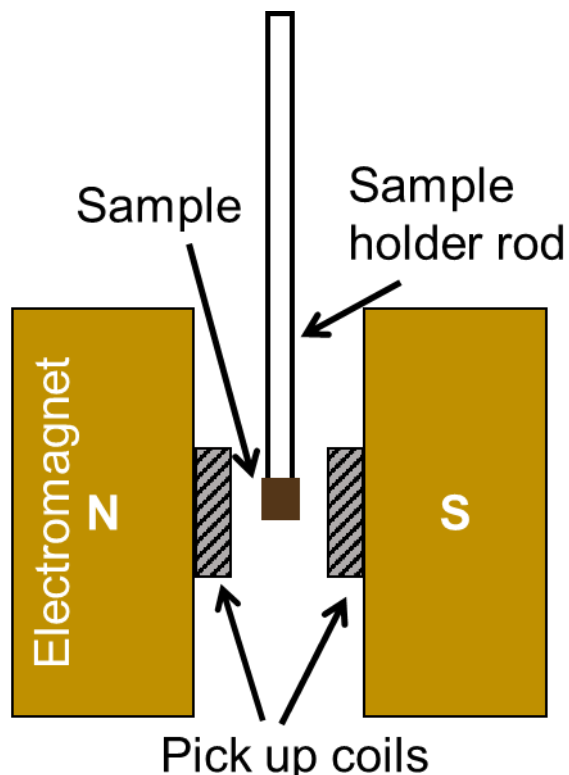


Figure 2.5.1. Schematic of a VSM. Sample is mounted in the middle of the magnetic pole pieces and the pick-up coils

In this study, PPMS from Quantum Design is used in VSM mode mostly to study high temperature magnetic properties using a heater oven. The oven is connected to the sample rod which holds the sample holder. A sample with dimension of about 2 mm is mounted on the heater coils of the oven using zirconia cement and a wrapping of copper foil is used for homogeneous heat conduction across the sample. The oven operates in the temperature range of 300 – 900 K under the vacuum of the sample chamber with a pressure of about 10^{-5} torr. Variation of magnetic moment with temperature is studied often under a small magnetic field to obtain good moment signal from the sample. The

VSM used in the PPMS is sensitive up to a small magnetic moment of the order of 10^{-6} emu.

2.5.2 Superconducting Quantum Interference Device (SQUID)

A SQUID magnetometer implements the quantum interference effect of a Josephson junction for precise measurement of the magnetic signal (moment) produced by superconducting detection coils. A Josephson junction is two superconductors at different phases separated by an insulator at the junction through which Cooper pairs with different phases can tunnel producing a current flow. The current across the Josephson junction in presence of a magnetic field $\mathbf{B} = \nabla \times \mathbf{A}$ given by:

$$\mathbf{j} = j_0 \sin(\gamma_a - \gamma_b - \frac{2e}{\hbar} \int_a^b \mathbf{A} \cdot d\mathbf{l}) \quad 2.3$$

where γ_a, γ_b are the phases of the superconducting-state wave functions for the two superconductors a and b in the Josephson junction, and we can assume, $\gamma_a - \gamma_b = \delta$. [10] \mathbf{A} is the magnetic vector potential, j_0 is the maximum current which depends on the charge densities of the two superconductors and the coupling strength between them. It can be noticed that even if there is no \mathbf{A} , the current is not zero. Integrating the current density of Eqn. 2.3 across the junction gives the total current I and is given by:

$$I = I_0 \frac{|\sin(\frac{\phi e}{\hbar})|}{\frac{\phi e}{\hbar}} |\sin \delta| \quad 2.4$$

Here ϕ is the flux contained in the current carrying region of the junction. Hence the current will vary with change in ϕ in a similar way like, optical single-slit diffraction

pattern. This diffraction phenomenon can be analyzed by taking the integration of Eqn. 2.3 along all the possible paths across the junction where each individual path takes on different phase shifts due to the vector potential \mathbf{A} . Note that, the current becomes zero for $\phi = \frac{n\pi\hbar}{e}$ and this quantized flux element is denoted as $\phi_0 = \frac{\pi\hbar}{e}$. So, interference occurs whenever a new flux quantum is created (a new phase difference) by the magnetic field and the tunneling current is cut off. For more than one junction the variation of current simply follows the equation:

$$I \simeq I_0 \frac{|\sin(\frac{\phi e}{\hbar})|}{\frac{\phi e}{\hbar}} \left| \sin(\Delta\delta - \frac{\phi_T e}{\hbar}) \right| \quad 2.5$$

where ϕ is the flux trapped in each junction and ϕ_T is the total flux across the junction.[10] $\Delta\delta$ is the change in phase difference between two junctions. Hence, the signal detected by the SQUID pick-up coils leading to the current I (Eqn. 2.5) due to change in the flux-quantum is precisely detected in the case of DC or in case of AC, the Josephson junction oscillates with a characteristic frequency corresponding to the variation in flux-quantum and the voltage created across the junction encodes the magnetic signal.

In this study, a magnetic property measurement system (MPMS) SQUID from Quantum Design is used in which a maximum magnetic field of 70 kOe can be applied and measurements can be done at a large temperature range from 2 K to 400 K. A magnetic moment of as low as 10^{-8} emu can be detected using the SQUID which operates in three modes of magnetic field variation namely no overshoot, hysteresis and oscillation

modes. The overshoot mode is ideal for a magnetic field which should be strictly restricted to its set value and not beyond which makes the set time for the desired field value longer to obtain the most accurate field value. In case of hysteresis mode, the magnetic field is swept much faster than the no-overshoot mode so that the field can reach within 3 % of its set value faster. Due to the fast sweeping of magnetic field in the hysteresis mode, consumption of liquid ^4He by the superconducting magnets becomes high. In the oscillation mode, as the name suggests, the magnetic field is allowed to oscillate around the set value up to a range of 30 % which reaches the set point by decaying the oscillation. Measurements not suitable for exposure to large field variation at each data point should not be run under the oscillation mode. Most of the magnetic measurements performed in this study are done in the no-overshoot mode for better accuracy of the data.

Samples used for SQUID measurements are about 50 – 100 nm thick and cut with a dimension of about 6 mm x 6 mm in the case of nanoclusters films and gelatin capsule of diameter 5 mm are used to hold bulk samples. The magnetic moment obtained from SQUID either from moment m vs. applied magnetic field H hysteresis measurements, or from m vs T data contain the diamagnetic signal from the substrate or the capsule holder which must be corrected to obtain accurate results related to the sample under investigation. The magnetic moment from the bare substrate or the empty capsule is measured and m vs. H data is obtained which shows diamagnetic variation of m with H as shown in Fig. 2.5.2.

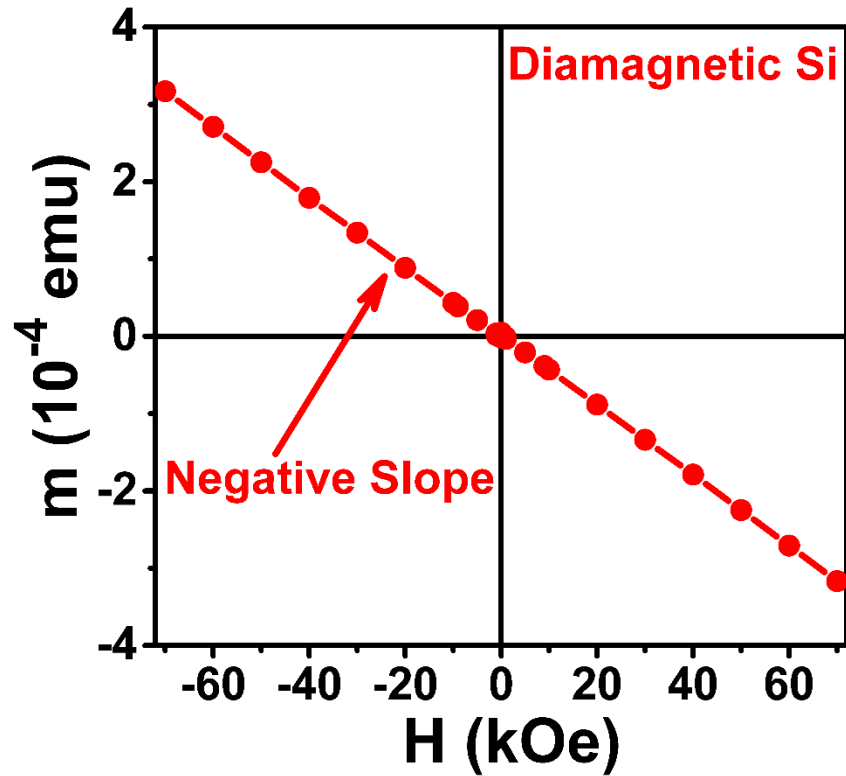


Figure 2.5.2. Diamagnetic m vs H graph of Silicon substrate showing negative slope.

The negative slope of the diamagnetic hysteresis loop is calculated from m vs. H graph and the slope is deducted from that at the high field region of the hysteresis loop obtained for the magnetic sample. The effective curve after this slope correction represents the magnetic hysteresis for the sample and is converted to magnetization M vs. H curve with proper weighting factor such as mass or volume of the sample.

References:

- [1] H. Haberland, M. Karrais, M. Mall, and Y. Thurner, Thin films from energetic cluster impact: A feasibility study, *Journal of Vacuum Science & Technology A* **10**, 3266 (1992).
- [2] J. P. Wilcoxon and B. L. Abrams, Synthesis, structure and properties of metal nanoclusters, *Chemical Society Reviews* **35**, 1162 (2006).
- [3] K. R. Bray, C. Q. Jiao, and J. N. DeCerbo, Nucleation and growth of Nb nanoclusters during plasma gas condensation, *Journal of Applied Physics* **113**, 234307 (2013).
- [4] B. Balasubramanian, R. Skomski, X. Li, S. R. Valloppilly, J. E. Shield, G. C. Hadjipanayis, and D. J. Sellmyer, Cluster Synthesis and Direct Ordering of Rare-Earth Transition-Metal Nanomagnets, *Nano Letters* **11**, 1747 (2011).
- [5] T. Hihara and K. Sumiyama, Formation and size control of a Ni cluster by plasma gas condensation, *Journal of Applied Physics* **84**, 5270 (1998).
- [6] B. D. Cullity, *Elements of X-ray diffraction* (Addison-Wesley Pub. Co., Reading, Mass., 1956), Addison-Wesley metallurgy series.
- [7] T. E. Everhart and R. F. M. Thornley, Wide-band detector for micro-microampere low-energy electron currents, *Journal of Scientific Instruments* **37**, 246 (1960).
- [8] D. E. Jesson and S. J. Pennycook, Incoherent Imaging of Crystals Using Thermally Scattered Electrons, *Proceedings of the Royal Society of London. Series A: Mathematical and Physical Sciences* **449**, 273 (1995).
- [9] S. Foner, Versatile and Sensitive Vibrating-Sample Magnetometer, *Review of Scientific Instruments* **30**, 548 (1959).
- [10] R. C. Jaklevic, J. Lambe, A. H. Silver, and J. E. Mercereau, Quantum Interference Effects in Josephson Tunneling, *Physical Review Letters* **12**, 159 (1964).

CHAPTER 3. MAGNETIC ANISOTROPY OF DILUTE Co(Zr) NANOCLUSTERS

Ferromagnetic materials with non-cubic structures are important to study due their potential for high magnetocrystalline anisotropy. Cobalt (Co) is a simple example of such materials with hcp (hexagonal close-packed) structure. However, Co also exists in f.c.c (face-centered-cubic) form and often these two phases co-exist at nanoscale. In this study, stabilization of hcp Co phase in the form of nanoclusters with addition of a third element zirconium (Zr) is discussed and magnetic alignment of these nanoclusters are demonstrated.

Many of the results presented in this chapter are adapted from the publication: “Structure and magnetism of dilute Co(Zr) nanoclusters.” B. Das, B. Balamurugan, R. Skomski, X. Z. Li, P. Mukherjee, G. C. Hadjipanayis and D. J. Sellmyer, *Journal of Applied Physics*, 113, 17B509 (2013).

I performed the synthesis and characterization of the Co(Zr) nanoclusters. R. Skomski helped with the theoretical explanations. and X. Z. Li and P. Mukherjee helped with the TEM measurements. All co-authors contributed to the final manuscript.

3.1 Introduction

Recently, simple ferromagnetic nanoclusters such as Fe or Co doped with substitutional or interstitial additives have gained significant interests – in order to create nanocluster building blocks with improved magnetic anisotropies for alternative permanent-magnet materials. Also, they are of potential interest from the viewpoint of understanding the physical significance behind the modified properties.[1-3] It is worth noting that experimental and theoretical investigations on bulk and thin films of Fe and Co have already shown appreciable changes in their magnetic properties on doping with heavy transition metals.[4-6]

Studying the magnetic anisotropy of diluted magnetic nanoclusters requires precise control over the phase purity as well as crystalline ordering which influences the magnetocrystalline anisotropy for uniaxial crystal structures. Co is known to have hexagonal close packed (hcp) structure which is of high symmetry and uniaxial as well as face-centered cubic (fcc) structure. Promoting growth of only the hcp structure is important which can be done with heavy transition metal, like Zr, since it also has hexagonal crystal structure and also, being a $4d$ -transition metal, it may help to improve the magnetocrystalline anisotropy. In this study, Co nanoclusters with dilute Zr addition are synthesized using the cluster-deposition method and their structure and magnetic properties are investigated.

3.2 Synthesis and Alignment of the Nanoclusters

Co and Co(Zr) nanoclusters are synthesized using the gas-aggregation type cluster-deposition method described in the Chapter 2. A composite target of Co and Zr, with Zr used as plug inserts into the Co target, was used for sputtering and the gas-aggregation chamber was water cooled. High sputtering power in the range of 150 – 200 W was used with the Ar -flow rate of 350 SCCM. The partial pressure of the sputtering chamber and the deposition chamber are about 10^{-1} Torr and 10^{-3} Torr respectively. The nanoclusters are deposited on Si (001) substrate as films of thickness in the range of 50 – 150 nm for XRD and magnetic measurements and on copper grids as a layer (thickness 1 – 3 nm) of isolated nanoclusters for TEM studies.

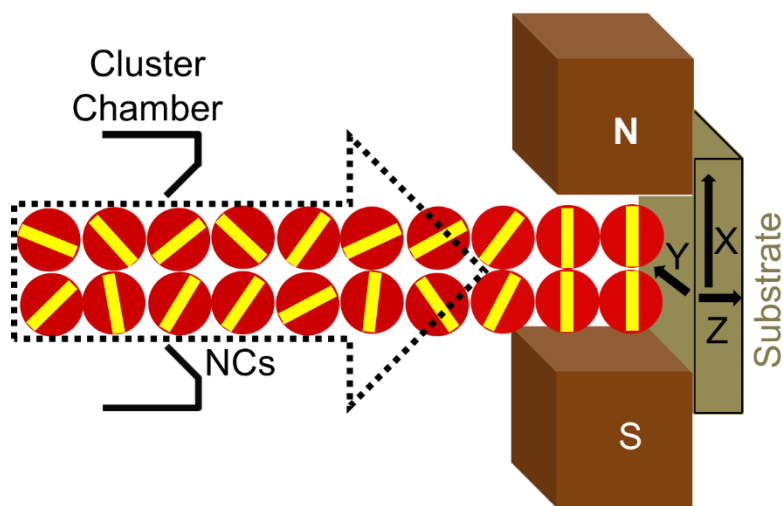


Figure 3.2.1. Magnetic alignment of nanoclusters using two permanent magnets.

The samples are coated with SiO₂ thin layer [thickness of about 25 nm for Si substrate and about 2 nm for the copper grids] to protect the nanoclusters from oxidation or other atmospheric corruptions.

The direct crystalline ordering achieved using the cluster-deposition method provides a unique method to align the nanoclusters along the easy-magnetization direction by applying an external magnetic field prior to deposition as shown in the Fig. 3.2.1.[7] Uniaxial nanoclusters of randomly oriented easy-axes pass through the uniform magnetic field of about 5 kOe generated by the permanent magnets kept close to the substrate by fixing them on the substrate holder. The magnetic field influences the crystalline easy-axes of the nanoclusters to be oriented along the direction of the magnetic field which is the x-direction in the Fig. 3.2.1 and therefore, the y and z become the hard directions for the aligned Co(Zr) nanoclusters.

3.3 Results and Discussion

XRD patterns of nanoclusters of Co and Co(Zr) having 6.3 at. % of Zr are shown in Fig. 3.3.1 (a). The standard positions and relative intensities of XRD peaks corresponding to the hexagonal close-packed (hcp) and face-centered cubic (fcc) structures of Co are given as vertical-solid and -dotted lines, respectively.[8,9]

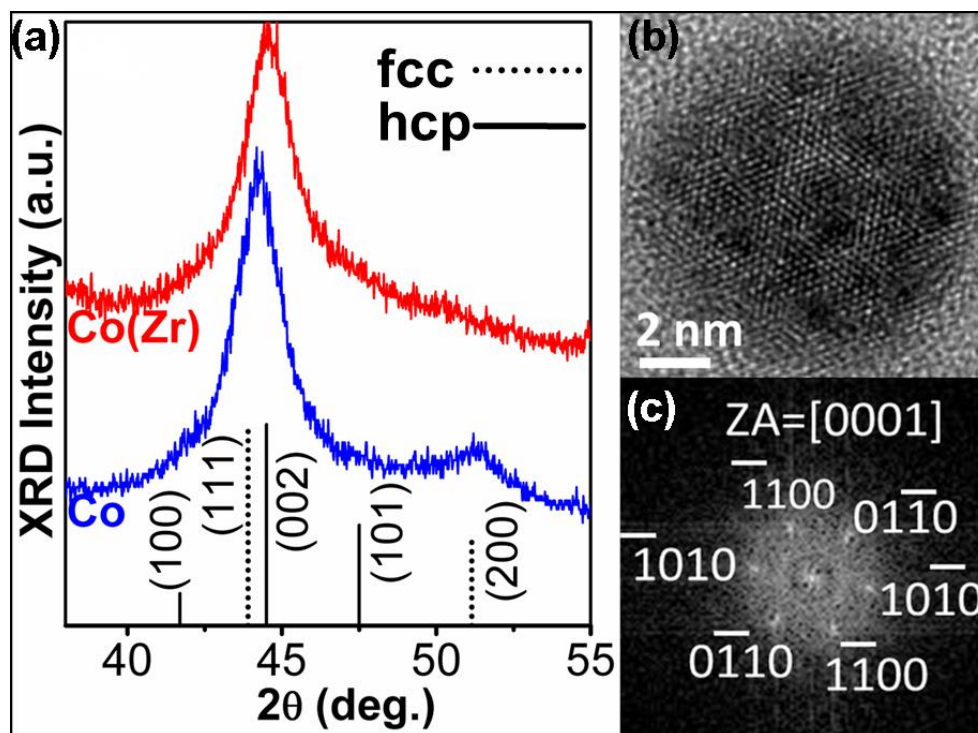


Figure 3.3.1. Structure of Co(Zr) nanoclusters. (a) XRD patterns for the nanoclusters of Co [blue line] and Co(Zr) [red line] with 6.3 at.% of Zr. (c) HRTEM image of a single Co(Zr) nanocluster and (d) the corresponding fast Fourier transform indexed for the hcp structure.

XRD pattern of Co nanoclusters show fcc structure with (111) and (200) reflection peaks. However, in the case of Co(Zr) clusters, (200) reflection of the fcc phase completely disappears and the position of the most intense XRD peak has a good agreement with that of (002) reflection of the hcp phase as shown in the XRD pattern of Co(Zr) nanoclusters having 6.3 at. % of Zr. These results reveal that Zr addition to Co nanoclusters promotes the hcp Co phase in the nanoclusters. The HRTEM image of Co(Zr) nanoclusters indicates a high degree of atomic ordering [Fig. 3.3.1 (b)], and the corresponding fast Fourier transform (FFT) image as shown in Fig. 3.3.1 (c) reveals the hcp structure in agreement with the XRD results.

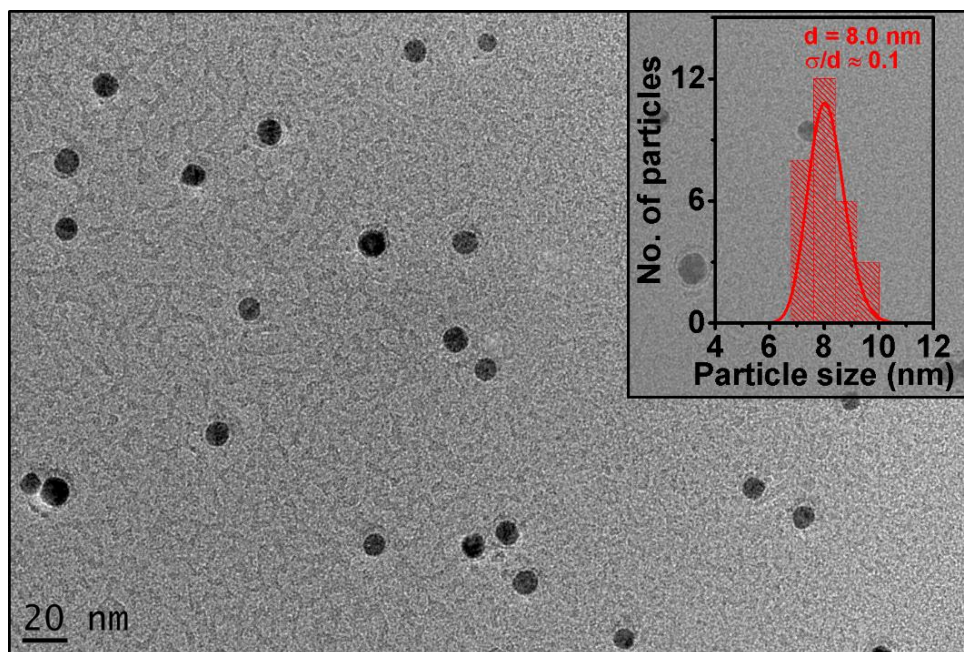


Figure 3.3.2. LRTEM image of Co(Zr) nanoclusters and the cluster size distribution (inset).

Figure 3.3.2 shows the LRTEM image which exhibits that Co(Zr) nanoclusters have an average particle size of about 8.0 nm with an rms standard deviation of $\sigma/d = 0.1$ as shown in the inset of Fig. 3.3.2.

Magnetic properties of aligned nanoclusters were investigated by measuring the magnetization M at 300 K as a function of applied magnetic field H from -70 to 70 kOe along the easy (x -axis) and hard (y - and z -axes) directions as shown in Fig. 3.3.3.

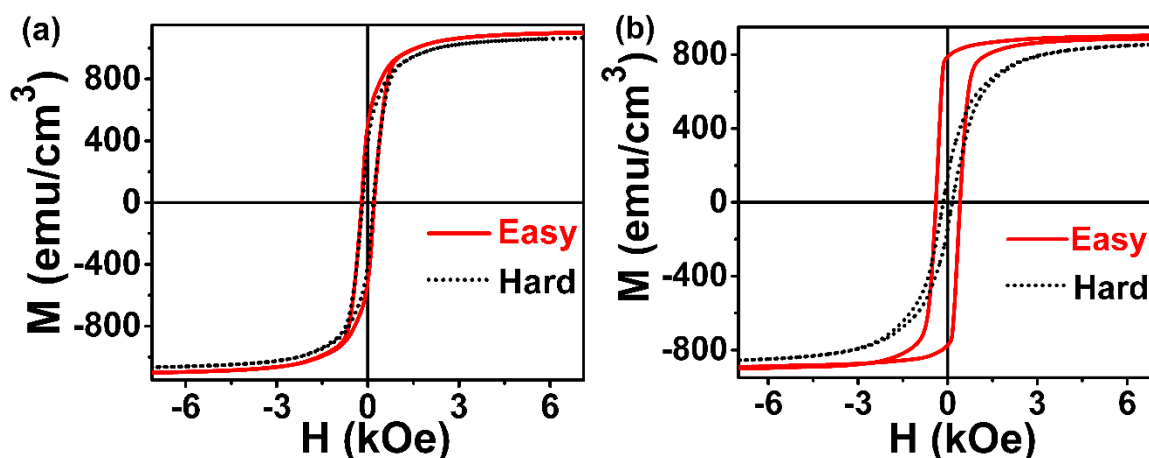


Figure 3.3.3. The expanded room-temperature M - H curves of the aligned nanoclusters measured along the easy (x -axis) and hard (y -axis) directions for (a) Co and (b) Co(Zr) nanoclusters having 6.3 at. % of Zr.

The room-temperature M - H curve of the Co nanoclusters measured along the easy (x-axis) and hard (z-axis) directions are nearly identical with coercivities $H_c \approx 180$ Oe and remanence ratios $M_r/M_s \approx 0.40$ as shown in Fig. 3.3.3 (a) revealing no alignment, due to isotropic fcc Co content. Here M_s and M_r are saturation and remanent magnetizations, respectively. In comparison, as shown in Fig. 3.3.3 (b), Co(Zr) nanoclusters having 6.3 at. % of Zr exhibit $H_c \approx 400$ Oe and $M_r/M_s \approx 0.85$ along the easy direction (x-axis) and comparatively reduced $H_c \approx 130$ Oe and $M_r/M_s \approx 0.16$ along the hard direction (z-axis). Note that M - H loop measured along the y-axis for the Co(Zr) nanoclusters is identical to that measured along the z-axis.

Figure 3.3.4 shows the measured values of H_c [Fig. 3.3.4 (a)] and M_r/M_s [Fig. 3.3.4 (b)] of Co(Zr) nanoclusters as a function of Zr at. % along the easy and hard directions. H_c and M_r/M_s are significantly higher along the easy axis as compared to those values along the hard axes for Co(Zr) nanoclusters having 6.3 and 7.8 at.% of Zr.

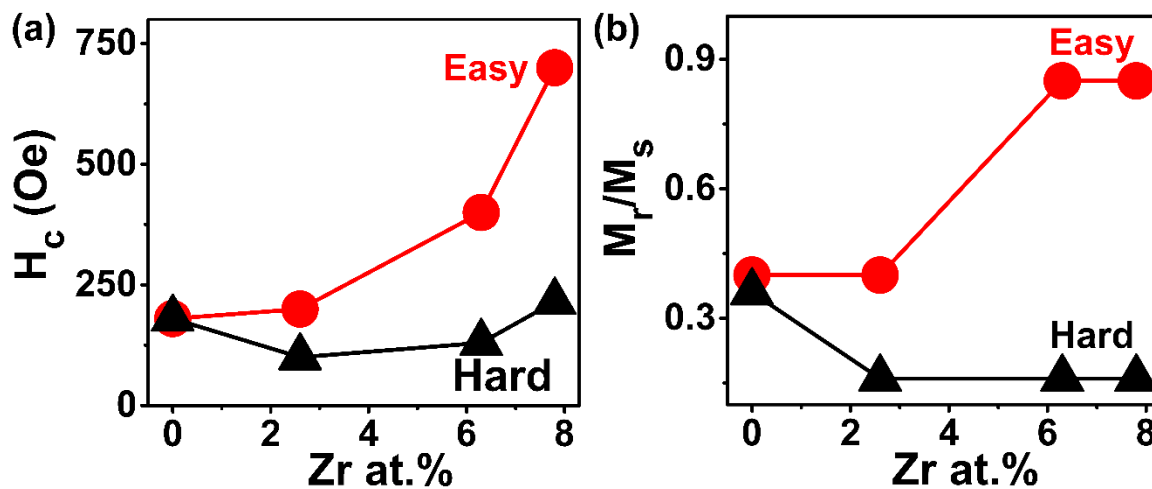


Figure 3.3.4. Variation of (a) H_c and, (b) remanence ratio (M_r/M_s) of Co(Zr) nanoclusters for different Zr -concentration along easy (red spheres) and hard (black triangles) directions.

These results reveal that Zr addition to Co improves the alignment process, presumably due to change in the crystal structure to anisotropic hcp which improves magnetic anisotropy in Co(Zr) nanoclusters. We have estimated the uniaxial magnetocrystalline anisotropy constant K_u for aligned Co(Zr) nanoclusters having 2.6, 6.3 and 7.8 at. % of Zr using the area under the complete $M-H$ curves (from 0 to 70 kOe) along the easy and hard directions.[10] In the case of Co, we have estimated the magnetic anisotropy from the high-field region of room-temperature $M-H$ curves of the unaligned Co nanoclusters by applying the law of approach to saturation method (Appendix A) used for randomly oriented magnets.[11-13]

Table 3.1. K_u and saturation magnetic polarization J_s of Co(Zr) for different Zr concentrations (x).

| x | K_u (Mergs/cm ³) | J_s (kG) |
|-----|--------------------------------|------------|
| 0 | 2.1 | 14.3 |
| 2.6 | 3.5 | 12.0 |
| 6.3 | 4.9 | 11.5 |
| 7.8 | 6.8 | 10.7 |

Table 3.1 shows K_u and magnetic polarization J_s ($J_s = 4\pi M_s$) of Co(Zr) nanoclusters as a function of Zr content and clearly indicates an increase of magnetic anisotropy in Co(Zr) nanoclusters on increasing Zr content. These nanoclusters also show appreciable J_s in the range of 0.7 to 12.0 kG. Note that generally nanoclusters show higher K_u as compared to standard bulk values, presumably due to surface effects in nanoparticles.[14]

3.4 Conclusions

In conclusion, the gas-aggregation-type cluster-deposition system was used to produce dilute Co(Zr) nanoclusters having $0 \leq \text{Zr at.}\% \leq 7.8$ and their structural and magnetic properties were investigated. XRD and HRTEM studies show that Co(Zr) nanoclusters have predominantly hcp Co phase. Co(Zr) nanoclusters also were aligned using a magnetic field of 5 kOe before deposition and the uniaxial anisotropy constant was evaluated as a

function of Zr content. These results reveal that addition of Zr to Co nanoclusters improve the easy axis alignment process, due to change in structure to anisotropic hcp phase. Co(Zr) nanoclusters having 7.8 at. % of Zr exhibit a high $K_u \approx 6.8$ Mergs/cm³ at 300 K as compared to $K_u \approx 2.1$ Mergs/cm³ for fcc Co nanoclusters.

References:

- [1] B. Wei, M. Shima, R. Pati, S. K. Nayak, D. J. Singh, R. Ma, Y. Li, Y. Bando, S. Nasu, and P. M. Ajayan, Room-temperature ferromagnetism in doped face-centered cubic Fe nanoparticles, *Small* **2**, 804 (2006).
- [2] F. Golkar, M. J. Kramer, Y. Zhang, R. W. McCallum, R. Skomski, D. J. Sellmyer, and, J. E. Shield, Structure and magnetic properties of Co-W clusters produced by inert gas condensation, *Journal of Applied Physics* **111**, 07B524 (2012).
- [3] B. Balamurugan, R. Skomski, B. Das, X. Z. Li, V. R. Shah, P. Manchanda, A. Kashyap, and D. J. Sellmyer, Magnetism of dilute Co(Hf) and Co(Pt) nanoclusters, *Journal of Applied Physics* **111**, 07B532 (2012).
- [4] R. Skomski, V. Sharma, B. Balamurugan, J. E. Shield, A. Kashyap, and D. J. Sellmyer, REPM'10 – Proceedings of the 21st Workshop on RareEarth Permanent Magnets and their Applications, pp. 55–59 (2010).
- [5] H. Yuan and D. E. Laughlin, Effects of substrate bias on magnetocrystalline anisotropy K_u of CoPt thin films with increasing Pt content, *Journal of Applied Physics* **105**, 07A712 (2009).
- [6] K. Nobuaki, K. Osamu, O. Satoshi, S. Yutaka, S. Akimasa, O. Yoshichika, and F. Kazuaki, Influence of 5d transition elements on the magnetocrystalline anisotropy of hcp-Co, *Journal of Physics: Condensed Matter* **11**, L485 (1999).
- [7] B. Balamurugan, B. Das, V. R. Shah, R. Skomski, X. Z. Li, and D. J. Sellmyer, Assembly of uniaxially aligned rare-earth-free nanomagnets, *Applied Physics Letters* **101**, 122407 (2012).
- [8] ICDD 2011 International Centre for Diffraction Data, Card No 01-089-4308.
- [9] ICDD 2011 International Centre for Diffraction Data, Card No 01-071-4238.
- [10] D. J. Sellmyer and Z. S. Shan, in *Science and Technology of Nanostructured Magnetic Materials*, edited by G. C. Hadjipanayis, and G. A. Prinz (Springer US, Boston, MA, 1991), pp. 151.
- [11] G. Hadjipanayis, D. J. Sellmyer, and B. Brandt, Rare-earth-rich metallic glasses. I. Magnetic hysteresis, *Physical Review B* **23**, 3349 (1981).
- [12] A. Franco and F. C. e Silva, High temperature magnetic properties of cobalt ferrite nanoparticles, *Applied Physics Letters* **96**, 172505 (2010).
- [13] E. Kneller, *Ferromagnetism* (Springer, Berlin, 1962).

- [14] S. Oyarzun, A. Tamion, F. Tournus, V. Dupuis, and M. Hillenkamp, Size effects in the magnetic anisotropy of embedded cobalt nanoparticles: from shape to surface, *Scientific Reports* **5**, 14749 (2015).

CHAPTER 4. Zr_2Co_{11} -BASED RARE-EARTH-FREE NANOCLUSTERS WITH HIGH ENERGY PRODUCTS

Rare-earth free magnets with appreciable permanent-magnet properties are ideal for developing magnetic materials in current geo-political situation of rare-earth criticality. Zr_2Co_{11} is one of such materials which is hard to prepare with conventional bulk processing methods, which often result in phase mixtures. Controlled non-equilibrium synthesis can stabilize the phase which potentially can show good magnetic properties. In this study, non-equilibrium synthesis of Zr-Co nanoclusters using cluster-deposition method is demonstrated and improvement of permanent magnet properties of the nanoclusters in the vicinity of Zr_2Co_{11} stoichiometry are shown.

Many of the results presented in this chapter are adapted from the publication: “Novel Nanostructured Rare-Earth-Free Magnetic Materials with High Energy Products”, B. Balamurugan[†], B. Das[†], R. Skomski, W. Y. Zhang and D. J. Sellmyer, *Advanced Materials*. 25, 6089 (2013) - [†]Co-first authorship.

I prepared and characterized the Zr-Co nanoclusters. B. Balamurugan and I analyzed the results. B. Balamurugan led the writing of the manuscript. P. Mukherjee helped with the TEM measurements, and all co-authors contributed ideas and criticized the manuscript.

4.1 Introduction

Research on new iron- or cobalt-based permanent-magnet materials has gained substantial importance, since conventional high-performance materials based on $\text{Nd}_2\text{Fe}_{14}\text{B}$ or FePt are either expensive or subject to the criticality of rare-earth elements.[1-4] However, the range of alternative compounds with appreciable magnetocrystalline anisotropy is limited, and the situation often is aggravated by their metastable nature and requirement of high-formation temperatures, above $1000\text{ }^\circ\text{C}$.[5-8] This threatens the future development and use of permanent magnets in applications ranging from home appliances to sophisticated microelectronics and environment-friendly technologies such as hybrid vehicles and wind turbines.[1-4] Hence, new Fe –or Co –rich permanent magnet alloys with high magnetocrystalline anisotropies and Curie temperatures are essential for next-generation clean energy-harvesting technologies. Furthermore, these materials must have a high coercivity H_c and a high energy product $(BH)_{\text{max}}$, that is, the maximum of the product of B and H on the BH curve in the second quadrant. $\text{Zr}_2\text{Co}_{11}$ is a suitable candidate which crystallizes in non-cubic structures, essential for obtaining superior permanent-magnet properties.[5-11] However, the poor control over phase purity in the traditionally prepared bulk alloys has an adverse effect on the permanent-magnet properties and deteriorates the energy products generally to less than 5 MGOe .[7,8,10,11]

Non-equilibrium synthesis of magnetic materials in the form of nanoclusters smaller than 10 nm can be used as an alternate approach to stabilize the non-cubic $\text{Zr}_2\text{Co}_{11}$ phase.[12,13] In addition, the reduced particle size and the associated nanoscale

effects also result in improvement of structural and magnetic properties suitable for applications in areas such as permanent magnets, magnetic recording and hybrid-energy technologies.[14-17] Moreover, alignment of easy-axes of the uniaxial Zr_2Co_{11} nanoclusters is likely to add additional advantage of obtaining high remanence ratio (M_r/M_s), which is key for high-energy products in commercial permanent magnets and enables the nanoclusters to be used as building blocks for permanent magnets and recording media.[18-20]

4.2 Synthesis of Zr_2Co_{11} Nanoclusters

Nanoclusters of Zr_2Co_{11} are synthesized using gas-aggregation type cluster-deposition method as described in Chapter 2. In brief, Co target was used in which small pellets of Zr was inserted in various numbers to control the desired composition of Zr_xCo_{100-x} nanoclusters with $9 < x < 20$. High sputtering power in the range of 150 – 200 W was used with Ar -flow lying in the range between 450 – 650 SCCM. The nanoclusters were aligned prior to deposition as described in the previous chapter (section 4.2). Zr –is known to absorb oxygen if thermally excited and hence, a thick coating of SiO_2 film (10 – 15 nm) was used for the nanoclusters deposited on Si (001) substrate. For TEM measurements, nanoclusters were deposited on copper grids with a thinner protective coating (about 1 nm). Bulk Zr_2Co_{11} was fabricated using conventional melt-spinning method as described in the section 2.2 (and ref. [8]) from which metallic ribbons were obtained and characterized for comparison with the nanoclusters.

4.3 Results

4.3.1 Structural Properties

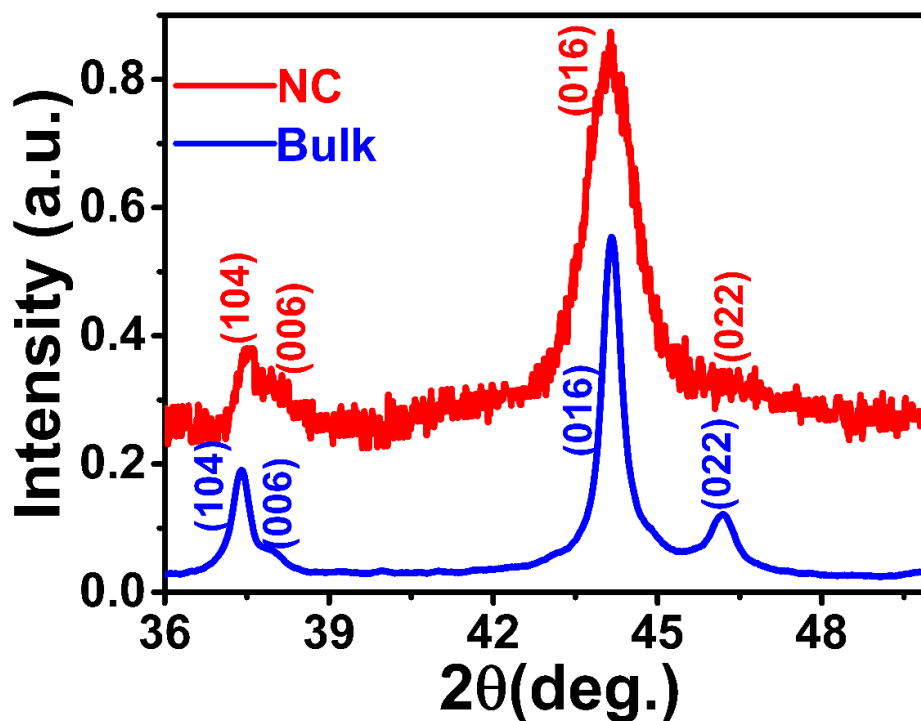


Figure 4.3.1. XRD patterns of Zr_2Co_{11} nanoclusters (red) and bulk (blue) showing rhombohedral crystal structure. (XRD of bulk Zr_2Co_{11} is adapted from ref.[8]).

XRD patterns of nanocluster films with thickness about 250 nm were obtained and compared with the diffraction patterns for bulk Zr_2Co_{11} . The red curve shown in Fig. 4.3.1 exhibits the XRD pattern for the nanoclusters which is showing rhombohedral crystal structure similar to that observed for the bulk (blue curve in Fig. 4.3.1).

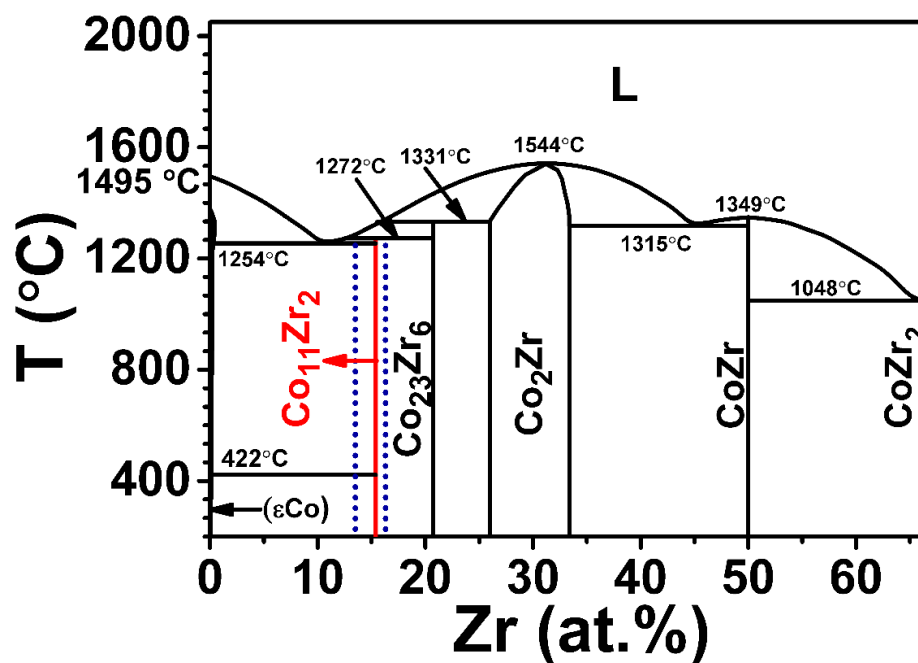


Figure 4.3.2. Equilibrium phase diagram of Co-Zr.[5] The solid red vertical line represents the ideal composition and temperatures for the formation of $\text{Zr}_2\text{Co}_{11}$ phase. The dotted blue vertical lines show the composition region where the phase observed in nanoclusters is predominantly $\text{Zr}_2\text{Co}_{11}$.

Note that, bulk $\text{Zr}_2\text{Co}_{11}$ crystallizes in both rhombohedral and orthorhombic structures at different temperatures among which, the rhombohedral $\text{Zr}_2\text{Co}_{11}$ is a high temperature phase and have comparatively high anisotropy as compare to that of the orthorhombic phase. This is not observed in the case of nanoclusters which exhibit only the high-symmetry rhombohedral structure.[7,8] The Co-Zr bulk phase diagram, shown in Fig. 4.3.2, indicates the formation of $\text{Zr}_2\text{Co}_{11}$ equilibrium phase only at a single composition and at high temperatures (solid red vertical line). However, in practice it is found that standard processing methods lead to the formation of secondary phases such as Co and $\text{Zr}_6\text{Co}_{23}$ having low magnetocrystalline anisotropies during the cooling process.[7-11] The cluster-deposited $\text{Zr}_x\text{Co}_{100-x}$ nanoclusters not only form in the high-

anisotropy rhombohedral Zr_2Co_{11} structure for $x \approx 15.4$ without high-temperature annealing, but they also exhibit a predominant Zr_2Co_{11} phase for a rather broad composition region ($13.5 \leq x \leq 16.3$), as indicated by green dotted vertical lines in Fig. 4.3.2. This phase structure is also supported by magnetic measurements.

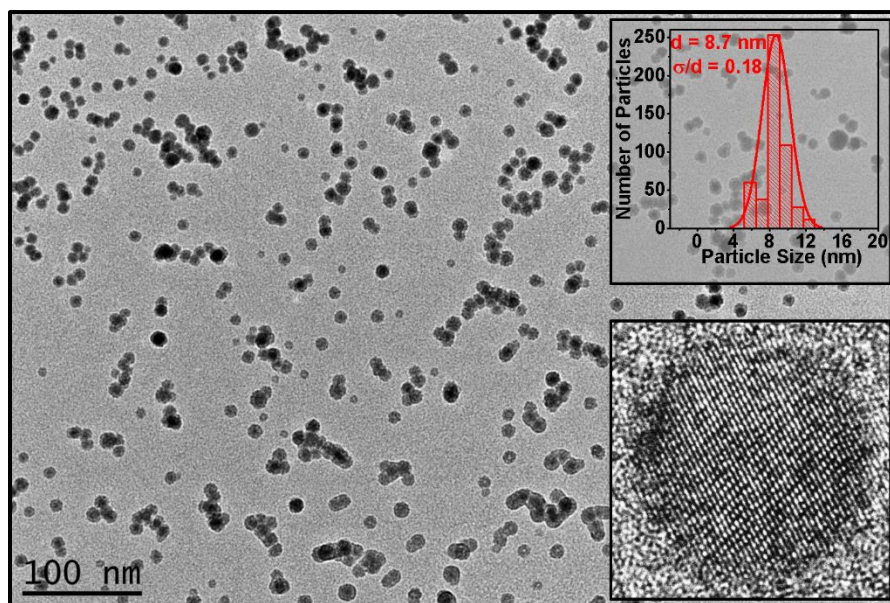


Figure 4.3.3. LRTEM image of Zr_2Co_{11} nanoclusters showing monodisperse clusters with the narrow size-distribution seen in the top inset. The bottom inset is a HRTEM image of a single Zr_2Co_{11} nanocluster showing a high degree of atomic ordering.

The Zr_xCo_{100-x} nanoclusters are monodispersed with an average cluster size $d = 8.7$ nm and an rms standard deviation of $\sigma/d = 0.18$, as shown in the transmission electron microscope (TEM) image (Fig. 4.3.3) and in the corresponding particle-size histogram of Zr_2Co_{11} nanoclusters (top inset of Fig. 4.3.3). A high-resolution TEM (HRTEM) image of

a single $\text{Zr}_2\text{Co}_{11}$ nanocluster as shown in the bottom inset of Fig. 4.3.3, reveals a high-degree of atomic ordering by showing lattice fringes.

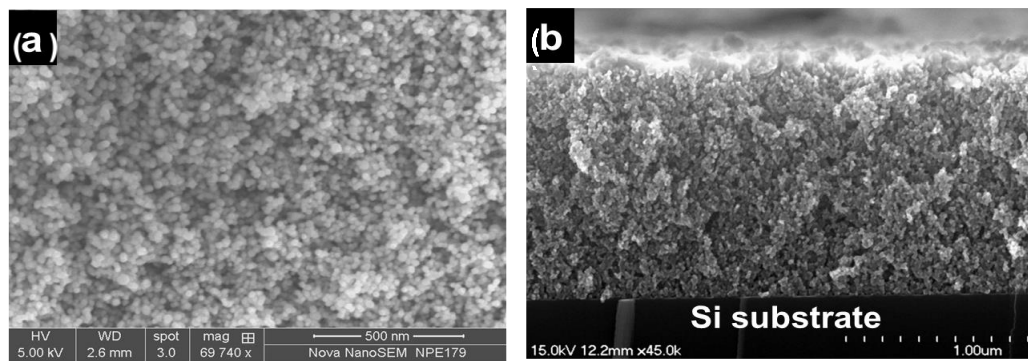


Figure 4.3.4. FESEM images of $\text{Zr}_2\text{Co}_{11}$ nanocluster films deposited on Si (001). (a), Top view. (b), Cross-sectional view. For the cross-sectional imaging, the sample was prepared by cutting the Si substrate after deposition.

Thick film of $\text{Zr}_2\text{Co}_{11}$ nanoclusters with a thickness of about $1.4 \mu\text{m}$ was deposited on Si (001) substrate for SEM [Field Emission SEM (FESEM): FEI Nova NanoSEM (section 2.4)] measurements to obtain both the planar and cross-sectional view of the film. The secondary-electron (FESEM) images of Fig. 4.3.4 shows that the nanocluster films are fairly dense, that is, they do not consist of loosely packed spheres. The volume fraction is difficult to determine from the cross-sectional view due to roughness or pores generated during the cleaving process, but the top view of the films show a density between 50 and 80%. In particular, smaller nanoclusters fill interstitial holes between bigger nanoclusters. This indicates that the nominal magnetization measured for the nanocluster-films are close to that for highly dense-packed films.

4.3.2 Magnetic Properties

The direct crystalline ordering achieved during the gas-aggregation process in the present study is essential to accomplish the major goal of aligning the easy axes of the nanoclusters. The nanoclusters are aligned by applying a magnetic field ($H_{\text{al}} \approx 5$ kOe) before deposition on the Si substrate for forming assemblies of dense-packed nanoclusters. The alignment process is similar to that described in Chapter 4. The field H_{al} is applied along the x-direction, which is parallel to the substrate, and the x-axis is expected to be the easy magnetization direction, whereas both the y- and z-directions are hard directions. The aligned nanocluster films are used for magnetization measurements along both easy and hard directions.

The room-temperature M - H hysteresis loops of aligned $\text{Zr}_x\text{Co}_{100-x}$ nanocluster assemblies exhibit a high remanence ratio M_r/M_s and coercivity H_c along the easy axis as compared to those along the hard axis. Figure 4.3.5 (a) shows the M - H loop for $\text{Zr}_2\text{Co}_{11}$ composition along easy (blue curve) and hard (red curve) directions and the expanded hysteresis loops are shown in the Fig. 4.3.5 (b). The hysteresis of the unaligned sample (green) is shown for realization of the magnetic alignment. The hysteresis loops exhibit a high $M_s = 825$ emu/cm³, and appreciable easy-axis $H_c = 4.5$ kOe ($H_c = 1.4$ kOe and 2.3 kOe along the hard direction and for unaligned $\text{Zr}_2\text{Co}_{11}$ nanoclusters, respectively).

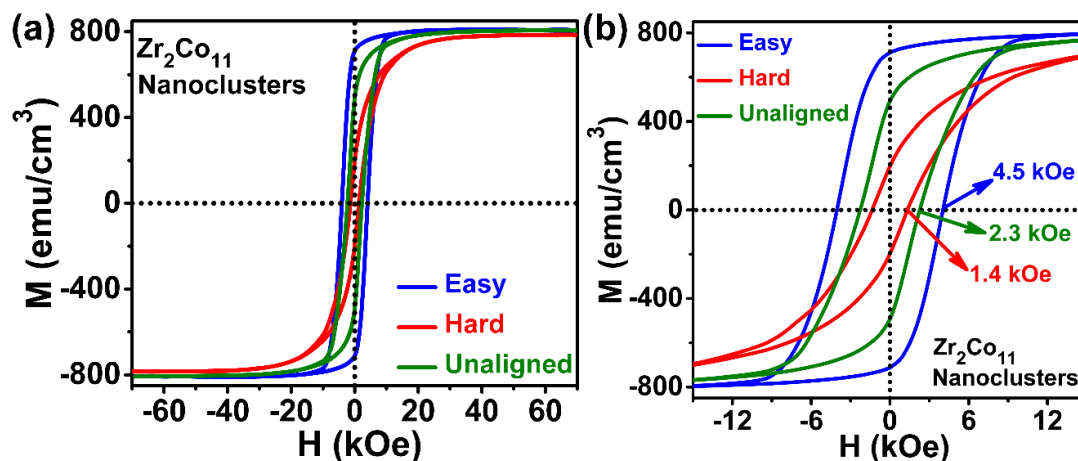


Figure 4.3.5. (a) Hysteresis loops for $\text{Zr}_2\text{Co}_{11}$ nanoclusters along easy (x)[blue] and hard (y) [red] direction compared with that for the unaligned sample [green]. (b) The expanded version of the hysteresis loops shown in (a) for clarification.

The alignment of the nanoclusters helps to improve the coercivity substantially compared to that of the unaligned samples as seen in the Fig. 4.3.5. Moreover, the remanence ratio (M_r/M_s) along easy and hard directions as well as for the unaligned sample exhibit large difference with a highest along easy axis and the lowest along the hard axis and the value for the unaligned sample lying in between them. This, ensures the high degree of magnetic alignment for the nanoclusters and a qualitative measure for the alignment is discussed later (section 4.3.3) in this chapter.

Figure 4.3.6 shows H_c and the saturation magnetic polarization (J_s) for the $\text{Zr}_x\text{Co}_{100-x}$ nanoclusters, measured along the easy axis and as a function of x . The figure yields $H_c = 2.9 - 4.5$ kOe and $J_s = 8.6 - 10.3$ kG for nanocluster films that are predominantly $\text{Zr}_2\text{Co}_{11}$.

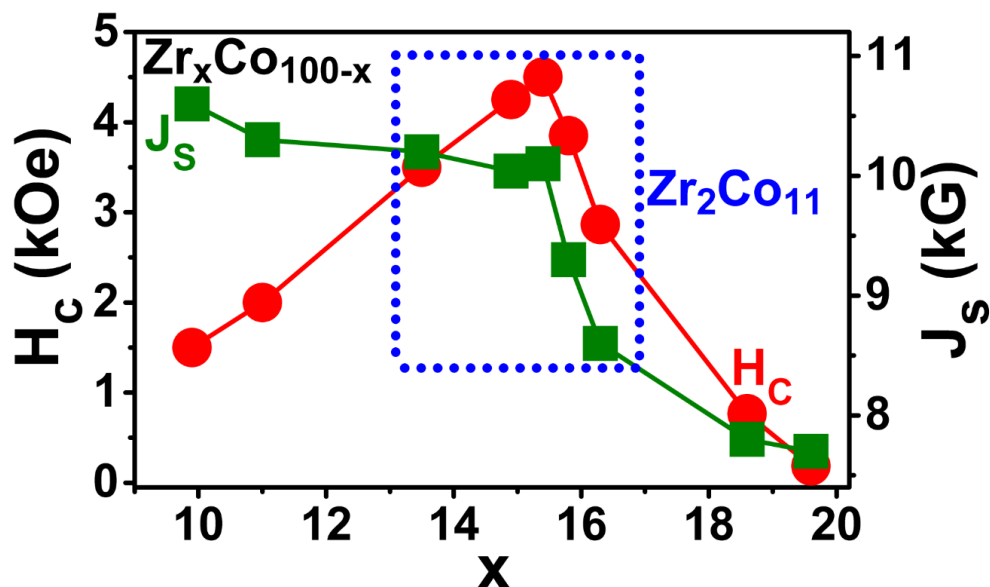


Figure 4.3.6. Coercivity H_c (red curve) and saturation polarization J_s (green curve) measured along the easy axis at 300 K for aligned Zr_xCo_{100-x} nanoclusters. The blue-dotted rectangle shows the composition range where the phase is predominantly Zr_2Co_{11} .

These values are comparable to those of $SmCo_5$ and $L1_0$ -ordered FePt and CoPt nanoclusters smaller than 10 nm.[16,21,22] The FESEM image (Fig. 4.3.4) reveals that the Zr_2Co_{11} nanoclusters stick to each other in the film but nevertheless exhibit an appreciable room-temperature coercivity of about 4.5 kOe. This indicates that interparticle interactions and even physical contact do not destroy the coercivity. The law-of-approach-to-saturation method (Appendix A) was used to estimate the magnetocrystalline anisotropy constant (K_1) of the Zr_2Co_{11} nanoclusters using the high-field region of the hysteresis loop for unaligned nanoclusters [23-25], which yields $K_1 = 11$ Mergs/cm³, close to the reported $K_1 = 13.5$ Mergs/cm³ for the bulk material.[26,27]

4.3.3 Degree of Magnetic Alignment

Magnetic alignment of Zr_2Co_{11} nanoclusters yields a high $M_r/M_s = 0.88$ along the easy axis, as compared to the low value $M_r/M_s \approx 0.5$ generally observed for randomly oriented permanent-magnet nanoclusters.[28,29]

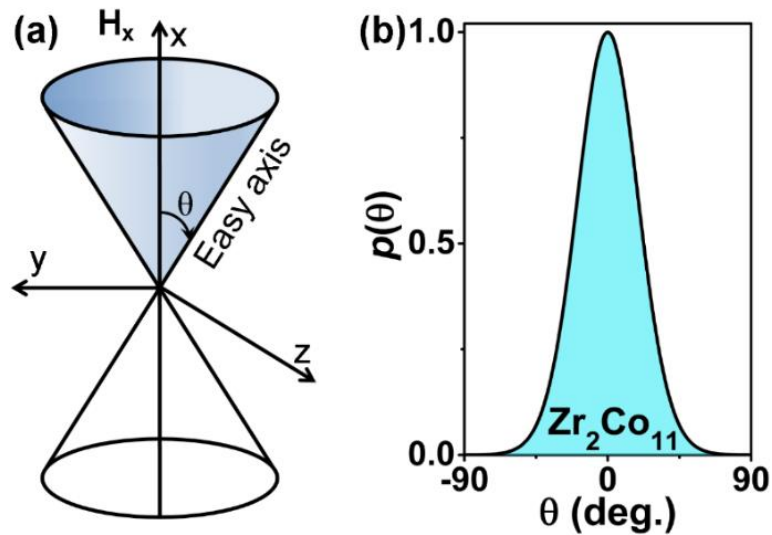


Figure 4.3.7. Degree of magnetic alignment. (a) Geometry of the easy-axis configuration, where H_x is the magnetic field applied along the x direction (direction of H_{al}) and θ is the angle between the easy axis and H_x . (b) The normalized easy-axis probability distribution or texture function $p(\theta)$ for aligned Zr_2Co_{11} nanocluster assembly.

M_r/M_s measured along the easy axis is used to quantify the magnetic alignment.

Figure 4.3.7 (a) shows the geometry of the easy-axis configuration and for a non-interacting ensemble of aligned uniaxial nanoclusters, the normalized average remanence can be written as[30-34]

$$m_n = \frac{M_r}{M_s} = \frac{\int m(\theta)P(\theta)\sin\theta d\theta}{\int P(\theta)\sin\theta d\theta} \quad 4.1$$

where θ is the angle between the easy-axis and x-direction, and m is the normalized magnetic moment of the individual nanoclusters in the field (or x-axis) direction. The easy-axis distribution or texture function $P(\theta)$ can be approximated by [34]

$$P(\theta) = P(0)\exp\left(\frac{\cos\theta}{\delta}\right) \quad 4.2$$

In this equation, δ parameterizes the width of distribution of the easy-axis ($\delta \ll 1$ for well-aligned particle ensembles).[30,32] Combination of Eqns. 4.1 and 4.2 yields M_r/M_s , which depends on δ . The remanence ratio of Zr_2Co_{11} nanoclusters, $M_r/M_s = 0.88$, corresponds to a δ value of about 0.11 and to the narrow normalized distribution ($p(\theta) = P(\theta)/P(0)$) as shown in Fig. 4.3.7 (b). Numerical evaluation of Eq. 4.1 shows that the percentage of nanoclusters with alignment angles smaller than 30° is about 73 %.

4.4 Discussion

The stabilization of a single phase Zr_2Co_{11} nanoclusters having high-anisotropy rhombohedral structure, without a subsequent high-temperature annealing, is an important achievement of the study and is essential for alignment of the easy axes prior to deposition. Note that unaligned Zr_2Co_{11} nanoclusters are isotropic with $M_r/M_s \approx 0.50$ along the in-plane direction, and M_r/M_s increases to 0.88 upon alignment with a field of about 5 kOe. By successfully obtaining a single Zr_2Co_{11} phase and magnetic alignment, a nominal high energy product $(BH)_{\max}$ in the Zr_2Co_{11} nanocluster films is achieved, which is a key figure of merit for permanent-magnet materials. Figure 4.4.1 (a) shows the room-

temperature B and energy product BH_i for an assembly of easy axis aligned Zr_2Co_{11} nanoclusters as function of H_i , where $H_i = H - NM_s$ is the internal field.

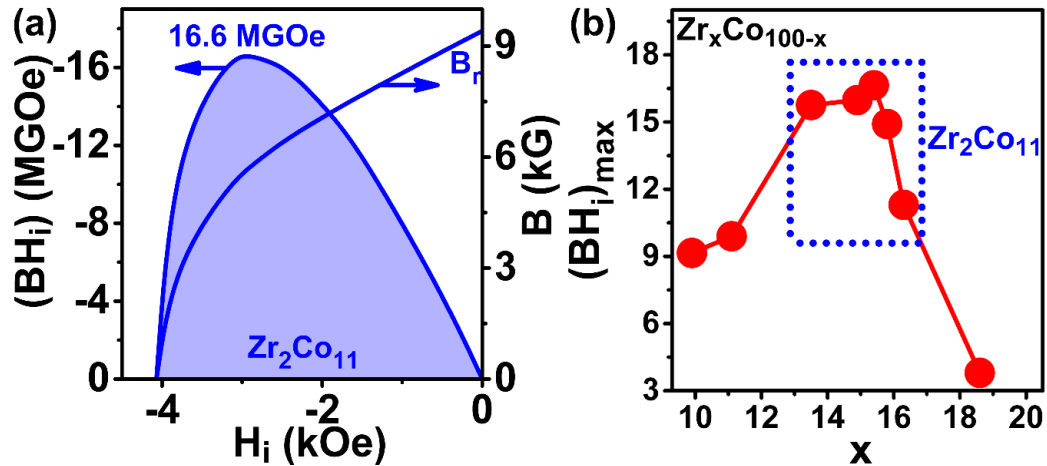


Figure 4.4.1. Energy products. (a) B and BH_i curves for Zr_2Co_{11} nanoclusters. (b) $(BH_i)_{max}$ for Zr_xCo_{100-x} with different Zr concentrations (x) showing reasonably high energy products for majority Zr_2Co_{11} phase (blue rectangle).

N is the demagnetization factor and estimated to be 0.26 by comparing the slopes (micromagnetic susceptibilities) of in-plane and perpendicular $M(H)$ curves of isotropic samples (Details in Appendix B). Figure 4.4.1 (a) yields an energy product of about 16.6 MGOe which is high compared to that of alnico and other rare-earth-free magnetic materials.[1,2,35-38] The variation of energy products with different Zr concentrations in Zr_xCo_{100-x} is shown in the Fig. 4.4.1 (b) which shows reasonably high $(BH_i)_{max}$ values (> 10 MGOe) for the composition range exhibiting Zr_2Co_{11} . The formation of new nanoclusters, direct-crystalline ordering, and high degree of easy-axis alignment reported in this study are essential processing steps for developing nanostructured rare-earth-free high-performance permanent magnets.

References:

- [1] N. Jones, Materials science: the pull of stronger magnets, *Nature* **472**, 22 (2011).
- [2] J. M. D. Coey, Permanent magnets: Plugging the gap, *Scripta Materialia* **67**, 524 (2012).
- [3] M. Jacoby, Powerful Pull to New Magnets, *Chemical & Engineering News* **91**, 23 (2013).
- [4] M. J. Kramer, R. W. McCallum, I. A. Anderson, and S. Constantinides, Prospects for Non-Rare Earth Permanent Magnets for Traction Motors and Generators, *JOM* **64**, 752 (2012).
- [5] H. Okamoto, *Desk handbook: phase diagrams for binary alloys* (ASM International, Materials Park, OH, 2000), Phase diagrams for binary alloys, pp. 248, and, 263.
- [6] K. H. J. Buschow, Differences in Magnetic-Properties between Amorphous and Crystalline Alloys, *Journal of Applied Physics* **53**, 7713 (1982).
- [7] G. V. Ivanova, N. N. Shchegoleva, and A. M. Gabay, Crystal structure of Zr_2Co_{11} hard magnetic compound, *Journal of Alloys and Compounds* **432**, 135 (2007).
- [8] W. Y. Zhang, X. Z. Li, S. Valloppilly, R. Skomski, J. E. Shield, and D. J. Sellmyer, Magnetism of rapidly quenched rhombohedral Zr_2Co_{11} -based nanocomposites, *Journal of Physics D-Applied Physics* **46** (2013).
- [9] B. G. Demczyk and S. F. Cheng, Structures of Zr_2Co_{11} and $HfCo_7$ Intermetallic Compounds, *Journal of Applied Crystallography* **24**, 1023 (1991).
- [10] T. Saito, High performance Co-Zr-B melt-spun ribbons, *Applied Physics Letters* **82**, 2305 (2003).
- [11] Z. P. Hou, W. Q. Wang, S. F. Xu, J. B. Zhang, C. J. Wu, and F. Su, Hard magnetic properties of melt-spun $Co_{82}Zr_{18-x}Ti_x$ alloys, *Physica B-Condensed Matter* **407**, 1047 (2012).
- [12] B. Balamurugan, B. Das, V. R. Shah, R. Skomski, X. Z. Li, and D. J. Sellmyer, Assembly of uniaxially aligned rare-earth-free nanomagnets, *Applied Physics Letters* **101** (2012).
- [13] B. Balasubramanian, R. Skomski, X. Li, S. R. Valloppilly, J. E. Shield, G. C. Hadjipanayis, and D. J. Sellmyer, Cluster synthesis and direct ordering of rare-earth transition-metal nanomagnets, *Nano Letters* **11**, 1747 (2011).

- [14] D. J. Sellmyer, Applied physics - Strong magnets by self-assembly, *Nature* **420**, 374 (2002).
- [15] D. Alloyeau, C. Ricolleau, C. Mottet, T. Oikawa, C. Langlois, Y. Le Bouar, N. Braidy, and A. Loiseau, Size and shape effects on the order-disorder phase transition in CoPt nanoparticles, *Nature Materials* **8**, 940 (2009).
- [16] S. H. Sun, C. B. Murray, D. Weller, L. Folks, and A. Moser, Monodisperse FePt nanoparticles and ferromagnetic FePt nanocrystal superlattices, *Science* **287**, 1989 (2000).
- [17] H. Zeng, J. Li, J. P. Liu, Z. L. Wang, and S. H. Sun, Exchange-coupled nanocomposite magnets by nanoparticle self-assembly, *Nature* **420**, 395 (2002).
- [18] B. Balamurugan, D. J. Sellmyer, G. C. Hadjipanayis, and R. Skomski, Prospects for nanoparticle-based permanent magnets, *Scripta Materialia* **67**, 542 (2012).
- [19] S. Kang, S. Shi, Z. Jia, G. B. Thompson, D. E. Nikles, and J. W. Harrell, Microstructures and magnetic alignment of L1₀ FePt nanoparticles, *Journal of Applied Physics* **101** (2007).
- [20] S. Kang, Z. Jia, S. Shi, D. E. Nikles, and J. W. Harrell, Easy axis alignment of chemically partially ordered FePt nanoparticles, *Applied Physics Letters* **86** (2005).
- [21] C. H. Chen, S. J. Knutson, Y. Shen, R. A. Wheeler, J. C. Horwath, and P. N. Barnes, The effect of particle size on coercivity and crystallinity of SmCo₅, *Applied Physics Letters* **99** (2011).
- [22] T. Matsushita, T. Iwamoto, M. Inokuchi, and N. Toshima, Novel ferromagnetic materials of SmCo₅ nanoparticles in single-nanometer size: chemical syntheses and characterizations, *Nanotechnology* **21** (2010).
- [23] G. Hadjipanayis, D. J. Sellmyer, and B. Brandt, Rare-earth-rich metallic glasses. I. Magnetic hysteresis, *Physical Review B* **23**, 3349 (1981).
- [24] E. Kneller, *Ferromagnetism* (Springer, Berlin, 1962).
- [25] A. Franco and F. C. E Silva, High temperature magnetic properties of cobalt ferrite nanoparticles, *Applied Physics Letters* **96**, 172505 (2010).
- [26] B. Balamurugan, B. Das, W. Y. Zhang, R. Skomski, and D. J. Sellmyer, Hf-Co and Zr-Co alloys for rare-earth-free permanent magnets, *Journal of Physics-Condensed Matter* **26** (2014).
- [27] T. Ishikawa and K. Ohmori, Hard magnetic phase in rapidly quenched Zr-Co-B alloys, *IEEE Transactions on Magnetics* **26**, 1370 (1990).

- [28] E. P. Wohlfarth, Relations between Different Modes of Acquisition of the Remanent Magnetization of Ferromagnetic Particles, *Journal of Applied Physics* **29**, 595 (1958).
- [29] C. Tannous and J. Gieraltowski, The Stoner-Wohlfarth model of ferromagnetism, *European Journal of Physics* **29**, 475 (2008).
- [30] D. Le Roy, R. Morel, A. Brenac, and L. Notin, Anisotropy easy axes alignment of deposited Co nanoclusters, *Journal of Magnetism and Magnetic Materials* **323**, 127 (2011).
- [31] L. Neel, R. Pauthenet, G. Rimet, and V. S. Giron, On the Laws of Magnetization of Ferromagnetic Single Crystals and Polycrystals - Application to Uniaxial Compounds, *Journal of Applied Physics* **31**, S27 (1960).
- [32] H. Rubio and S. Suarez, Easy axis distribution in interacting fine-particle systems: Two and three dimensions, *Journal of Applied Physics* **87**, 7415 (2000).
- [33] K. H. Muller, D. Eckert, P. A. P. Wendhausen, A. Handstein, S. Wirth, and M. Wolf, Description of Texture for Permanent-Magnets, *IEEE Transactions on Magnetics* **30**, 586 (1994).
- [34] D. Givord, A. Lienard, R. P. Delabathie, P. Tenaud, and T. Viadieu, Determination of the Degree of Crystallites Orientation in Permanent-Magnets by X-Ray-Scattering and Magnetic Measurements, *Journal De Physique* **46**, 313 (1985).
- [35] J. B. Yang, K. Kamaraju, W. B. Yelon, W. J. James, Q. Cai, and A. Bollero, Magnetic properties of the MnBi intermetallic compound, *Applied Physics Letters* **79**, 1846 (2001).
- [36] M. A. McGuire, O. Rios, N. J. Ghimire, and M. Koehler, Hard ferromagnetism in melt-spun Hf₂Co₁₁B alloys, *Applied Physics Letters* **101** (2012).
- [37] B. Balke, G. H. Fecher, J. Winterlik, and C. Felser, Mn₃Ga, a compensated ferrimagnet with high Curie temperature and low magnetic moment for spin torque transfer applications, *Applied Physics Letters* **90** (2007).
- [38] J. H. Park, Y. K. Hong, S. Bae, J. J. Lee, J. Jalli, G. S. Abo, N. Neveu, S. G. Kim, C. J. Choi, and J. G. Lee, Saturation magnetization and crystalline anisotropy calculations for MnAl permanent magnet, *Journal of Applied Physics* **107** (2010).

CHAPTER 5. MAGNETIC PROPERTIES OF $Zr_2Co_{11}:Fe-Co$ NANOCOMPOSITES FABRICATED BY NANOCLUSTER-DEPOSITION

Magnetic nanocomposites with a combination of hard and soft magnets are superior in energy products since they can utilize high coercivity of the hard phase and high magnetization of the soft phase together. Exchange-coupling between hard and soft phases is necessary for ideal composite magnets which requires controlled synthesis method. In this study, fabrication of magnetic nanocomposites with Zr_2Co_{11} nanoclusters as hard phase and Fe-Co matrix as soft phase is demonstrated and magnetic properties of the nanocomposite films for different hard-soft volume ratio are shown. Enhanced energy-product of the nanocomposites compared to bare Zr_2Co_{11} nanoclusters indicates the positive results of the exchange-coupled composite magnets.

Results presented in this chapter are related to the publications: “Hf–Co and Zr–Co alloys for rare-earth-free permanent magnets”, B. Balamurugan, B. Das, W. Y. Zhang, R. Skomski and D. J. Sellmyer, *Journal of Physics: Condensed Matter*. 26, 064204 (2014) and “Magnetic nanostructuring and overcoming Brown's paradox to realize extraordinary high-temperature energy products”, B. Balamurugan, P. Mukherjee, R. Skomski, P. Manchanda, B. Das and D. J. Sellmyer, *Scientific Reports*. 4, 6265 (2014).

I fabricated and characterized of the $Zr_2Co_{11}:Fe-Co$ nanocomposite films. R. Skomski did the theoretical modeling of the nanocomposites and P. Mukherjee helped with TEM measurements. All co-authors criticized the manuscripts.

5.1 Introduction

Exchange-coupled hard-soft nanocomposites are an active research area in permanent-magnet development.[1-8] In particular, this class of nanostructures has gained an immense focus in recent years to develop new high-energy magnetic materials to satisfy the widespread use of permanent magnets in energy-related applications.[9,10] Besides their technological impact, the nanoscale magnetic properties and associated physical phenomena are also of considerable interest from the viewpoint of fundamental science. The soft-phase material improves the hard-magnetic performance of the main hard phase, using excess anisotropy to enhance magnetization and energy product beyond that of the hard phase. This is evidenced by theory and/or various proof-of-principle experiments in nanocomposite systems such as multilayered thin films, nanocrystalline ribbons, bulk materials with a random distribution of soft and hard phases, and self-assembled nanoclusters.[4-8] The well-known challenge is, however, to maintain significant coercivity in the presence of the soft phase. It is well-established that the soft phase of a two-phase system cannot be much larger than twice the Bloch-wall width $\delta_h = \pi\sqrt{A/K_h}$ of the hard phase irrespective of dimensionality, where A and K_h are the exchange-stiffness constant and magnetic anisotropy constant of the hard phase, respectively.[1,2,11]

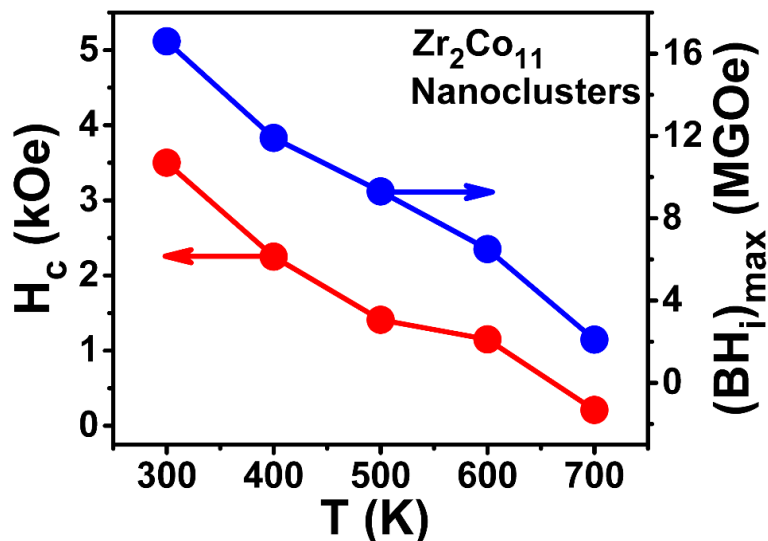


Figure 5.1.1. Coercivity [H_c ; red curve] and energy product [$(BH)_i$]_{max}; blue curve] of Zr_2Co_{11} nanoclusters measured at different temperatures.

Thus, the nanostructuring requires a uniform mixture of hard and soft grains of sizes preferably about 10 nm, easy-axis alignment of hard grains for obtaining a high remanent magnetization M_r nearly equal to the saturation magnetization M_s , and a homogeneous distribution of hard and soft phases for ensuring effective exchange-coupling.[1,2]

However, optimum exchange-coupling and superior permanent-magnet properties of nanocomposite magnets depend significantly on the permanent-magnet properties of the hard phase so that it can be suitable for practical applications both at room and high temperatures. In chapter 5, it is shown that Zr_2Co_{11} could be a suitable hard-magnetic candidate with high energy products which is free of critical rare-earth elements or expensive noble metals. Moreover, as shown in Fig. 5.1.1, the nanoclusters exhibit significant coercivities [H_c] and energy-products [$(BH)_i$]_{max} at high-temperatures (up to

600 K) suitable for most permanent-magnet applications ranging from room temperature to high temperatures.[12-14]

5.2 Synthesis of the Nanocomposite Cluster Films

Exchange-coupled nanocomposites of $Zr_2Co_{11}:Fe-Co$ are synthesized using the cluster-deposition system described in chapter 2 with a DC magnetron gun used for sputtering Fe-Co matrix. Figure 5.2.1 (a) shows a schematic of the fabrication process along with magnetic alignment of the nanocomposite cluster-films and Fig. 5.2.1 (b) shows schematic-example of such films obtained after alignment.

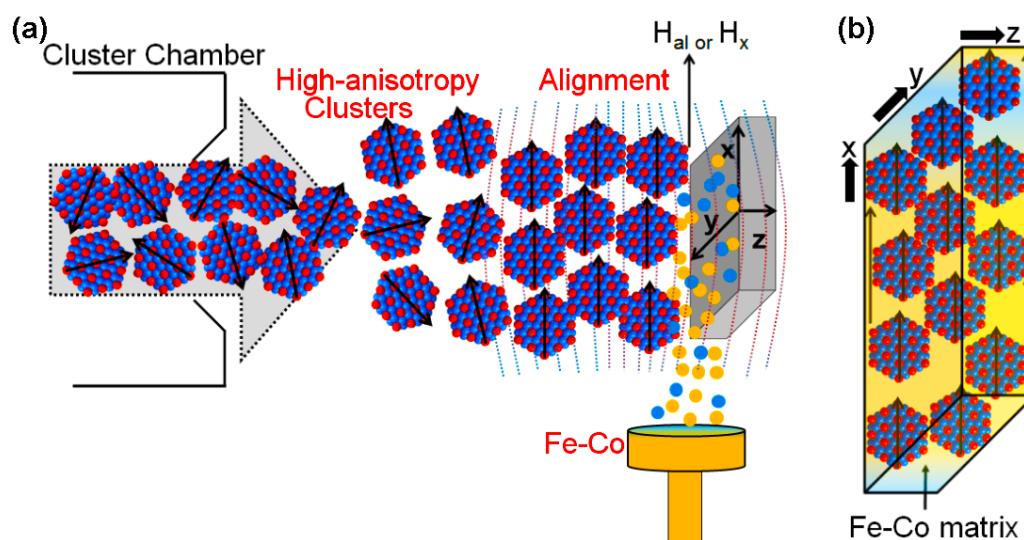


Figure 5.2.1. (a) Schematic of the nanocomposite fabrication process showing the alignment of high-anisotropy nanoclusters and co-deposition of Fe and Co atoms using the DC magnetron sputtering. H_{al} (or H_x) indicates the direction of the alignment field. (b) Sample structure of an aligned nanocomposite film. The substrate is excluded for clarity and the co-ordinate axes clarifies the alignment direction (x). [Image idea and concept from Dr. B. Balamurugan at NCMN]

The target for the soft Fe-Co matrix is optimized to a composition close to Fe₆₅Co₃₅ which is reported to have a large saturation magnetic polarization (J_s) of about 24.5 kG, required to obtain high magnetization in an exchange-coupled magnet.[15]

Fabrication of hard-magnetic Zr₂Co₁₁ nanoclusters is similar to that described in the previous chapter, only with a minor variation in the deposition process involving co-deposition of the Fe-Co soft matrix at various volume fractions with respect to the nanoclusters. The nominal thickness of the nanocomposite films was determined from the deposition rate measured using a quartz-crystal thickness monitor which also provides a quantitative measure of the volume fractions of the soft and hard phases in the film. Hence, to change the fraction, deposition rates of the nanoclusters and the Fe-Co film were adjusted according to the desired values. Nanocomposite films deposited on Si (001) substrate were used for magnetic characterization. For TEM measurements the nanocomposites are deposited on copper grids with low coverage densities but large enough to determine an approximate average distance between the Zr₂Co₁₁ nanoclusters required to realize the interaction between the hard-nanoclusters and its effect on the overall magnetic properties on the nanocomposites. A thin film of SiO₂ was used as protective coating on the nanocomposites, similar to that described in chapter 5, to prevent oxidation.

5.3 Results and Discussion

5.3.1 Nanostructures of Zr_2Co_{11} :Fe-Co composite films

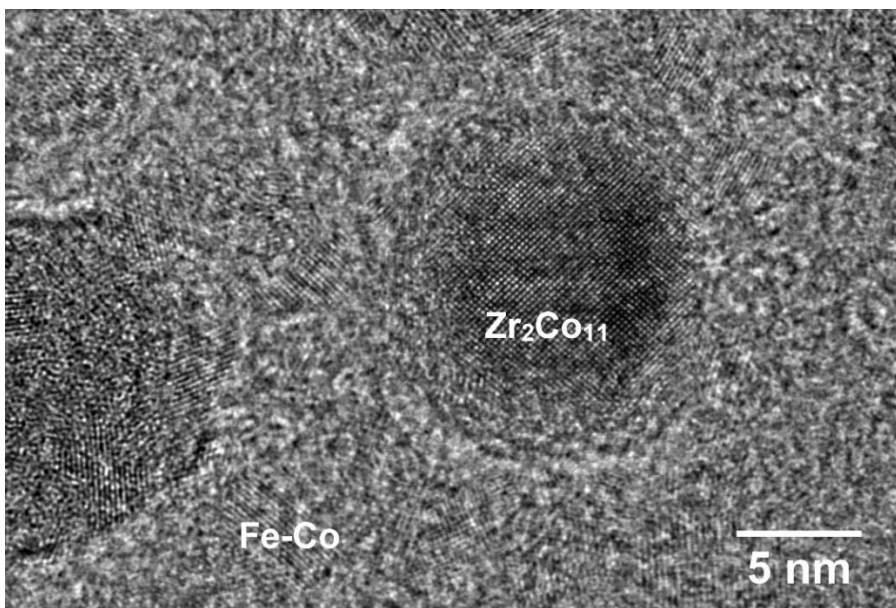


Figure 5.3.1. HRTEM image of Zr_2Co_{11} : Fe-Co nanocomposite film with 15 vol. % of Fe-Co.

Hard nanoclusters of Zr_2Co_{11} are embedded in soft magnetic Fe-Co films as shown in the HRTEM image (Fig. 5.3.1) where the nanoclusters are seen to be separated by the Fe-Co matrix for 15 vol. % of the soft Fe-Co. The Zr_2Co_{11} nanoclusters are highly crystalline as seen in Fig. 5.3.1 with the average cluster-size less than 10 nm (average size of Zr_2Co_{11} nanoclusters is about 8.7 nm as described in section 4.3.1) which are important to obtain superior hard-magnetic nanoclusters required for optimization of the magnetic properties. The composition of the Zr_2Co_{11} nanoclusters are verified using EDX and the corresponding elemental color maps are shown in Fig. 5.3.2.

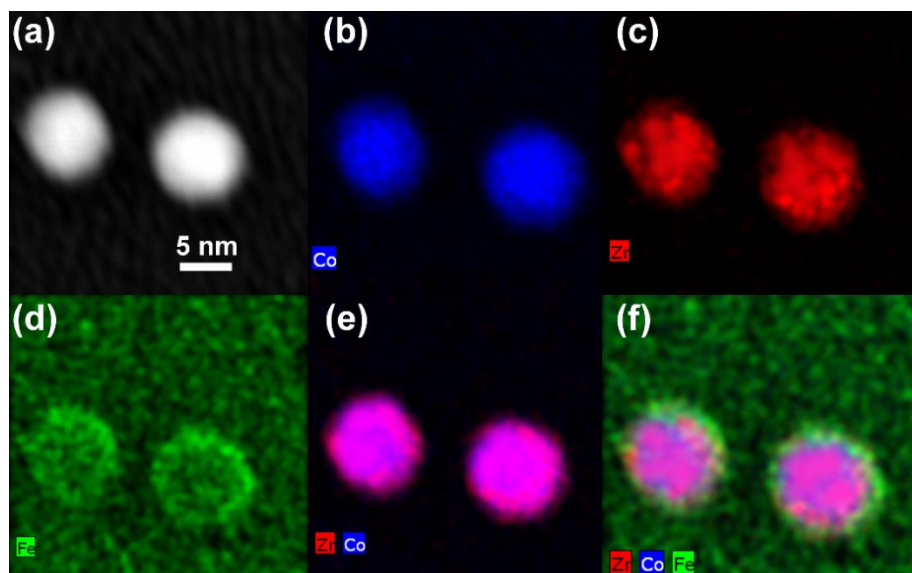


Figure 5.3.2. STEM and EDX of $Zr_2Co_{11}:Fe-Co$ nanocomposite film with 15 vol. % of Fe-Co. HAADF image (a); color maps for only Co, (b), only Zr, (c), only Fe, (d), Co and Zr, (e), and Co, Zr and Fe, (f).

HAADF image [Fig. 5.3.2 (a)] of the nanocomposite film with 15 vol. % of Fe-Co shows no significant contrast difference indicating homogeneous distribution of Co and Zr across the volume of the nanoclusters which is also shown in the EDX color maps of Co, Zr and combined Co and Zr [Figures 5.3.2 (b), (c) and (e) respectively]. Figure 5.3.2 (d) and (f) show color maps of the nanocomposite film with only Fe and all the elements (Co, Zr and Fe) respectively elucidating the soft-magnetic matrix in which the hard nanoclusters are ingrained, which improves the packing fraction of magnetic materials in the films and is essential to obtain exchange-coupling between the soft and hard phases.

5.3.2 Magnetic Properties

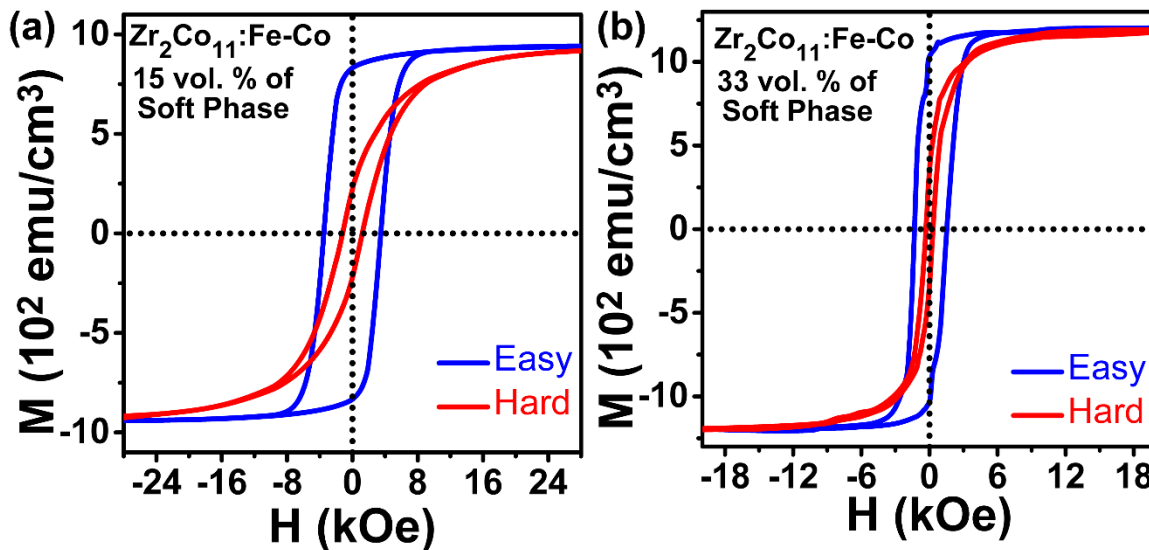


Figure 5.3.3. Magnetic hysteresis loops at room temperature along easy (blue curve) and hard (red curve) directions of $\text{Zr}_2\text{Co}_{11}:\text{Fe-Co}$ nanocomposite films with, (a) 15 vol. % and, (b) 33 vol. % of soft phase.

Magnetically aligned $\text{Zr}_2\text{Co}_{11}:\text{Fe-Co}$ nanocomposites exhibit a high degree of alignment as seen from the difference in the room temperature hysteresis loops along easy and hard directions for films with 15 and 33 vol. % of soft phase shown in Fig. 5.3.3 (a) and (b) respectively. Also, the hysteresis loops indicate a strong exchange-coupling between the soft and hard phases for 15 vol. % of Fe-Co, whereas the exchange-coupling is substantially good even for 33 vol. % of the soft phase. Usually, for a strongly exchange-coupled magnetic nanocomposite, the hysteresis loop does not exhibit two-phase behavior as seen in the case of nanocomposites with 15 vol. % of Fe-Co [Fig. 5.3.3 (a)], while for 33 vol. % of Fe-Co, the small kink in the hysteresis loop exhibits two-phase hysteresis behavior [Fig. 5.3.3 (b)] indicating slightly weaker exchange-

coupling.[16] For the nanocomposite film with 15 vol. % of Fe-Co, H_c is about 3.5 kOe which is substantial and is not significantly lower than that for Zr_2Co_{11} nanoclusters ($H_c = 4.5$ kOe) which is essential for magnetic applications. For a larger amount of the soft phase, H_c decreases with expected increase in the magnetization (M_s) or saturation magnetic polarization (J_s) as can be seen in the Fig. 5.3.3 (b) for 33 vol. % of Fe-Co showing an H_c of about 1.5 kOe.

5.3.3 Nanocomposite Model Structure

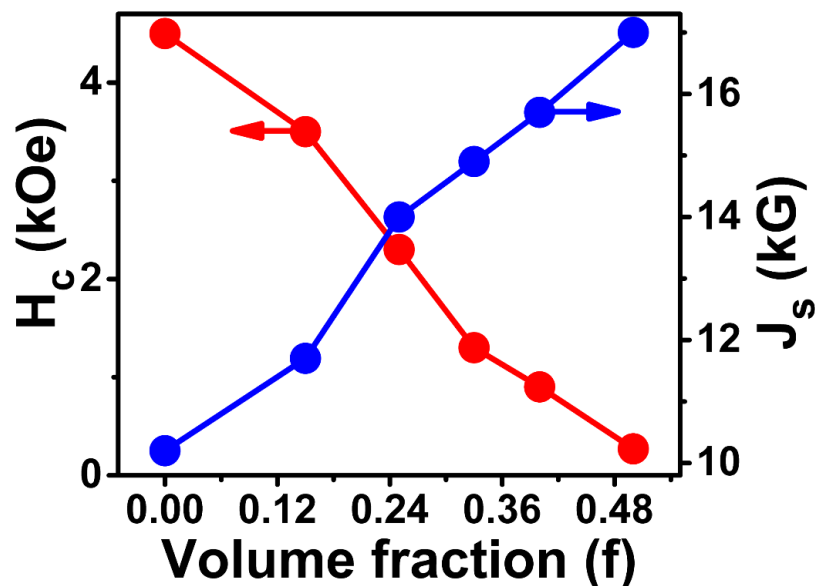


Figure 5.3.4. Trend of H_c (red curve) and J_s (blue curve) of the Zr_2Co_{11} :Fe-Co nanocomposites with variation of soft phase volume fraction (f).

Figure 5.3.4 shows the variation of H_c and J_s of the nanocomposite films with change in the volume fraction (f) of the soft phase which is determined by factoring the vol. % with 100 % ($f = \frac{\text{vol.}\%}{100\%}$). Decrease in H_c from 4.5 to 0.3 kOe and increase in J_s from

10.2 to 17 kG are observed with increasing f (from 0 to 0.5 corresponding to 0 to 50 vol. %) which is expected for the magnetic nanocomposites.

A key requirement of exchange-coupled nanocomposites is to achieve a high volume fraction of the soft phase without killing the coercivity which is observed in $\text{Zr}_2\text{Co}_{11}:\text{Fe-Co}$ system showing appreciable H_c (about 1.5 kOe) for high f up to 0.33.

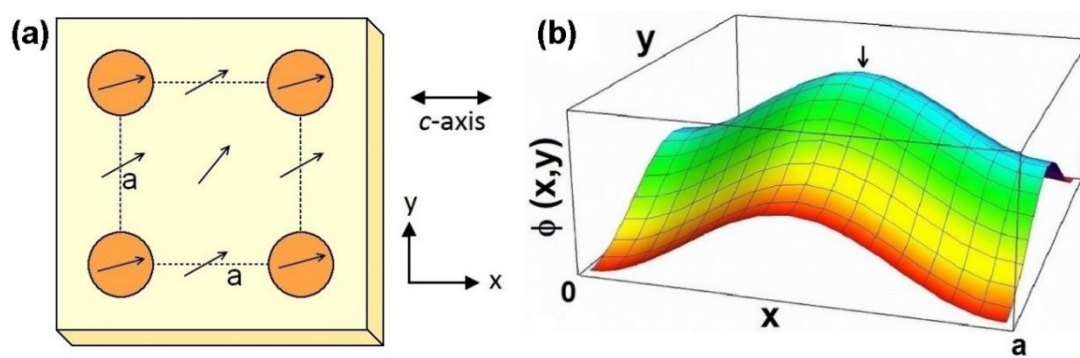


Figure 5.3.5. Model nanocomposite structure. (a) Schematic spin structure near coercivity. Brown and yellow regions denote hard and soft regions, respectively and a is the center-to-center distance of the hard regions, or the edge length of the dashed square. (b) The simulated spin distribution $\phi(x, y)$ as a function of x and y . The center of the soft region is indicated by an arrow.

To explain the high H_c , the model structure shown in Fig. 5.3.5 (a) is used where a is the center-to-center distance between the hard regions, or the edge length of the dashed square. In this coordinate frame, the alignment field H_{a1} , the measurement field H , and the c -axis (crystallographic easy axis) alignment are all in the x -direction. The absence of a pronounced shoulder in the hysteresis loop and the smallness of the feature sizes indicate nearly perfect exchange coupling. In this limit, the nucleation mode is nearly coherent and can be written as $\phi(x, y) = \phi_0 + \phi_1(x, y)$, where ϕ is the local

magnetization angle relative to the c -axis, ϕ_0 is the coherent magnetization angle, and $\phi_1(x, y)$ is the incoherent contribution.[17,18] Nucleation starts in the middle of the soft regions, and the exchange stiffness suppresses abrupt changes in the spin direction. This indicates that the long-wavelength Fourier components of the magnetization are only significant and ϕ can be expressed as,

$$\phi(x, y) = \phi_0 - \frac{1}{2} b \phi_0 [\cos(2\pi x/a) + \cos(2\pi y/a)] \quad 5.1$$

Here, $x = 0$ and $y = 0$ are in the center of the bottom-left hard particle in Fig. 5.3.5 (a) and b describes the relative strength of the incoherent part.

The dimensionless parameter b is determined by minimizing the micromagnetic (free) energy written as,

$$E = \int A \left(\left(\frac{\partial \phi}{\partial x} \right)^2 + \left(\frac{\partial \phi}{\partial y} \right)^2 + K(x, y) - \frac{1}{2} M_s(x, y) H \right) dx dy \quad 5.2$$

which yields the nucleation field,[19]

$$H_N = \frac{2K_1}{M_s} \left(1 - f \frac{M_{\text{soft}}}{\langle M \rangle} \right) \left(1 - \frac{f^2 (1-f) a^2}{\delta_h^2} \frac{M_{\text{soft}}^2}{\langle M \rangle^2} \right) - D_{\text{eff}} \langle M \rangle \quad 5.3$$

Here, K_1 and M_s are the magnetic anisotropy constant and saturation magnetization of the hard phase, respectively, and f is the volume fraction of the soft phase, M_{soft} is the saturation magnetization of the soft phase and $\langle M \rangle$ is the average saturation magnetization of the system. D_{eff} is the demagnetization factor which is

assumed to be zero for thin films with in-plane applied magnetic field parallel to easy-axis which is the present case.

Figure 5.3.5 (b) shows the distribution of $\phi(x, y)$ or spin structure during the demagnetization in the nanocomposite samples. The nucleation starts from the center of the soft phase as indicated by arrow in Fig. 5.3.5 (b). By the definition of the present model, the correction term in the right-hand side of Eqn. 5.3 must be small, and thus the idealized structure of Fig. 5.3.5 (a) corresponds to a rectangular hysteresis loops with remanence $M_r = M_s$ and $H_c = H_N$. However, the experimentally produced structures are disordered and this leads to a smoothing of the hysteresis loops. The result of the multiplication of the terms in parenthesis in Eqn. 5.3 can be expressed as α , a modified Kronmüller factor for nanocomposite films which is about 0.7 obtained by numerical calculation for ideal system.[19] This indicates, a reduction of H_c of about 70 % for the nanocomposites from the H_c of the pure hard phase.[1,19] As an example, in the case of experimental results for $Zr_2Co_{11}:Fe-Co$ nanocomposite film with $f = 0.15$, a H_c of 3.5 kOe was obtained which is about 77 % of the H_c obtained for hard Zr_2Co_{11} nanoclusters.

5.3.4 Energy Products

Energy product $[(BH)_{\max}]$ is important as a figure of merit for the efficiency of nanocomposite magnets. Optimal composition of hard and soft phases plays crucial role in determining the nominal energy product of the nanocomposite films. Although, $(BH)_{\max}$ varies in proportion with $B_r^2/4$ (B_r is the remanent magnetic induction), the value of H_c is important to get the large area in $B-H$ loop leading to high energy-product.

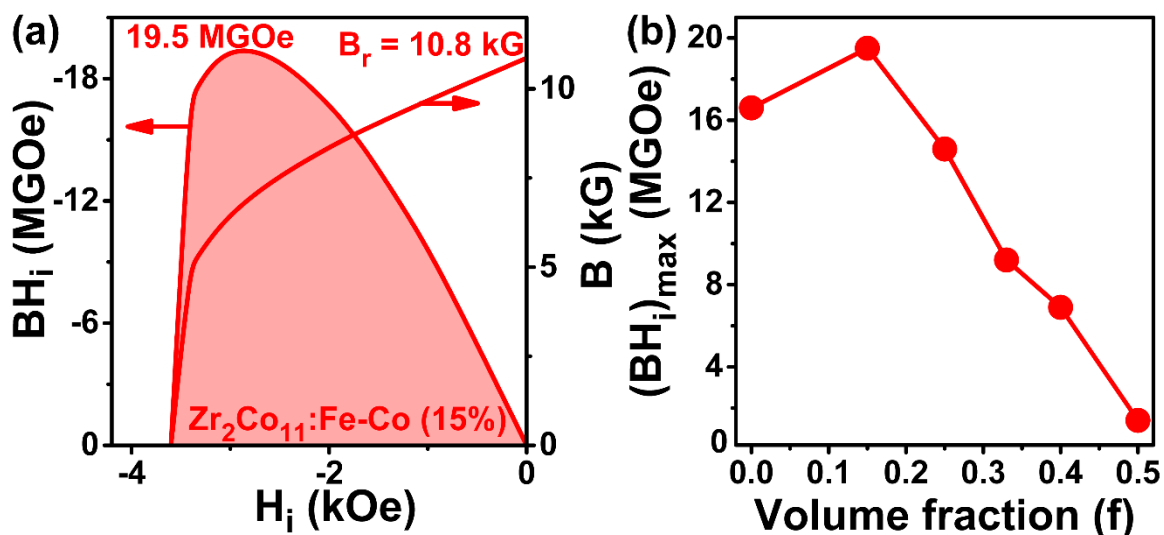


Figure 5.3.6. Energy product at Room Temperature. (a) Change in BH_i and B with H_i (internal field) for nanocomposite film with 15 vol. % ($f = 0.15$) of soft phase; (b) variation of $(BH_i)_{max}$ with f .

Figure 5.3.6 (a) shows the change in the nominal energy product (BH_i) and B with the internal magnetic field (H_i) for $Zr_2Co_{11}:Fe-Co$ nanocomposite film with $f = 0.15$. A large maximum energy product [$(BH_i)_{max}$] of about 19.5 MGOe was obtained for $f = 0.15$ or 15 vol. % of Fe-Co, which is one of the largest values obtained for rare-earth and Pt free permanent magnet materials.[19-23] Change in $(BH_i)_{max}$ with the soft-phase volume fraction f is shown in Fig. 5.3.6 (b) which shows a decrease in energy product with increasing f but remains appreciable up to $f = 0.33$ with corresponding value of 9.2 MGOe suitable for permanent-magnet applications. Nanocomposites with 50 vol. % ($f = 0.5$) of soft phase exhibits low energy product [$(BH_i)_{max} < 1.5$ MGOe] predominantly due to reduction of H_c which indicates strong dependence on coercivity of the energy-products for hard-soft composite films.

5.4 Conclusions

Synthesis of magnetic nanocomposite dense films consisting of hard Zr_2Co_{11} nanoclusters dispersed in soft Fe-Co matrix is demonstrated in this chapter with different volume fractions (f) of the soft phase. Study of the magnetic properties indicate slow decrease rate of H_c with increasing f which helps to retain a high energy-product of the composite films. The micromagnetic calculations using a model structure indicates a high remanent magnetization and a small hysteresis-loop slope near remanence due to perfect exchange-coupling between the soft and hard phases. This behavior is also evident from the experimental hysteresis loops and results in high energy products (9.2 - 19.5 MGOe) for nanocomposites having volume fractions in the range of 15 to 33%. The largest value of the energy-product (19.5 MGOe) is obtained for $f = 15$ which is higher than that obtained for commercially available alnico or other rare-earth or Pt free magnets. Scaling up of the nanocomposite magnets using hard-magnetic nanocluster building blocks is challenging and needs further research for commercialization. However, this study is quintessential to obtain insights for developing next generation composite magnets for practical permanent-magnet applications.

References:

- [1] E. F. Kneller and R. Hawig, The Exchange-Spring Magnet - a New Material Principle for Permanent-Magnets, *IEEE Transactions on Magnetics* **27**, 3588 (1991).
- [2] R. Skomski and J. M. D. Coey, Giant Energy Product in Nanostructured 2-Phase Magnets, *Physical Review B* **48**, 15812 (1993).
- [3] D. J. Sellmyer, Applied physics - Strong magnets by self-assembly, *Nature* **420**, 374 (2002).
- [4] H. Zeng, J. Li, J. P. Liu, Z. L. Wang, and S. H. Sun, Exchange-coupled nanocomposite magnets by nanoparticle self-assembly, *Nature* **420**, 395 (2002).
- [5] C. B. Rong, Y. Zhang, N. Poudyal, X. Y. Xiong, M. J. Kramer, and J. P. Liu, Fabrication of bulk nanocomposite magnets via severe plastic deformation and warm compaction, *Applied Physics Letters* **96** (2010).
- [6] W. B. Cui, Y. K. Takahashi, and K. Hono, Nd₂Fe₁₄B/FeCo Anisotropic Nanocomposite Films with a Large Maximum Energy Product, *Advanced Materials* **24**, 6530 (2012).
- [7] V. Neu, S. Sawatzki, M. Kopte, C. Mickel, and L. Schultz, Fully Epitaxial, Exchange Coupled SmCo₅/Fe Multilayers With Energy Densities above 400 kJ/m³, *IEEE Transactions on Magnetics* **48**, 3599 (2012).
- [8] X. Y. Zhang, Y. Guan, L. Yang, and J. W. Zhang, Crystallographic texture and magnetic anisotropy of alpha-Fe/Nd₂Fe₁₄B nanocomposites prepared by controlled melt spinning, *Applied Physics Letters* **79**, 2426 (2001).
- [9] J. M. D. Coey, Permanent magnets: Plugging the gap, *Scripta Materialia* **67**, 524 (2012).
- [10] M. Jacoby, Powerful Pull to New Magnets, *Chemical & Engineering News* **91**, 23 (2013).
- [11] S. Nieber and H. Kronmuller, Nucleation Fields in Periodic Multilayers, *Physica Status Solidi B-Basic Research* **153**, 367 (1989).
- [12] G. C. Hadjipanayis, W. Tang, Y. Zhang, S. T. Chui, J. F. Liu, C. Chen, and H. Kronmuller, High temperature 2 : 17 magnets: Relationship of magnetic properties to microstructure and processing, *IEEE Transactions on Magnetics* **36**, 3382 (2000).
- [13] C. H. Chen, M. S. Walmer, M. H. Walmer, S. Liu, E. Kuhl, and G. Simon, Sm₂(Co,Fe,Cu,Zr)₁₇ magnets for use at temperature $\geq 400^\circ\text{C}$, *Journal of Applied Physics* **83**, 6706 (1998).

- [14] S. Liu, E. P. Hoffman, and J. R. Brown, Long-term aging of Sm₂(Co,Fe,Cu,Zr)₁₇ permanent magnets at 300 and 400° C, *IEEE Transactions on Magnetics* **33**, 3859 (1997).
- [15] J. M. D. Coey, *Magnetism and magnetic materials* (Cambridge University Press, Cambridge ; New York, 2009).
- [16] A. Poorbafrani, H. Salamati, and P. Kameli, Exchange spring behavior in Co_{0.6}Zn_{0.4}Fe₂O₄/SrFe_{10.5}O_{16.75} nanocomposites, *Ceramics International* **41**, 1603 (2015).
- [17] R. Skomski, Nanomagnetism, *Journal of Physics-Condensed Matter* **15**, R841 (2003).
- [18] R. Skomski and J. M. D. Coey, Exchange Coupling and Energy Product in Random 2-Phase Aligned Magnets, *IEEE Transactions on Magnetics* **30**, 607 (1994).
- [19] B. Balasubramanian, P. Mukherjee, R. Skomski, P. Manchanda, B. Das, and D. J. Sellmyer, Magnetic nanostructuring and overcoming Brown's paradox to realize extraordinary high-temperature energy products, *Scientific Reports* **4** (2014).
- [20] J. H. Park, Y. K. Hong, S. Bae, J. J. Lee, J. Jalli, G. S. Abo, N. Neveu, S. G. Kim, C. J. Choi, and J. G. Lee, Saturation magnetization and crystalline anisotropy calculations for MnAl permanent magnet, *Journal of Applied Physics* **107**, 09A731 (2010).
- [21] J. B. Yang, K. Kamaraju, W. B. Yelon, W. J. James, Q. Cai, and A. Bollero, Magnetic properties of the MnBi intermetallic compound, *Applied Physics Letters* **79**, 1846 (2001).
- [22] M. A. McGuire, O. Rios, N. J. Ghimire, and M. Koehler, Hard ferromagnetism in melt-spun Hf₂Co₁₁B alloys, *Applied Physics Letters* **101** (2012).
- [23] B. Balke, G. H. Fecher, J. Winterlik, and C. Felser, Mn₃Ga, a compensated ferrimagnet with high Curie temperature and low magnetic moment for spin torque transfer applications, *Applied Physics Letters* **90** (2007).

CHAPTER 6. SIZE-ENHANCED MAGNETIC PROPERTIES OF Mn AND Fe -BASED SILICIDE NANOCLUSTERS

Spin-structure changes drastically from bulk to at nanoscale due to surface effect or high surface to volume ratio compared to bulk. New magnetic properties are discovered in the case of nanoclusters which are not known for bulk or thin films. In this study, effect of surface-spins on the magnetic properties of Mn and Fe-based silicides are discussed which are reported as potential candidates for spintronics applications. Density functional theory is used to understand the physics of magnetism in these nanoclusters.

Many of the results presented in this chapter are adapted from the publication: “Mn₅Si₃ Nanoparticles: Synthesis and Size-induced Ferromagnetism”, B. Das, B. Balamurugan, P. Manchanda, P. Mukherjee, R. Skomski, G. C. Hadjipanayis and D. J. Sellmyer, *Nano Letters*, 16, 1132 (2016).

I fabricated the Mn₅Si₃ and Fe₅Si₃ nanoclusters and analyzed the results. B. Balamurugan and I wrote the manuscript. R. Skomski and P. Manchanda performed the density-functional theory and simulations. P. Mukherjee helped with the TEM measurements and analysis. All co-authors contributed with ideas and criticized the manuscript.

6.1 Introduction

Electron spins on the surface of nanoclusters with sizes less than 10 nm behave differently from the spins those are at the core due to very high surface to volume ratio which usually absent in case of bulk materials with large grain sizes.[1] This surface effect becomes interesting for ferromagnetic materials such as Mn or Fe due to their large magnetic moments which drive the spin-polarization on the surface of the nanoclusters. Mn-based intermetallic compounds are fascinating due to their exotic spin textures and unique crystal structures which facilitate them as a central focus of research in magnetism from the viewpoints of developing new rare-earth-free permanent magnets and magnetic materials with interesting spin-electronic properties.[2,3] Among various Mn or Fe based magnetic materials, their silicides are of special interest due to potential applications in spintronics and semiconductor-magnetics.[4,5] The elemental magnetic moment of Mn is larger than those of Fe and Co, but Mn atoms tend to exhibit antiferromagnetic interactions, which reduce net magnetization and Curie temperature. In this regard, Mn_5Si_3 is a promising material due to its hexagonal crystal structure [D_{8h} -type hexagonal structure with space group P6₃/mcm as shown in Fig. 6.1.1] that has potential for creating a high magnetocrystalline anisotropy.

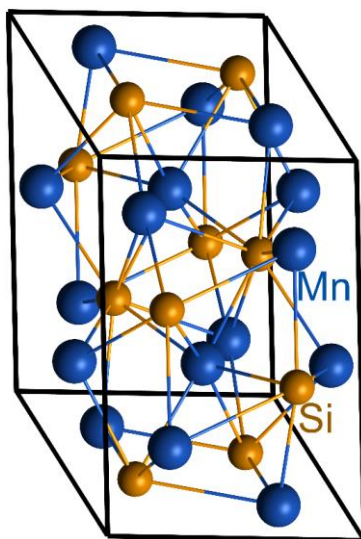


Figure 6.1.1. D_{8h} -type hexagonal crystal structure of Mn₅Si₃.

However, bulk Mn₅Si₃ is paramagnetic at room temperature and transforms at around 100 K into a non-collinear orthorhombic phase, that exhibits only antiferromagnetic ordering.[6-9] Interestingly, carbon doping has been observed to stabilize ferromagnetic ordering in Mn₅Si₃ bulk and thin films, due to a carbon-mediated superexchange between two neighboring Mn atoms.[10-13] Fe₅Si₃ is a silicide which also possesses the same D_{8h} -type hexagonal crystal structure which shows ferromagnetic properties in the form of thin films, carbon-encapsulated isolated nanostructures, and nanowires with diameters lying in the range between 100 – 200 nm and lengths of the order of microns.[14,15] However, ferromagnetic properties of these nanostructures and films are weak and close to those for bulk Fe₅Si₃ with low magnetization not suitable for practical applications.

Although the previous studies show relatively low magnetic moments of up to $1.0 \mu_B/\text{Mn}$ and Curie temperatures just above the room temperature ($T_c \approx 350 \text{ K}$) in carbon-doped Mn_5Si_3 , the results suggest that a small perturbation in the electronic structure can have strong effects on its magnetic properties. Hence, nanostructuring is an effective approach to modify the electronic structure of Mn_5Si_3 and Fe_5Si_3 by utilizing nanoscale effects that can substantially improve their magnetic properties and/or inducing new properties entirely different from the bulk.[1,16,17] This chapter focusses on the spin-polarization at the nanocluster surfaces and its effect on the magnetization and anisotropy of nanocluster-deposited Mn_5Si_3 and Fe_5Si_3 films.

6.2 Structure of Mn_5Si_3 and Fe_5Si_3 Nanoclusters

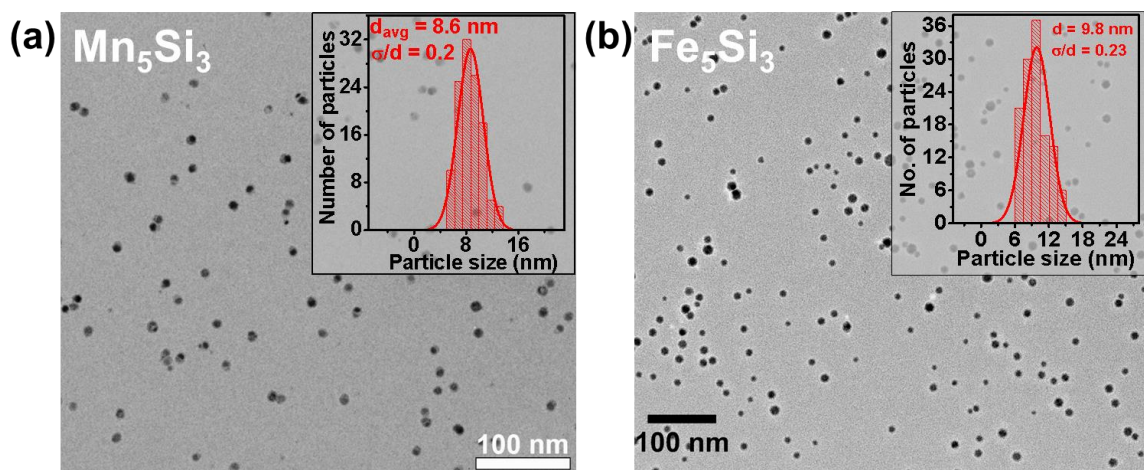


Figure 6.2.1. LRTEM image of (a) Mn_5Si_3 and, (b) Fe_5Si_3 nanoclusters showing the cluster size distribution and the average cluster size in the corresponding insets.

Figure 6.2.1 shows the low resolution TEM (LRTEM) images of the Mn_5Si_3 [Fig. 6.2.1 (a)] and Fe_5Si_3 [Fig. 6.2.1 (b)] nanoclusters showing average cluster sizes less than 10 nm [average size of Mn_5Si_3 nanoclusters is 8.6 nm and that of the Fe_5Si_3 nanoclusters is 9.8 nm] with narrow size distribution shown in the insets with relative standard deviation values (σ/d) 0.2 and 0.23 for the two systems respectively.

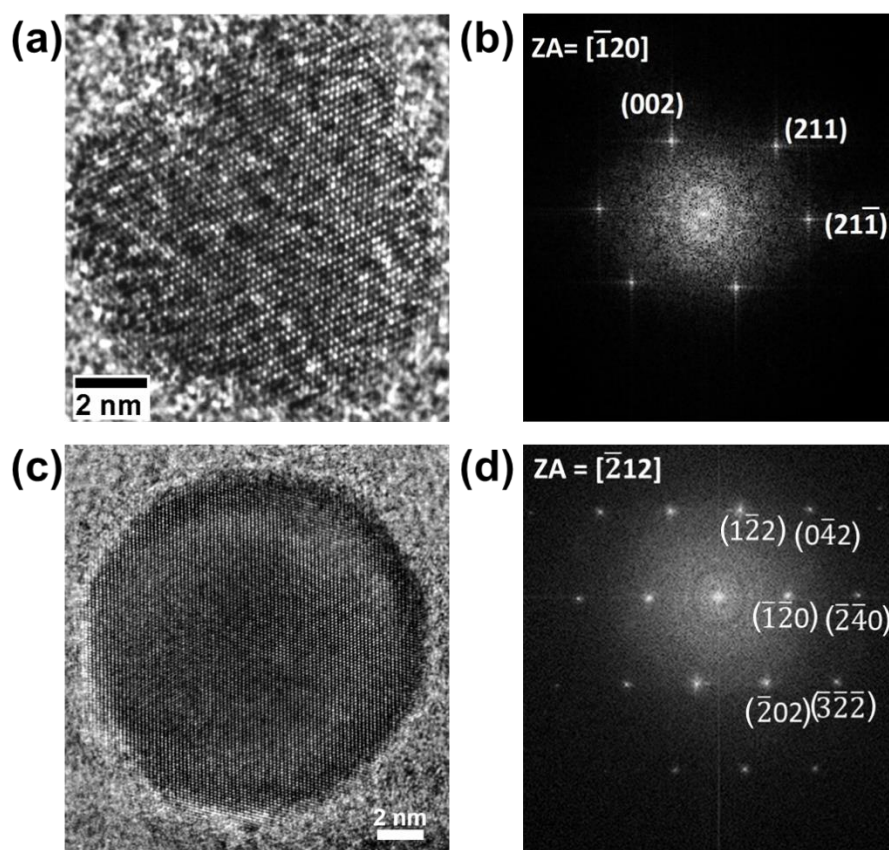


Figure 6.2.2. HRTEM images of a single nanocluster of (a) Mn_5Si_3 and (c) Fe_5Si_3 with the corresponding FFT images shown in (b) and (d) respectively.

HRTEM of both the nanoclusters are shown in Fig. 6.2.2 [(a) Mn_5Si_3 and (c) Fe_5Si_3] with the corresponding FFTs [(b) Mn_5Si_3 along $[\bar{1} 2 0]$ zone axis and (c) Fe_5Si_3 along $[\bar{2} 1 2]$ zone axis] indexed with D8₈-type hexagonal crystal structure which are

also verified using XRD. It is clear from the distinct lattice fringes seen in the HRTEM images that both Mn_5Si_3 and Fe_5Si_3 nanoclusters are single crystalline with high degree of atomic ordering.

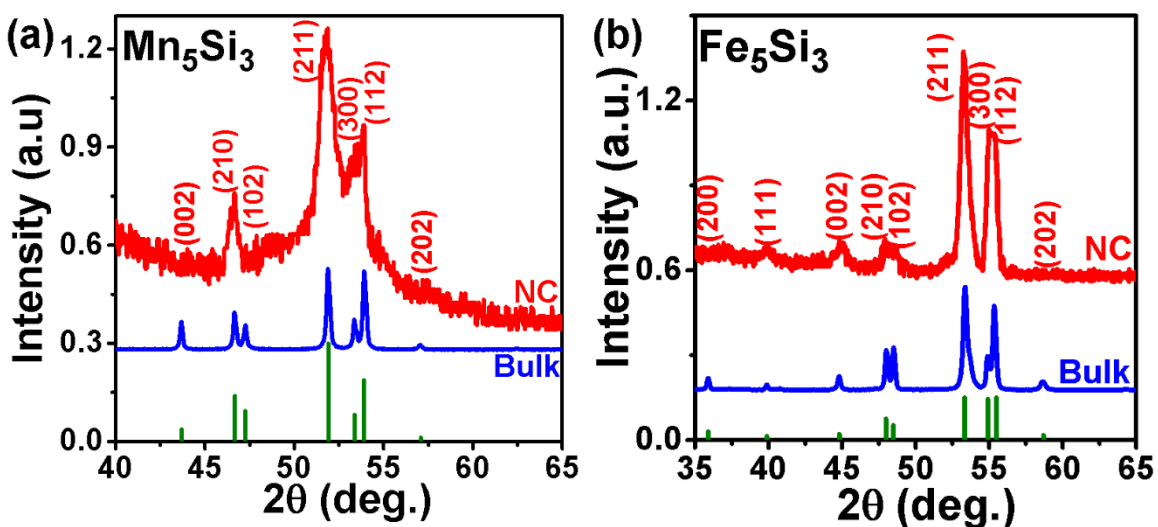


Figure 6.2.3. XRD of the nanoclusters shown in red curve compared to that of bulk (in blue curve) and standard data (in green straight lines) for (a) Mn_5Si_3 and, (b) Fe_5Si_3 .

Fig. 6.2.3 (a) shows the XRD pattern of Mn_5Si_3 nanoclusters (red curve) which also exhibits D8_8 -type hexagonal crystal structure as compared to the standard XRD data (green straight lines) and bulk (blue curve).[18,19] Similar crystal structure is obtained for Fe_5Si_3 nanoclusters (red curve) as shown in the Fig. 6.2.3 (b) which also shows the comparison with the standard data (green starlight lines) for the Fe_5Si_3 with hexagonal structure (prototype – Mn_5Si_3).[20] Thus, both the nanoclusters are highly ordered and crystallize in hexagonal crystal structure as supported by TEM and XRD studies. To explore their potential for magnetic applications, it is important to perform magnetic characterization which will be discussed for both the systems in the following sections.

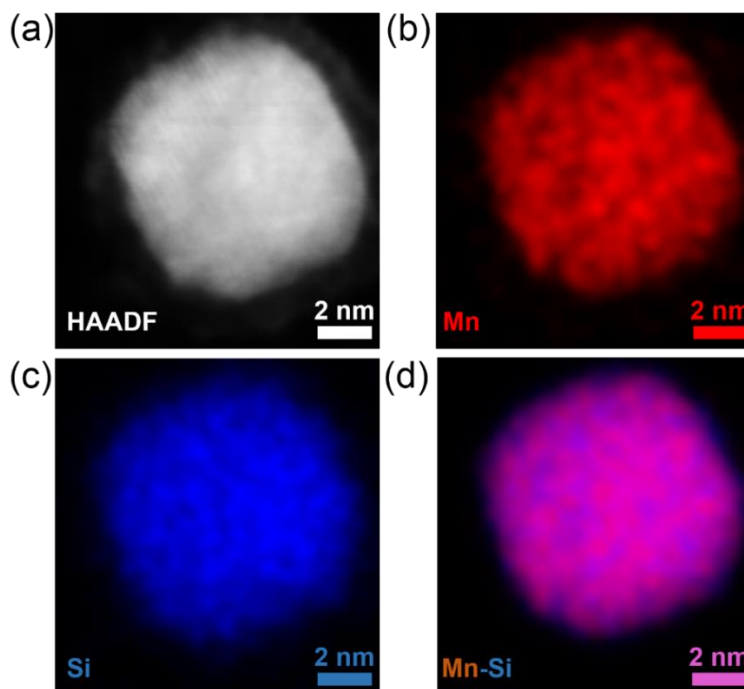


Figure 6.2.4. Scanning Transmission Electron Microscopy: (a) High-Angle Annular Dark-Field (HAADF) image of a single Mn_5Si_3 nanocluster showing homogeneous atomic number (Z) contrast distribution supported by Energy Dispersive X-ray (EDX) color mapping of (b) Mn, (c) Si and, (d) combined Mn and Si.

Fig. 6.2.4 (a) shows a High-Angle Annular Dark-Field (HAADF) image with atomic number (Z) contrast for a single Mn_5Si_3 nanocluster. The composition of the nanoclusters was studied and verified using Energy Dispersive X-ray (EDX) measurements in STEM mode and the corresponding color mapping of Mn, Si and combined Mn-Si elemental distribution are shown in figures 6.2.4 (b), (c) and (d) respectively. The study exhibits a uniform distribution of Mn and Si over the nanocluster indicated by the homogeneous contrast and color distribution in Fig. 6.2.4 (a) and (d) respectively, and a similar trend was obtained also for the Fe_5Si_3 nanoclusters (not shown here due to similarity of the data).

6.3 Magnetic Properties: Mn_5Si_3 Nanoclusters

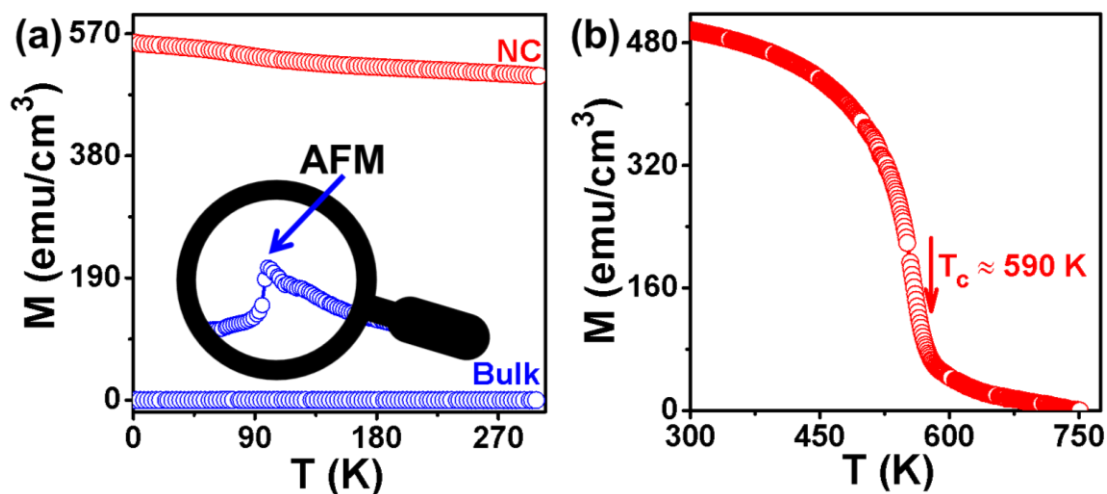


Figure 6.3.1. (a) Magnetization (M) measured as a function of temperature (T) in a magnetic field of 1 kOe. The M - T curve for the bulk alloy is magnified in the inset to show clearly the antiferromagnetic transition at 99 K. (b) M - T curve for the nanoclusters measured in the temperature range of 300 – 850 K, where the Curie temperature T_c is indicated by an arrow.

The temperature-dependent magnetization curves of Mn_5Si_3 nanoclusters is shown in Fig. 6.3.1 (a) by the red curve which is also compared to the M - T curve for bulk Mn_5Si_3 (blue curve). The bulk alloy exhibits negligibly small magnetization, mainly due to its antiferromagnetic behavior. Generally, bulk Mn_5Si_3 is paramagnetic at room temperature and expected to exhibit a structural transition from the hexagonal to orthorhombic structure at 100 K, which accompanies antiferromagnetic transition at 99 K, as clearly shown in the inset of Fig. 6.3.1 (a) which is basically the magnified version of the bulk M - T curve near 99 K.[6,21] In comparison, the nanoclusters exhibit an enhanced magnetization by about three orders of magnitude, which indicates a possible

ferromagnetic ordering with a Curie temperature T_c higher than 300 K. The measured M - T curve at elevated temperatures, Fig. 6.3.1 (b), suggests a T_c close to 590 K for the nanoclusters.

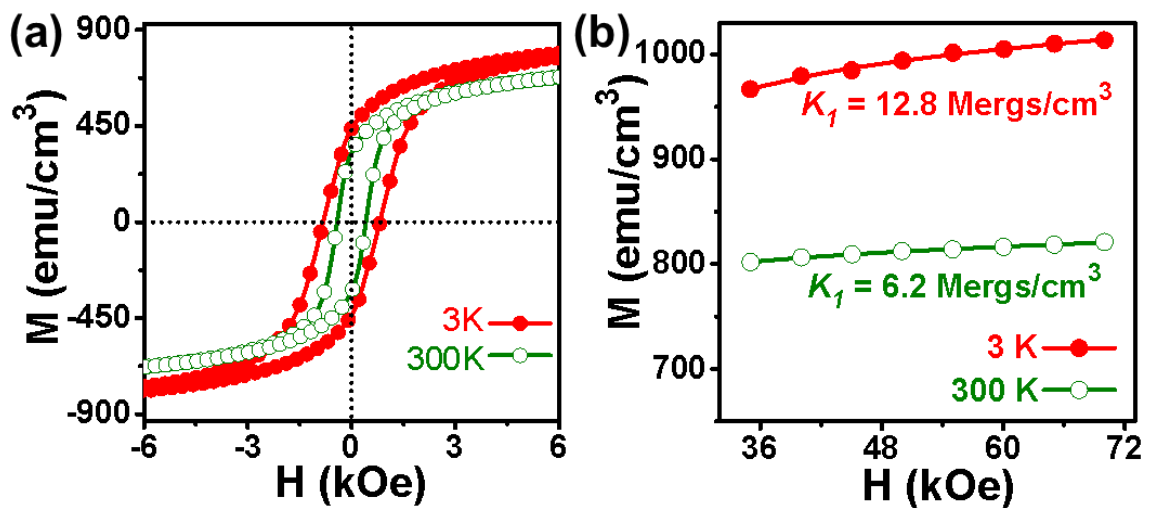


Figure 6.3.2. (a) The magnetic hysteresis loops of the isotropic (unaligned) nanoclusters measured at 3 K (red curve) and 300 K (green curve). (b) The experimental magnetization curves (spheres) of the nanoclusters at high-field region (35 – 70 kOe) were fitted (lines) using the law-of-approach to saturation method to determine magnetocrystalline anisotropy constant K_1 .

The magnetization curves of the Mn_5Si_3 nanoclusters measured as a function of applied field H from -70 kOe to + 70 kOe reveal a large saturation magnetization (M_s), and appreciable coercivities (H_c). For example, the expanded M - H loops of the nanoclusters, Fig. 6.3.2 (a), show $H_c = 0.50$ and 0.90 kOe at 300 and 3 K, respectively. Most importantly, M does not saturate even for a high field (70 kOe) as shown in Fig. 6.3.2 (b), suggesting a significant magnetocrystalline anisotropy constant K_1 . In Fig. 6.3.2

(b), the experimental magnetization data at high field were fitted using the law-of-approach to saturation method (Appendix A) and this analysis yields $K_1 = 12.8$ Mergs/cm³ and $M_s = 983$ emu/cm³ ($J_s = 12.4$ kG) at 3 K [$K_1 = 6.2$ Mergs/cm³ and $M_s = 802$ emu/cm³ ($J_s = 10.1$ kG) at 300 K].

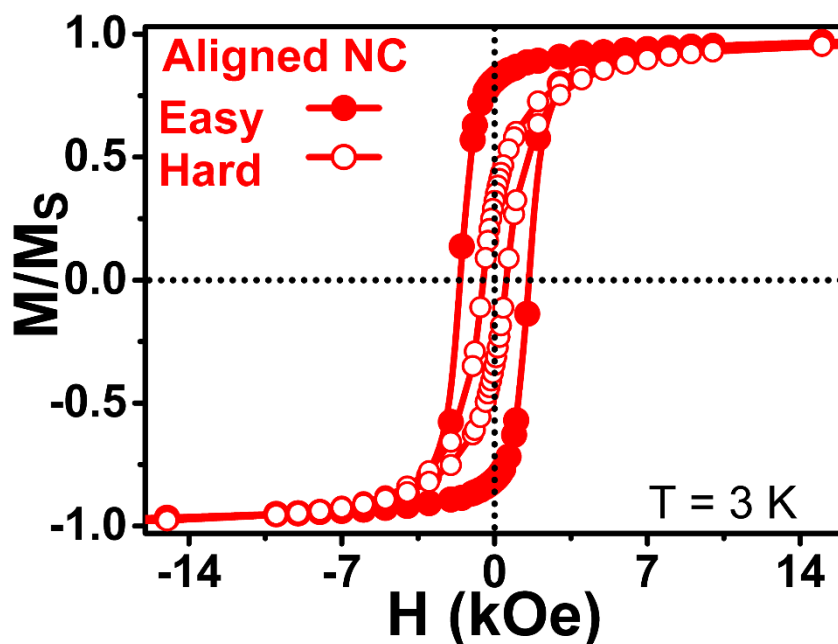


Figure 6.3.3. Easy-axis aligned Mn_5Si_3 nanoclusters showing in-plane hysteresis loops measured along the easy and hard directions.

The strong magnetic crystalline anisotropy of Mn_5Si_3 nanoclusters is also revealed from the easy-axis alignment experiment for uniaxial nanoclusters. Due to this anisotropic nature, the nanoclusters were successfully aligned using an external magnetic field of about 5 kOe, as described in earlier chapters. The magnetic hysteresis loops of the aligned (anisotropic) nanoclusters is shown in Fig. 6.3.3, which exhibits an appreciable coercivity, $H_c = 1.7$ kOe (at 3 K), which is larger than that for the isotropic

nanoclusters. A high remanence ratio $M_r/M_s = 0.82$ along the easy axis was obtained as compared to those measured along the hard axis ($H_c = 0.50$ kOe and $M_r/M_s = 0.3$) which also ensures a high degree of alignment and appreciable magnetocrystalline anisotropy present in the nanoclusters. Note that, for aligned Mn_5Si_3 nanoclusters at 300 K, $H_c = 0.9$ kOe and $M_r/M_s = 0.84$ along the easy direction.

6.4 DFT Results for Mn_5Si_3 nanoclusters

The experimental results show that Mn_5Si_3 nanoclusters are ferromagnetic with a high $T_c \approx 590$ K, and a large saturation magnetic polarization, $J_s = 12.4$ kG, which corresponds to an average magnetic moment $\langle m \rangle = 2.2 \mu_B/Mn$. In order to understand the magnetic properties of the nanoclusters, first-principle density-functional theory (DFT) calculations using the projected augmented wave method (PAW), as implemented in the Vienna ab-initio simulation package (VASP) have been used.[22,23] The exchange-correlation effects were implemented by generalized-gradient approximation (GGA-PBE) and a supercell with 15 Å vacuum spaces in the x , y , and z directions is used to exclude interactions between the neighboring nanoclusters.[24] For the nanocluster, the Γ -point was used for k -point sampling due to the large supercell. The atomic positions for the nanoclusters were relaxed until the force acting on each atom was less than 0.1 eV/Å, and a convergence criteria of 1×10^{-5} eV has been used for electronic structure calculations.

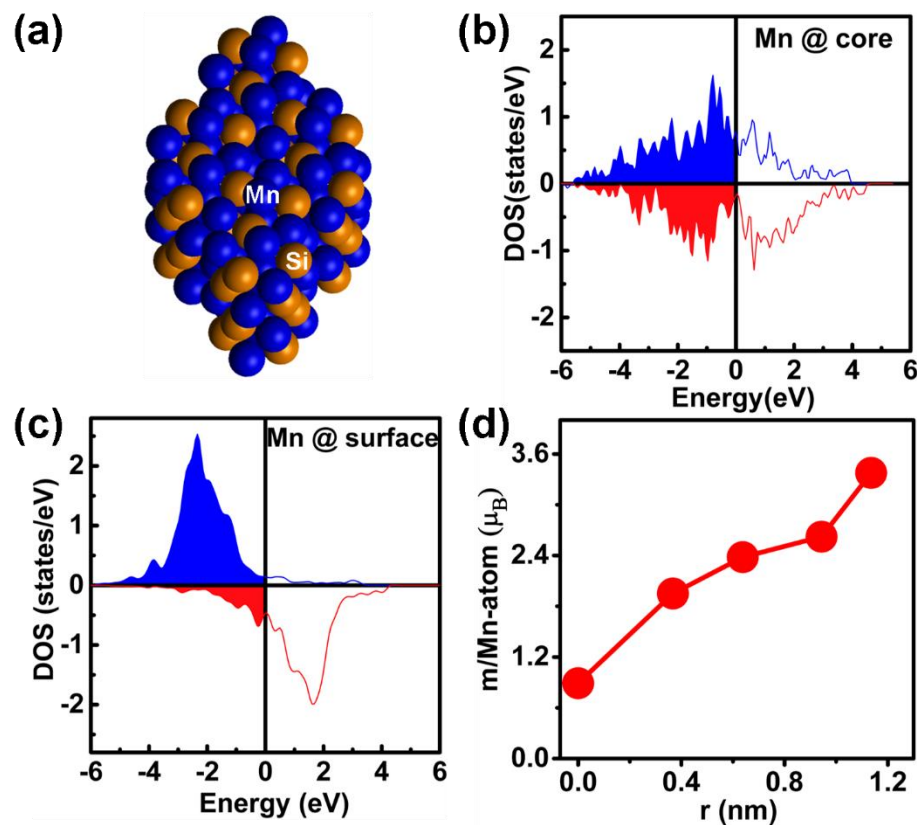


Figure 6.4.1. DFT results of Mn₅Si₃ nanoclusters: (a) Schematic of a nanocluster having 128 atoms. Density of states for (b) core Mn and (c) surface Mn atoms. (d) Radial distribution of magnetic moments from the center to the surface.

The simulations were performed for a hexagonal nanocluster having 128 atoms as schematically shown in Fig. 6.4.1 (a) and yield $\langle m \rangle = 2.7 \mu_B/\text{Mn}$, in an agreement with the experimental value $\langle m \rangle = 2.2 \mu_B/\text{Mn}$. The DFT analysis also reveals a large magnetic moment of about $3.2 \mu_B/\text{Mn}$ for surface atoms as compared to $0.85 \mu_B/\text{Mn}$ for core atoms. Furthermore, this result can be explained by comparing the calculated densities of states (DOS) for the core Mn atoms [Figure 6.4.1 (b)] and that of surface Mn atoms [Figure 6.4.1 (c)]. This surface effect is also reflected by an inhomogeneous distribution of the calculated magnetic moment across the nanocluster as shown in Fig. 6.4.1 (d). In brief,

Fig 6.4.1 (b)-(d) demonstrate a modified electronic structure at the nanocluster surface as compared to core, leading to a large surface spin polarization. It is also clear from the DOS study, that the large spin polarization at the nanocluster surface also polarizes the core to show ferromagnetic behavior. Note that a small perturbation in the electronic structure of Mn_5Si_3 bulk and thin films upon carbon doping have shown considerable effects on their magnetic properties.[10-13] Furthermore, the finite-size effects have shown to increase T_c with a decrease of cluster size in MnFe_2O_4 nanoclusters.[25] Thus, the unusual ferromagnetic ordering with a substantially high T_c and $\langle m \rangle$ observed in the case of Mn_5Si_3 nanoclusters is presumably a direct consequence of the modification in the electronic structure due to nanoscale effects, evident from Fig. 6.4.1 (b) and (c).

6.5 Magnetic Properties: Fe_5Si_3 Bulk and Nanoclusters

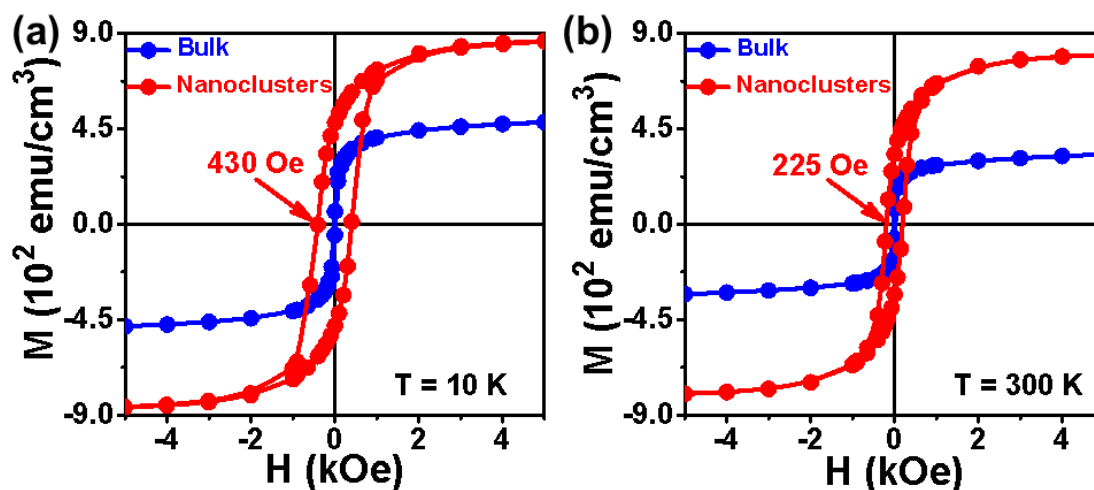


Figure 6.5.1. Magnetic hysteresis of Fe_5Si_3 nanoclusters (red curve) and bulk (blue curve) at (a) 10 K and (b) 300 K.

Comparison of magnetic properties of Fe_5Si_3 nanoclusters with the bulk exhibit appreciable enhancement of magnetization for the nanoclusters. The comparison is shown in Fig. 6.5.1 through the hysteresis loops of Fe_5Si_3 bulk (blue curve) and nanoclusters (red curve) at $T = 10$ K [Fig. 6.5.1 (a)] and 300 K [Fig. 6.5.1 (b)] which shows appreciable M_s of about 915 emu/cm^3 ($J_s = 11.5 \text{ kG}$) at 10 K with $H_c = 430 \text{ Oe}$ [$H_c = 200 \text{ Oe}$, $M_s = 845 \text{ emu/cm}^3$ and $J_s = 10.6 \text{ kG}$ at 300K]. These values are significantly higher than those obtained for bulk Fe_5Si_3 showing M_s of 560 emu/cm^3 [$J_s = 7.0 \text{ kG}$] at 10K [$M_s = 452 \text{ emu/cm}^3$ and $J_s = 5.6 \text{ kG}$ at 300 K] with zero coercivity exhibiting soft magnetic behavior.

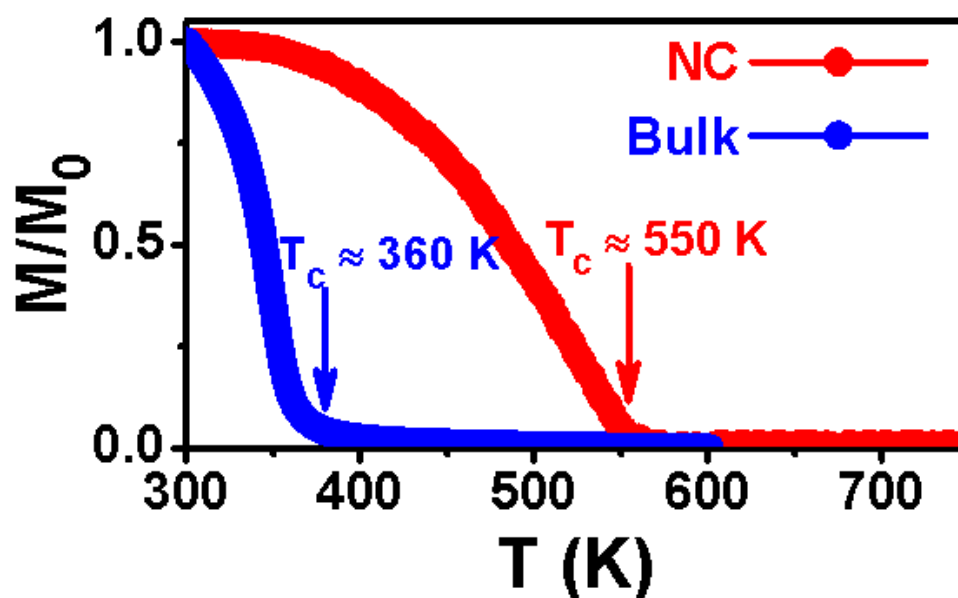


Figure 6.5.2. Dependence of magnetization on change in temperature for bulk (blue curve) and nanoclusters (red curve) of Fe_5Si_3 indicating respective Curie temperatures by arrows.

Figure 6.5.2 shows the variation of normalized magnetization M/M_0 with temperature (T) [M is the magnetization varying with temperature and M_0 is the magnetization at 10K] for the nanoclusters (red curve) and bulk (blue curve) Fe_5Si_3 . A T_c of about 550 K was obtained for the Fe_5Si_3 nanoclusters which is significantly higher than the bulk T_c of 360 K. The enhancement in magnetic properties can be attributed to the nanoscale effect of spin-polarization at the nanocluster surfaces similar to the phenomenon observed in Mn_5Si_3 nanoclusters. DFT calculations for Fe_5Si_3 nanoclusters are also done to verify this effect which is discussed in the following section.

6.6 DFT Study of Fe_5Si_3 nanoclusters

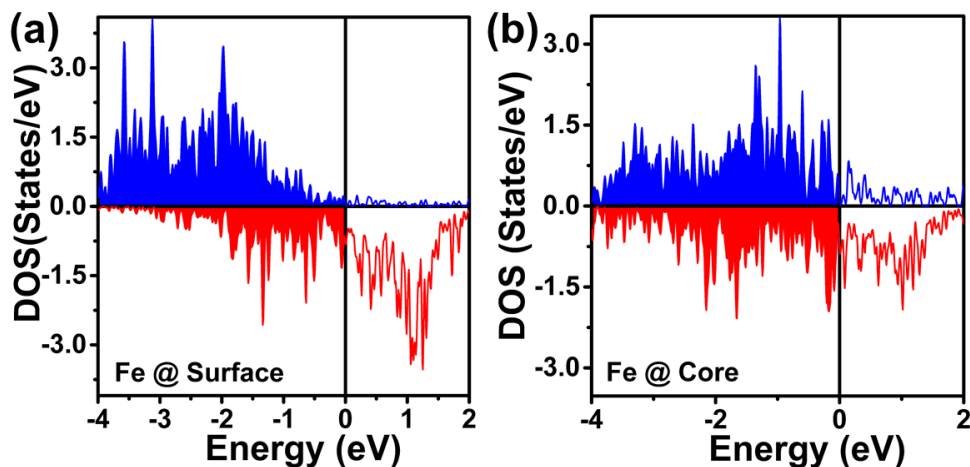


Figure 6.6.1. DOS for the Fe atoms at (a) surface and at (b) core of a Fe_5Si_3 nanocluster.

DFT calculations for the Fe_5Si_3 nanoclusters were performed using similar method described in section 6.4 for Mn_5Si_3 using a cluster of 128 atoms. Figure 6.6.1

shows the DOS for the Fe atoms at the surface and at the core of the nanocluster [Fig. 6.6.1 (a) and (b) respectively] indicating large spin-polarization at the surface compared to that at the core. Note that bulk Fe_5Si_3 is known to be ferromagnetic and hence it is obvious that the core of the nanocluster showing spin-polarization somewhat larger compared to that observed in the case of Mn_5Si_3 [Fig. 6.4.1 (b)]. The average magnetic moment of $2.1 \mu_{\text{B}}/\text{Fe}$ -atom was obtained from the DFT calculations which is close to the moment of about $1.8 \mu_{\text{B}}/\text{Fe}$ -atom obtained from the experiment.

6.7 Conclusions

Nanoscale confinement effects on spin-polarization at the nanocluster surfaces was studied with silicide nanoclusters. A large saturation magnetic polarization of about 12.4 kG (equivalent to an average magnetic moment of $2.2 \mu_{\text{B}}/\text{Mn}$) in Mn_5Si_3 nanoclusters was obtained, as compared to the nearly zero magnetic moment observed in the case of the antiferromagnetic bulk alloy. The first-principle calculations demonstrate that the surface-induced spin polarization is responsible for a high ferromagnetic moment in the nanoclusters. The nanoclusters also exhibit appreciable coercivities ($H_c = 1.7$ kOe at 3 K and 0.9 kOe at 300 K), mainly due to the underlying appreciable magnetocrystalline anisotropies at the corresponding temperatures. Similarly, spin-polarization-induced high magnetization was observed in Fe_5Si_3 nanoclusters which belong to the same space group as Mn_5Si_3 and has similar crystal structure and interestingly, exhibit a large T_c of about 550 K compared to that for the bulk [$T_c = 360$ K]. This study explains how the nanoscale

effects can be used to improve the magnetic properties of transition metal – based silicides, which may be emerging materials for significant magnetic and spintronics applications.

References:

- [1] B. Balasubramanian, P. Manchanda, R. Skomski, P. Mukherjee, B. Das, T. A. George, G. C. Hadjipanayis, and D. J. Sellmyer, Unusual spin correlations in a nanomagnet, *Applied Physics Letters* **106** (2015).
- [2] J. M. D. Coey, Permanent magnets: Plugging the gap, *Scripta Materialia* **67**, 524 (2012).
- [3] F. Jonietz *et al.*, Spin Transfer Torques in MnSi at Ultralow Current Densities, *Science* **330**, 1648 (2010).
- [4] C. G. Zeng, S. C. Erwin, L. C. Feldman, A. P. Li, R. Jin, Y. Song, J. R. Thompson, and H. H. Weiering, Epitaxial ferromagnetic Mn₅Ge₃ on Ge(111), *Applied Physics Letters* **83**, 5002 (2003).
- [5] P. C. Srivastava and J. K. Tripathi, Giant magnetoresistance (GMR) in swift heavy ion irradiated Fe films on c-silicon (Fe/c-Si), *Journal of Physics D-Applied Physics* **39**, 1465 (2006).
- [6] J. Leciejewicz, B. Penc, A. Szytula, A. Jezierski, and A. Zygmunt, Magnetic properties of the Mn₅Si₃ compound, *Acta Physica Polonica A* **113**, 1193 (2008).
- [7] M. R. Silva, P. J. Brown, and J. B. Forsyth, Magnetic moments and magnetic site susceptibilities in Mn₅Si₃, *Journal of Physics-Condensed Matter* **14**, 8707 (2002).
- [8] P. J. Brown, J. B. Forsyth, V. Nunez, and F. Tasset, The Low-Temperature Antiferromagnetic Structure of Mn₅Si₃ Revised in the Light of Neutron Polarimetry, *Journal of Physics-Condensed Matter* **4**, 10025 (1992).
- [9] C. Surgers, G. Fischer, P. Winkel, and H. V. Lohneysen, Large topological Hall effect in the non-collinear phase of an antiferromagnet, *Nature Communications* **5** (2014).
- [10] C. Suergers, K. Potzger, and G. Fischer, Magnetism of carbon doped Mn₅Si₃ and Mn₅Ge₃ films, *Journal of Chemical Sciences* **121**, 173 (2009).
- [11] B. Gopalakrishnan, C. Surgers, R. Montbrun, A. Singh, M. Uhlarz, and H. Von Lohneysen, Electronic transport in magnetically ordered Mn₅Si₃C_x films, *Physical Review B* **77** (2008).
- [12] C. Surgers, M. Gajdzik, G. Fischer, H. von Lohneysen, E. Welter, and K. Attenkofer, Preparation and structural characterization of ferromagnetic Mn₅Si₃C_x films, *Physical Review B* **68** (2003).
- [13] M. Gajdzik, C. Surgers, M. Kelemen, and H. von Lohneysen, Ferromagnetism in carbon-doped Mn₅Si₃ films, *Journal of Applied Physics* **87**, 6013 (2000).

- [14] K. Seo, S. Lee, Y. Jo, M.-H. Jung, J. Kim, D. G. Churchill, and B. Kim, Room Temperature Ferromagnetism in Single-Crystalline Fe₅Si₃ Nanowires, *The Journal of Physical Chemistry C* **113**, 6902 (2009).
- [15] M. K. Kolel-Veetil, S. B. Qadri, M. Osofsky, R. Goswami, and T. M. Keller, Carbon Nanocapsule-Mediated Formation of Ferromagnetic Fe₅Si₃ Nanoparticles, *The Journal of Physical Chemistry C* **113**, 14663 (2009).
- [16] Y. Yamamoto, T. Miura, M. Suzuki, N. Kawamura, H. Miyagawa, T. Nakamura, K. Kobayashi, T. Teranishi, and H. Hori, Direct Observation of Ferromagnetic Spin Polarization in Gold Nanoparticles, *Physical Review Letters* **93**, 116801 (2004).
- [17] A. Fraile Rodríguez, A. Kleibert, J. Bansmann, A. Voitkans, L. J. Heyderman, and F. Nolting, Size-Dependent Spin Structures in Iron Nanoparticles, *Physical Review Letters* **104**, 127201 (2010).
- [18] ICDD 2014 International Centre for Diffraction Data, Powder Diffraction File Card No 01-076-0196.
- [19] ICDD 2014 International Centre for Diffraction Data, Powder Diffraction File Card No 04-002-8149.
- [20] ICDD 2011 International Centre for Diffraction Data, Card No. 00-038-0438 and 0404-0002-3089.
- [21] M. Gottschilch, O. Gourdon, J. Persson, C. de la Cruz, V. Petricek, and T. Brueckel, Study of the antiferromagnetism of Mn₅Si₃: an inverse magnetocaloric effect material, *Journal of Materials Chemistry* **22**, 15275 (2012).
- [22] G. Kresse and D. Joubert, From ultrasoft pseudopotentials to the projector augmented-wave method, *Physical Review B* **59**, 1758 (1999).
- [23] G. Kresse and J. Furthmüller, Efficiency of ab-initio total energy calculations for metals and semiconductors using a plane-wave basis set, *Computational Materials Science* **6**, 15 (1996).
- [24] J. P. Perdew, K. Burke, and M. Ernzerhof, Generalized gradient approximation made simple, *Physical Review Letters* **77**, 3865 (1996).
- [25] Z. X. Tang, C. M. Sorensen, K. J. Klabunde, and G. C. Hadjipanayis, Size-Dependent Curie-Temperature in Nanoscale MnFe₂O₄ Particles, *Physical Review Letters* **67**, 3602 (1991).

CONCLUSIONS

Synthesis of magnetic nanoclusters with unique inert-gas condensation type cluster-deposition method is demonstrated in this dissertation. The materials studied are all rare-earth free and also do not include any expensive element like Pt. Enhancement of magnetocrystalline anisotropy in Co(Zr) nanoclusters is shown due to stabilization of hcp Co phase. Metastable Zr_2Co_{11} phase is stabilized using the cluster-deposition synthesis method and this single-step technique also helped to align the uniaxial nanoclusters using external magnetic field. This is the first time any rare-earth free magnetic materials were demonstrated which have a room-temperature energy product as high as 16.6 MGOe. Using Zr_2Co_{11} nanoclusters as the hard phase along with Fe-Co soft phase, exchange-coupled nanocomposites were fabricated which shows even higher energy product of 19.5 MGOe. This nanocomposite structure likely can be a first step in preparing environment-friendly cost-effective permanent magnets for practical applications. The physics behind the enhanced magnetic properties is explained with the help of experimental characterization and theoretical analysis of the results. Modification of spin-structure at nanoscale was studied for Mn_5Si_3 and Fe_5Si_3 nanoclusters which exhibit enhanced spin-polarization at the nanocluster surface leading to new magnetism compared to the bulk. The density-functional theory was used to understand the physics of spin-modification at low dimension (nano-regime) which helps to develop experiments to visualize those effects. Silicide nanoclusters studied in this dissertation have potential

for future spintronic applications and this study helps to understand the underlying size-dependent magnetism.

The results in this dissertation help to understand the spin-correlations in nanoscale magnets so that proper engineering can be implemented to make these materials useful in future technologies.

APPENDIX A

Measurement of Magnetocrystalline Anisotropy using Law of Approach to Saturation Method:

The magnetic anisotropy constant (K_1) is estimated from the high field region of the experimental curves using the law of approach to saturation method, widely used for randomly oriented magnets.[1–3]

$$M = M_s \left(1 - \frac{A}{H^2}\right) + \chi H \quad (1)$$

In eqn. (1), χ is the high-field susceptibility and A is the constant depends on the anisotropy constant as given by,

$$A = \frac{4}{15} \frac{K_1^2}{M_s^2} \quad (2)$$

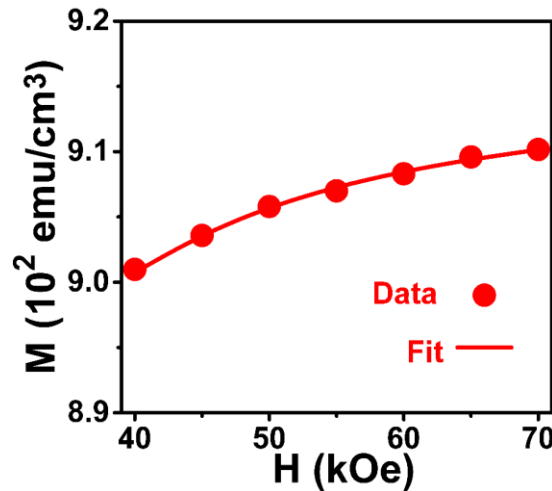


Figure A. Fitting (line) of eqn. (1) with experimental (spheres) M

Experimental M (solid spheres in Fig. A) at high field region is fitted with eqn. (1) (line in Fig. A) to obtain A which is used in eqn. (2) to calculate K_1 which is 8.8 Mergs/cm³ in the present example.

References A:

- [1] G. C. Hadjipanayis, D. J. Sellmyer, and B. Brandt, Rare-earth-rich metallic glasses. I. Magnetic hysteresis, *Physical Review B* **23**, 3349 (1981).
- [2] A. Franco, Jr and F. C. E. Silva, High temperature magnetic properties of cobalt ferrite nanoparticles, *Applied Physics Letters* **96**, 172505 (2010).
- [3] E. Kneller, *Ferromagnetism*. Berlin: Springer, 1962.

APPENDIX B

Calculation of Demagnetization Factor (N) of Nanocluster-Films:

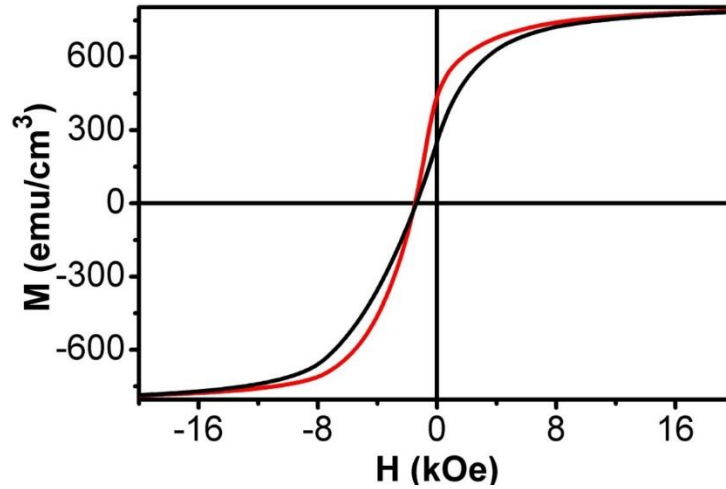


Figure B. Room-temperature hysteresis loops for isotropic Zr_2Co_{11} nanoclusters deposited as films measured along the in-plane or x (red) and out-of-plane or z (black) directions.[1]

The demagnetization factor N_x is estimated from Fig. B, using $N_x + N_y + N_z = 1$ and $N_x = N_y$ for the two in-plane directions, $2N_x + N_z = 1$. [1-3] The individual magnetization factors N_i ($i = x, y, z$) are related to the external magnetic susceptibilities χ_i by $1/\chi_i = 1/\chi_o + N_i$, where χ_o is independent of sample shape. [4] Extracting the two susceptibilities (loop slopes) χ_x and χ_z from Fig. B we obtain $N_x \approx 0.26$ which is for Zr_2Co_{11} nanocluster-films. Similar analysis yields a comparatively low $N_x \approx 0.15$ for nanocomposite films.

References B

- [1] B. Balamurugan, B.Das, W.Y Zhang, R. Skomski and D. J. Sellmyer, Novel Nanostructured Rare-Earth-Free Magnetic Materials with High Energy Products, *Advanced Materials* **25**, 6090 (2013).
- [2] G. Zheng, M. Pardavi-Horvath, X. Huang, B. Keszei, & J. Vandlik, Experimental determination of an effective demagnetization factor for nonellipsoidal geometries. *Journal of Applied Physics* **79**, 5742 (1996).
- [3] R. Skomski, Simple Models of Magnetism, Oxford University Press (2008)
- [4] J. M. D. Coey, Magnetism and Magnetic Materials, Cambridge University Press (2009).

APPENDIX C

Publications:

1. **B. Das**, B. Balamurugan, P. Manchanda, P. Mukherjee, R. Skomski, G. C. Hadjipanayis and D. J. Sellmyer, “Mn₅Si₃ Nanoparticles: Synthesis and Size-induced Ferromagnetism”, *Nano Letters*, 16, 1132 (2016). [Highlighted in University News as extraordinary research finding titled “Team finds unexpected magnetism in nanoscale compound”];
<http://news.unl.edu/newsrooms/today/article/team-finds-unexpected-magnetism-in-nanoscale-compound/>
2. B. Balamurugan, **B. Das**, M. C. Nguyen, X. Xu, Z. Jie, X. Zhang, Y. Liu, A. Huq, S. Valloppilly, Y. Jin, C-Z. Wang, K-M. Ho and D. J. Sellmyer, “Structure and Magnetism of New Rare-Earth-Free Intermetallic Compounds: Fe_{3+x}Co_{3-x}Ti₂ (0 ≤ x ≤ 3)”, *APL Materials* DOI: <http://dx.doi.org/10.1063/1.4968517> (2016)
3. X. Xu, X. Zhang, Y. Yin, B. Balamurugan, **B. Das**, Y. Liu, A. Huq and D. J. Sellmyer, “Anti-site Mixing and Magnetic Properties of Fe₃Co₃Nb₂ Studied by Neutron Powder Diffraction”, *Journal of Physics D: Applied Physics*, 50, 1-6, (2016).
4. M. Khan, O. Alshammari, B. Balamurugan, **B. Das**, D. J. Sellmyer, A. U. Saleheen and S. Stadler, “Controlling the microstructure and associated magnetic properties of Ni_{0.2}Mn_{3.2}Ga_{0.6} melt spun ribbons by annealing”, *AIP Advances* (2016) [In Press].
5. J. Zhang, M. C. Nguyen, B. Balasubramanian, **B. Das**, D. J. Sellmyer, Z. Zeng, K-M. Ho and C-Z. Wang, “Crystal structure and magnetic properties of new Fe₃Co₃X₂ (X= Ti, Nb) intermetallic compounds”, *J. Phys. D: Appl. Phys.* 49, 175002 (2016).
6. B. Balamurugan, P. Manchanda, R. Skomski, P. Mukherjee, S. R. Valloppilly, **B. Das**, G. C. Hadjipanayis and D. J. Sellmyer, “High-coercivity magnetism in nanostructures with strong easy-plane anisotropy”, *Appl. Phys. Lett.* 108, 152406 (2016).
7. D. J. Sellmyer, B. Balamurugan, **B. Das**, P. Mukherjee, R. Skomski and G. C. Hadjipanayis, “Novel Structures and Physics of Nanomagnets”, *J. Appl. Phys.* 117, 172609 (2015).
8. B. Balamurugan, P. Manchanda, R. Skomski, P. Mukherjee, **B. Das**, T. A. George, G. C. Hadjipanayis and D. J. Sellmyer, “Unusual Spin Correlations in a Nanomagnet”, *Appl. Phys. Lett.* 106, 242401 (2015).

9. B. Balamurugan, P. Mukherjee, R. Skomski, P. Manchanda, **B. Das**, and D. J. Sellmyer, "Magnetic nanostructuring and overcoming Brown's paradox to realize extraordinary high-temperature energy products", *Scientific Reports (Nature Publications)*, 4, 6265, (2014).
10. B. Balamurugan, **B. Das**, W. Y. Zhang, R. Skomski and D. J. Sellmyer, "Hf-Co and Zr-Co alloys for rare-earth-free permanent magnets", *J. Phys.: Condens. Matter*. 26, 064204 (2014).
11. B. Balamurugan, **B. Das**, P. Mukherjee and D. J. Sellmyer, "Development of Nanoparticle-Based Permanent-Magnet Materials: Challenges and Advances", *REPM'14 - Proceedings of the 23rd International Workshop on Rare-Earth Permanent Magnets and their Applications*. (2014).
12. B. Balamurugan[†], **B. Das**[†], R. Skomski, W. Y. Zhang and D. J. Sellmyer, "Novel Nanostructured Rare-Earth-Free Magnetic Materials with High Energy Products", *Advanced Materials*. 25, 6089 (2013) ([†]Joint **First Authorship**; equal contribution in the research). Selected as the *Frontispiece cover* reserved for highlighting outstanding communications.
13. **B. Das**, B. Balamurugan, R. Skomski, X. Z. Li, P. Mukherjee, G. C. Hadjipanayis and D. J. Sellmyer, "Structure and magnetism of dilute Co(Zr) nanoclusters", *J. Appl. Phys.* 113, 17B509 (2013).
14. **B. Das**, B. Balamurugan, P. Kumar, R. Skomski, V. R. Shah, J. E. Shield, A. Kashyap and D. J. Sellmyer, "HfCo₇-Based Rare-Earth-Free Permanent-Magnet Alloys", *IEEE Trans. Magn.* 49, 3330 (2013).
15. D.J. Sellmyer, B. Balamurugan, W.Y. Zhang, **B. Das**, R. Skomski, P. Kharel, Y. Liu, "Advances in Rare-Earth-Free Permanent Magnets", *PRICM: 8 Conference Proceedings, Wiley*. (2013).
16. **B. Das**, B. Balamurugan, W. Y. Zhang, R. Skomski, E. S. Krage, S. R. Valloppilly, J. E. Shield and D. J. Sellmyer, "Magnetism of Less Common Cobalt-Rich Alloys", *REPM'12 - Proceedings of the 22nd International Workshop on Rare-Earth Permanent Magnets and their Applications*. (2012).
17. B. Balamurugan, **B. Das**, V. R. Shah, R. Skomski, X. Z. Li and D. J. Sellmyer, "Assembly of uniaxially aligned rare-earth-free nanomagnets", *Appl. Phys. Lett.* 101, 122407 (2012).
18. X. Li, **B. Das**, B. Balamurugan, V.R. Shah, R. Skomski, D.J. Sellmyer, E.S. Krage and Y. Huh, "Structural Investigation of Fe-doped SmCo₄B Alloy System by TEM", *Microscopy and Microanalysis*. 18, 1464 (2012).
19. B. Balamurugan, R. Skomski, **B. Das**, X. Z. Li, V. R. Shah, P. Manchanda, A. Kashyap and D. J. Sellmyer, "Magnetism of dilute Co(Hf) and Co(Pt) nanoclusters", *J. Appl. Phys.* 111, 07B532 (2012).